Pt Nanocrystals Formed by Ion Implantation and Modified by Swift Heavy Ion Irradiation

Raquel Giulian

A thesis submitted for the degree of

Doctor of Philosophy

of

The Australian National University

May 2009

I certify that, to the best of my knowledge and belief, this thesis represents my own original work, except where due mention is made in the text. It contains no material previously submitted for a degree or diploma at any university.

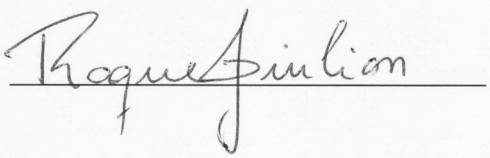

Raquel Giulian

May 2009

If you intend to do something good with the information that has been written here,
this thesis is dedicated to you.

Acknowledgements

I wish I could write in one page all the good things that happened to me during my PhD, and the things that were not so good as well, because they made me grow and become the person I am now. If you could spend some time being myself, you would see how many wonderful friends I have. I cannot type here the name of all of them and how much I respect and appreciate the support they give me every day, it is simply too much for just one page, but I hope each and everyone of them know that they are special.

I have to mention that I am the luckiest person on Earth, for marrying you, Leandro. The last four years were pure blessing and not a single moment would have happened without you. I love you.

À minha família, que eu amo tanto e sinto tanta saudade. Obrigado pela paciência, pelo carinho, pelas palavras de incentivo e por estarem sempre comigo em pensamento e oração, quando não ao telefone. É preciso mais que 16,000 km de oceano pra nos separar.

Eu sei meu Pai que mesmo em outra vida tu estas celebrando comigo essa conquista. Deus há de transformar a minha alegria em luz para o teu caminho.

A special thanks to my supervisor Dr. Mark C. Ridgway for giving me the opportunity to become a PhD. Thanks Mark for being so present and supportive. Your guidance, patience, wisdom and friendship made my life as a student very enjoyable. Thanks for introducing me to this fantastic group: Aidan, Patrick, Leandro, David L., David S., Claudia and Zohair. They are the living proof that the sum of the parts is never as good as the whole. It is a privilege to be part of such a team.

And I would like to thank the H that contaminated my samples and made my results much more interesting and challenging; the dimple grinder and PIPS that broke so easily in the hands of the unprepared, encouraging me to learn a new and more exciting sample preparation method that doesn't require the use of any expensive equipment; the nasty chemicals that corroded my samples and not my hands; and my computer, that worked almost as many hours as I did in Canberra, Tsukuba, Chicago, Aioi, Melbourne, Singapore, Taormina and Campinas.

PUBLICATIONS

Journal articles of the candidate. Those that originated directly from this thesis are indicated by *.

1* Giulian, R., Kluth, P., Araujo, L. L., Llewellyn, D. J. and Ridgway, M. C., Pt nanocrystals formed by ion implantation: A defect-mediated nucleation process. *Appl. Phys. Lett.* **91**, 093115 (2007).

2* Giulian, R., Kluth, P., Johannessen, B., Araujo, L. L., Llewellyn, D. J., Cookson, D. J. and Ridgway, M. C., Synthesis and characterization of ion-implanted Pt nanocrystals in SiO2. *Nucl. Instrum. Meth. B* **257**, 33 (2007).

3 Johannessen, B., Kluth, P., Giulian, R., Araujo, L. L., Llewellyn, D. J., Foran, G. J., Cookson, D. J. and Ridgway, M. C., Modification of embedded Cu nanoparticles: Ion irradiation at room temperature. *Nucl. Instrum. Meth. B* **257**, 37 (2007).

4 Kluth, P., Johannessen, B., Giulian, R., Schnohr, C. S., Foran, G. J., Cookson, D. J., Byrne, A. P. and Ridgway, M. C., Ion irradiation effects on metallic nanocrystals. *Radiat. Eff. Defects Solids* **162**, 501 (2007).

5* Ridgway, M. C., Kluth, P., Araujo, L. L., Sprouster, D. J., Giulian, R., Johannessen, B., Llewellyn, D. J., Cookson, D. J. and Foran, G. J., X-ray Absorption Spectroscopy and Small Angle X-ray Scattering studies of Metal nanoparticles using Synchrotron Radiation. *Chemistry in Australia* **74**, 13 (2007).

6 Araujo, L. L., Giulian, R., Johannessen, B., Llewellyn, D. J., Kluth, P., Azevedo, G. d. M., Cookson, D. J. and Ridgway, M. C., Structural characterization of Ge nanocrystals in silica amorphised by ion irradiation. *Nucl. Instrum. Meth. B* **266**, 3153 (2008).

7 Araujo, L. L., Giulian, R., Sprouster, D. J., Schnohr, C. S., Llewellyn, D. J., Kluth, P., Cookson, D. J., Foran, G. J. and Ridgway, M. C., Size-dependent characterization of embedded Ge nanocrystals: Structural and thermal properties. *Phys. Rev. B* **78**, 094112 (2008).

8* Giulian, R., Kluth, P., Araujo, L. L., Sprouster, D. J., Byrne, A. P., Cookson, D. J. and Ridgway, M. C., Shape transformation of Pt nanoparticles induced by swift heavy-ion irradiation. *Phys. Rev. B* **78**, 125413 (2008).

9* Giulian, R., Kluth, P., Sprouster, D. J., Araujo, L. L., Byrne, A. and Ridgway, M. C., Swift heavy ion irradiation of Pt nanocrystals embedded in SiO2. *Nucl. Instrum. Meth. B* **266**, 3158 (2008).

10 Kluth, P., Schnohr, C. S., Pakarinen, O. H., Djurabekova, F., Sprouster, D. J., Giulian, R., Ridgway, M. C., Byrne, A. P., Trautmann, C., Cookson, D. J., Nordlund, K. and Toulemonde, M., Fine Structure in Swift Heavy Ion Tracks in Amorphous SiO2. *Phys. Rev. Lett.* **101**, 175503 (2008).

11 Araujo, L. L., Giulian, R., Johannessen, B., Llewellyn, D. J., Kluth, P., Cookson, D. J., Foran, G. J. and Ridgway, M. C., Properties of Ge nanocrystals determined by EXAFS and SAXS. *Advanc. Synch. Rad.* **in press** (2009).

12 Araujo, L. L., Kluth, P., Giulian, R., Sprouster, D. J., Johannessen, B., Foran, G. J., Cookson, D. J. and Ridgway, M. C., Characterizing structural and vibrational properties of nanoparticles embedded in silica with XAS, SAXS and auxiliary techniques. *AIP Conf. Proc.* **1092**, 125 (2009).

13* Giulian, R., Araujo, L. L., Kluth, P., Sprouster, D. J., Schnohr, C. S., Foran, G. J. and Ridgway, M. C., Temperature-dependent EXAFS analysis of embedded Pt nanocrystals. *J. Phys.: Condens. Matter* **21**, 155302 (2009).

14* Giulian, R., Araujo, L. L., Kluth, P., Sprouster, D. J., Schnohr, C. S., Johannessen, B., Foran, G. J. and Ridgway, M. C., The influence of annealing conditions on the growth and structure of embedded Pt nanocrystals. *J. Appl. Phys.* **105**, 044303 (2009).

15* Giulian, R., Kluth, P., Sprouster, D. J., Araujo, L. L., Byrne, A., Llewellyn, D. J., Cookson, D. J. and Ridgway, M. C., Angle-dependent measurements of elongated Pt nanocrystals using small angle X-ray scattering. *Advanc. Synch. Rad.* **in press** (2009).

16* Giulian, R., Kluth, P., Sprouster, D. J., Araujo, L. L., Byrne, A. P., Cookson, D. J. and Ridgway, M. C., SAXS Analysis of Embedded Pt Nanocrystals Irradiated with Swift Heavy Ions. *AIP Conf. Proc.* **1092**, 45 (2009).

17 Kluth, P., Giulian, R., Sprouster, D. J., Schnohr, C. S., Byrne, A. P., Cookson, D. J. and Ridgway, M. C., Energy dependent saturation width of swift heavy ion shaped embedded Au nanoparticles. *Appl. Phys. Lett.* **94**, 113107 (2009).

18* Ridgway, M. C., Kluth, P., Giulian, R., Sprouster, D. J., Araujo, L. L., Schnohr, C. S., Llewellyn, D. J., Byrne, A. P., Foran, G. J. and Cookson, D. J., Changes in metal nanoparticle shape and size induced by swift heavy-ion irradiation. *Nucl. Instrum. Meth. B* **267**, 931 (2009).

19 Sprouster, D. J., Giulian, R., Kluth, P., Araujo, L. L., Foran, G. J., Cookson, D. J. and Ridgway, M. C., Synchrotron radiation characterization of Co nanoparticles. *Advanc. Synch. Rad.* **in press** (2009).

20 Sprouster, D. J., Giulian, R., Schnohr, C. S., Kluth, P., Araujo, L. L., Byrne, A. P., Foran, G. J. and Ridgway, M. C., Swift Heavy Ion Irradiation of Cobalt Nanoparticles. *AIP Conf. Proc.* **1092**, 55 (2009).

21 Wesch, W., Schnohr, C. S., Kluth, P., Hussain, Z. S., Araujo, L. L., Giulian, R., Sprouster, D. J., Byrne, A. P. and Ridgway, M. C., Structural modification of swift heavy ion irradiated amorphous Ge layers. *J. Phys D: Appl. Phys.* **42**, 115402 (2009).

22* Giulian, R., Araujo, L. L., Kluth, P., Sprouster, D. J., Schnohr, C. S., Byrne, A. P., Foran, G. J. and Ridgway, M. C., Structural changes and H desorption in swift heavy ion irradiated embedded Pt nanocrystals. *J. Phys D: Appl. Phys.* (submitted in 2009).

23 Sprouster, D. J., Giulian, R., Araujo, L. L., Kluth, P., Llewellyn, D. J., Byrne, A. P., Foran, G. J., Cookson, D. J. and Ridgway, M. C., Swift heavy ion irradiation induced growth and dissolution of embedded Co nanoparticles. *Nucl. Instrum. Meth. B* (submitted in 2009).

24 Sprouster, D. J., Giulian, R., Araujo, L. L., Kluth, P., Llewellyn, D. J., Johannessen, B., Foran, G. J., Kirby, N., Nordlund, K. and Ridgway, M. C., Amorphization of Co nanoparticles. (submitted in 2009).

25 Sprouster, D. J., Giulian, R., Johannessen, B., Schnohr, C. S., Araujo, L. L., Kluth, P., Byrne, A. P., Foran, G. J. and Ridgway, M. C., A FCC-to-HCP phase transformation in Co nanoparticles induced by swift heavy ion irradiation. *Phys. Rev. B* (submitted in 2009).

26 Sprouster, D. J., Giulian, R., Schnohr, C. S., Araujo, L. L., Kluth, P., Llewellyn, D. J., Byrne, A. P., Foran, G. J., Cookson, D. J. and Ridgway, M. C., Swift heavy ion irradiation induced shape and structural changes in Cobalt nanoparticles. *Phys. Rev. B* (submitted in 2009).

27 Sprouster, D. J., Johannessen, B., Giulian, R., Llewellyn, D. J., Araujo, L. L., Kluth, P., Cookson, D. J., Foran, G. J. and Ridgway, M. C., Formation and structural characterization of ion implanted cobalt nanoparticles. *Phys. Rev. B* (submitted in 2009).

ABSTRACT

This thesis reports on the formation of Pt nanocrystals (NC) embedded in amorphous SiO_2 by ion implantation and the subsequent changes in shape, size and structure induced by swift heavy ion irradiation.

The growth and structure of Pt NCs formed by ion implantation have been investigated as a function of the annealing conditions. Transmission electron microscopy (TEM) and small-angle x-ray scattering (SAXS) measurements demonstrated the annealing ambient has a significant influence on NC size. Samples annealed in either Ar, O_2 or forming gas (FG, 95% N_2 : 5% H_2) at temperatures ranging from 500-1300 °C formed spherical NCs with mean diameters ranging from 1-14 nm. For a given temperature, annealing in Ar yielded the smallest NCs. O_2 and FG ambients produced NCs of comparable size though the latter induced H chemisorption at 1100°C and above, as verified with x-ray absorption fine structure (XAFS) spectroscopy. This H intake was accompanied by a bond-length expansion and increased structural disorder in NCs of diameter > 3 nm. The latter was also observed in NCs of smaller sizes, regardless of annealing ambient, together with a size dependent bond-length contraction.

The influence of defects produced in the SiO_2 on the size of Pt NCs has also been investigated. Thin SiO_2 films were irradiated with high-energy Ge ions then implanted with Pt ions. Without Ge irradiation, the largest Pt NCs were observed beyond the Pt projected range. With irradiation, Ge-induced structural modification of the SiO_2 layer yielded a decrease in Pt NC size with increasing Ge fluence. A defect-mediated NC nucleation mechanism was proposed and a simple yet effective means of modifying and controlling the Pt NC size is demonstrated.

The vibrational and thermal properties of embedded Pt NCs have been studied with temperature-dependent extended x-ray absorption fine structure (EXAFS) spectroscopy. NCs of diameter 1.8-7.4 nm were analysed over the temperature range

20-295 K. An increase in Einstein temperature (~194 K) relative to that of a Pt standard (~179 K) was evident for the smallest NCs while those larger than ~2.0 nm exhibited values comparable to bulk material. Similarly, the thermal expansion of interatomic distances was lowest for small NCs. While the amorphous SiO_2 matrix restricted the thermal expansion of interatomic distances, it did not have a significant influence on the mean vibrational frequency of embedded Pt NCs. Instead, the latter was governed by finite-size effects or, specifically, capillary pressure.

Pt NCs were irradiated with Au ions in the energy range 27-185 MeV. SAXS and TEM were used to characterize an irradiation-induced shape transformation within the NCs. A transformation from spherical to rod-like shape with increasing irradiation fluence was observed for NCs larger than an energy-dependent threshold diameter which varied from 4.0 to 6.5 nm over 27 to 185 MeV. NCs smaller than this threshold diameter remained spherical upon irradiation but decreased in size as a result of dissolution. The latter was more pronounced for the smallest particles. The minor dimension of the transformed NCs saturated at an energy-dependent value comparable to the threshold diameter for elongation. The saturated minor dimension was less than the diameter of the irradiation-induced molten track within the matrix. We demonstrated that Pt NCs of diameter 13 nm reach saturation of the minor dimension beyond a total energy deposition into the matrix of 20 keV/nm^3.

In addition to shape transformation, NC dissolution was observed. SAXS measurements showed a decrease in the total NC volume with increasing energy deposited into the matrix. H-containing NCs with ~8 nm mean diameter exhibit a significant reduction in H content after low-intermediate SHII fluences, while NCs with ~14 nm mean diameter show lesser dissolution at such fluences. These differences were explained based on the energy per Pt atom after SHII, which is less the required for H desorption for the latter. EXAFS analysis showed that structural parameters (coordination number, bond-length and mean-square relative displacement) were strongly influenced by the extent of Pt-H bonding and NC dissolution.

CONTENTS

CHAPTER I

WHY NANOCRYSTALS ARE INTERESTING

This chapter is an introduction to the research work presented in this thesis. A brief historical overview is followed by a general discussion of the characteristics and applications of Pt nanocrystals. The motivation for the thesis research is presented, as is a brief outline.

1.1 – Introduction

Nowadays we are well accustomed to the concept of "nano", which refers to dimensions of 10^{-9}m, but fifty years ago, when computers were as big as a room, this concept was not in vogue. Nevertheless, the idea of very small things was already inspiring. In his talk entitled *"There's plenty of room at the bottom"*, in December 1959, Richard P. Feynman shared some interesting thoughts with his audience:[1]

> *"... As we go down in size, there are a number of interesting problems that arise. All things do not simply scale down in proportion....What would the properties of materials be if we could really arrange the atoms the way we want them?... I can't see exactly what would happen, but I can hardly doubt that when we have some control of the arrangement of things on a small scale we will get an enormously greater range of possible properties that substances can have, and of different things that we can do... A friend of mine suggests a very interesting possibility for relatively small machines. He says that, although it is a very wild idea, it would be interesting in surgery if you could swallow the surgeon..."*

Indeed, as we go down in size the properties of materials change and new applications arise. Miniaturized surgeons may still need some time to become reality, but in the meantime nanostructures with the capability of targeting specific tissues have been developed and are already in used for disease diagnostics and drug delivery.[2, 3, 4] Metallic nanocrystals (NCs) embedded in a dielectric matrix have potential applications, for example, in optical filters and switching devices due to their linear and non-linear optical properties.[5] Pt NCs on a supporting scaffold have been widely investigated for their important catalytic applications including the reduction of pollutant gases in automobile exhaust.[6] These are just a few examples of the fascinating NC capabilities, which to be fully exploited need to be thoroughly understood.

The present thesis aims to contribute to the understanding of a very small portion of this new world, with the study of Pt NCs formed by ion implantation in amorphous SiO_2 and the changes in shape, size and structure induced by swift heavy ion

irradiation. This introductory chapter highlights the main reasons why NCs have different properties than their bulk counterparts, starting with a brief historical overview followed by some examples of reported and promising applications.

1.2 – Historical overview

Nanocrystals have been used by artisans for a very long time, although they were not aware of that. One of the oldest examples is the Lycurgus cup, a dichroic glass cup with a mythological scene from the 4th century AD, probably made in Rome and currently on display at The British Museum in London.[7] The glass contains tiny amounts of colloidal gold and silver, and turns from opaque green to a glowing translucent red when light is shone through it, as can be seen in Fig. 1.1. The earliest explanation for such unusual optical properties was given much later, by Michael Faraday[8] in 1857. NCs were also found in Mesopotamian pottery from the 9th century AD, where Ag and Cu NCs were later identified as the source of a glittering effect on the surface.[9]

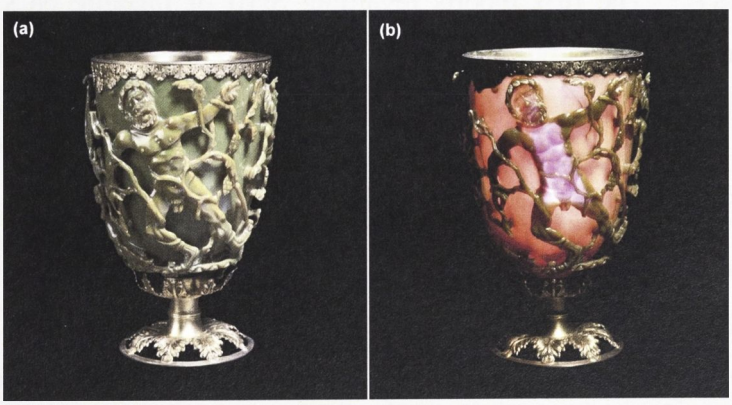

Fig. 1.1 – Lycurgus cup[7] (a) and the change in color when light is shone through it (b).

The term "nanometer" was first used to characterize particle sizes in the beginning of the 20th century by Richard Adolf Zsigmondy, who studied Au particles and other nanomaterials with sizes of approximately 10 nm.[10] Innumerous experimental and theoretical works have been developed during the 20th century, demonstrating and explaining many of the interesting characteristics presented by nanometer sized particles. As an example we cite the works of Fröhlich[11] in 1937, which describe the

creation of a discrete electronic energy spectrum when metallic particles become sufficiently small. In the 1960's, Kubo and Kawabata[12, 13] calculated a number of electronic properties of small metallic particles, including the low-temperature specific heat. A decade later, Buffat and Borel[14] demonstrated the decrease in the melting temperature of Au particles with decreasing particle size, evidencing the changes in the physical properties of materials when dimensions approach the nanometer range.

Ion implantation was first used for NC fabrication by Arnold and Borders[15, 16] in the 1970s, but it was in the 1990s that it became an important tool in this area, due to the increasing interest in optical filters and switching devices and their technological implications (discussed in the following sections).[17, 18] Many other experimental techniques like chemical synthesis, vapor condensation and sputtering deposition can also be used for NC fabrication, the choice of which relies mainly on the particular application.

Swift heavy ion irradiation (SHII) has been an important tool in the transformation of materials.[19-22] Elongation perpendicular to the ion beam direction was first reported for metallic glass in the early 1980's by Klaumünzer and Schumacher,[19] and then observed later in a series of amorphous semiconductors and insulators, including SiO_2.[23] The first reports regarding SHII of metallic NCs (embedded in a dielectric matrix) were published in 2003 by D'Orleans and co-workers,[24] where elongation parallel to the incident ion beam was observed for Co NCs embedded in amorphous SiO_2 (a-SiO_2). Changes in the magnetic properties of the system were also observed due to the anisotropy in the NC shape and their high degree of alignment. These results launched a series of studies involving metallic NCs and swift heavy ions, in an attempt to explain the mechanisms responsible for the changes in shape, size and structure induced by SHII,[25-32] as well as the interesting properties that arise from such changes, which will be discussed in the following sections.

1.3 – What makes NCs different?

1.3.1 – Surface-to-volume ratio

The total number of atoms forming a NC scales linearly with its volume. The fraction of atoms at the surface, which is proportional to the surface area of the NC

divided by its volume (surface-to-volume ratio), increases with decreasing NC dimensions. The schematics in Fig. 1.2 show a NC with a total of (a) 10 atoms (all of which are at the surface), (b) 92 atoms (74 at the surface) and (c) 792 atoms (394 at the surface). The diameter of the particle shown in Fig.1.2(c) is approximately twice the one shown in Fig.1.2(b), which is about twice the one in Fig.1.2(a).

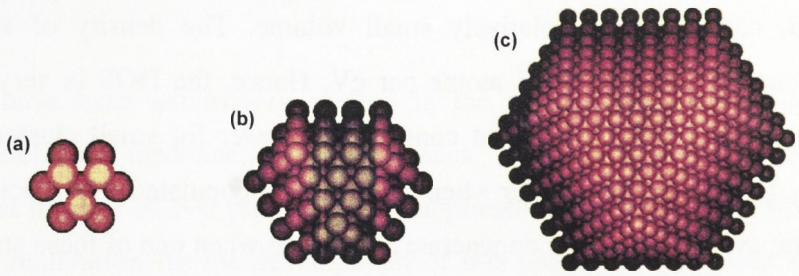

Fig. 1.2 –Schematics of NCs formed by (a) 10 atoms, (b) 92 atoms and (c) 792 atoms. (figure extracted from Frenkel et al.[33])

Atoms at the surface have fewer direct neighbors than atoms in the bulk. Therefore, NCs with a large fraction of surface atoms have a low mean coordination number (CN). The termination of the lattice periodicity in the direction of the surface normal creates a surface potential barrier (or work function), which is the energy separation between the vacuum level (for free-standing NCs) or the potential of the elements in the matrix (for embedded NCs) and the Fermi energy. The work function depends on the charge density in the surface region and consequently on the valence state of the surface atoms. It can be reduced through reaction with electronegative atoms (like N or O) or increased, for example, in the presence of H-like bonding.[34]

Properties that are influenced by surface related effects scale linearly with the inverse NC diameter (or surface-to-volume ratio), as the average CN, cohesive energy, melting point, capillary pressure, among others.[35] It is important to point out that such values may vary locally, as they are usually different for an atom at the surface or in the interior of the NC, but their average value reflect the linearity with the inverse NC diameter, approaching the corresponding bulk value for large NCs.

1.3.2 – Quantum confinement

Bulk metals and semiconductors differ from isolated atoms and molecules in a way that the atomic orbitals are no longer discrete, but form extended band structures. Each atom contributes with its atomic states to a band while the core orbitals remain localized, confined to a relatively small volume. The density of states (DOS) is proportional to the number of atoms per eV. Hence, the DOS is very large for bulk matter (~Avogadro's number) but considerably lower for small clusters, scaling with NC size. Discontinuities appear when the states are populated with electrons: for highly symmetric systems there are degenerate states, and when one of these states is filled the next electron must occupy the next state of higher energy. These discontinuities are blurred when an additional atom is added to a highly symmetric system.[35] The schematic in Fig.1.3 illustrates the development of the DOS with cluster size, where E_F is the Fermi energy, δ is the gap between the highest occupied and lowest unoccupied states (also called *Kubo gap*), and k_BT (Boltzman's constant times temperature) represents the thermal energy.

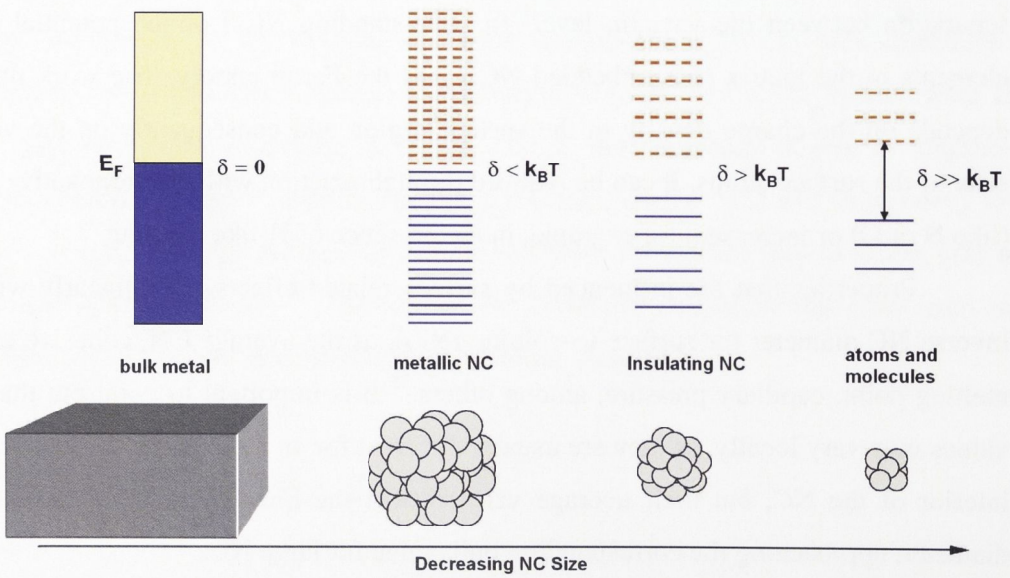

Fig. 1.3 – Evolution of the Kubo gap and the density of states as the number of atoms in a system decreases.

When electrons get thermally excited across the Kubo gap, a low temperature insulator becomes a semiconductor and at higher temperatures a metal. In a similar way, the reduction in NC size increases the Kubo gap, thus the electrons require more energy to overcome δ and metal-to-non-metal transitions occur.[35]

1.4 – NC properties and applications

NCs have been extensively studied in the past decades in a wide rage of disciplines, including medicine, biology, physics, materials engineering and others. Among a vast number of NC properties and applications, some are described here to illustrate the motivation for the development of this project, in particular the surface plasmon resonance and the nonlinear optical properties of metallic NCs embedded in a dielectric matrix. A brief overview on the enhanced catalytic activity of NCs is also presented, given Pt NCs are widely used for catalysis.

1.4.1 – Surface plasmon resonance

Several metallic NCs including Ag, Au and Pt exhibit strong absorption in the visible region of the spectrum, due to the collective oscillation of conduction band electrons in response to the electrical field of the electromagnetic radiation (light). This phenomenon is termed *surface plasmon resonance* (SPR) given the transient displacement of net charges on the particle surface, as illustrated schematically in Fig.1.4.

The frequency of the SPR can be spectrally tuned by changing the NC size, shape and environment.[36] When the size of the particle is much smaller than the wavelength of the incident light, the NC experiences a field that is spatially constant but with a time-dependent phase. Thus the displacement of the charges in a small sphere is homogeneous, yielding a dipolar charge distribution on the surface, while for larger spherical NCs high multipolar distributions are excited. The particle only absorbs energy by the excitation of the surface plasmon resonance. By elongating the NC in one direction (Fig.1.4(b)), a second, lower energy dipolar resonance band is formed in addition to that at higher energy associated with the transverse direction. As particles

become more complex, other modes can arise with many bands over a broad spectral region.

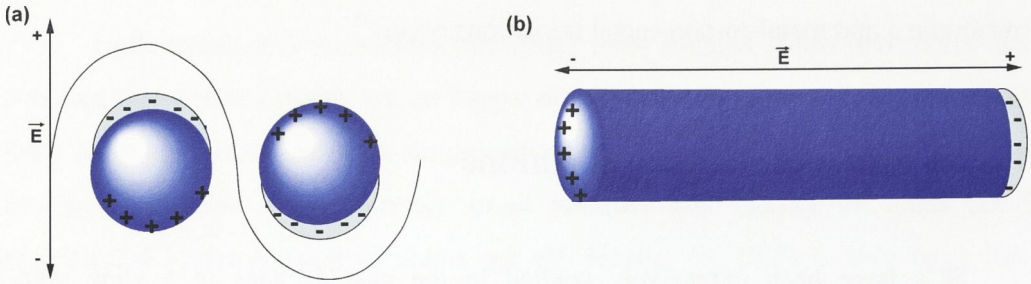

Fig.1.4 – Schematic illustration of surface plasmon resonance in (a) spherical and (b) elongated NC. (For the later, only the transversal electric field is shown.)

The strong enhancement of the local field around an excited NC leads to a wide range of potential applications, including biosensing, optical antennas, plasmonic waveguides and surface Raman scattering.[36]

1.4.2 – Third-order nonlinear optical properties

A currently active area of research is concerned with all-optical devices that are designed to switch and process light signals without converting them to electronic form, thus increasing the speed of switching, routing and signal processing. Such devices are essentially based on the non-linear optical properties of materials, i.e. changes of the refractive index caused by an intense optical beam or by an applied electric field.

When a light wave propagates through an optical medium, the oscillating electromagnetic field exerts a polarizing force on all of the electrons comprising the medium. The major polarizing effect is on the conduction electrons, since the inner electrons are tightly bound to the nuclei. For an optical field sufficiently intense to drive the electrons beyond the quadratic minimum of the interatomic potential (comparable or greater than the intra-atomic field (~10^{10} V/m)), the response becomes increasingly non-linear. At high photon intensities, the induced fields (which correspond to a significant fraction of the particles' internal field) adds to the particles internal field and substantially modifies the motion of the charges within the particles altering the nature of the polarization within the material.

It has been demonstrated that the inherent non-linear optical response of a dielectric host material, such as glass, polymer, etc., may be enhanced by several orders of magnitude by the introduction of small semiconductor or metal NCs. The non-linear response of NCs arises from saturable absorption at the excitation levels, which modifies the quantum states of the electrons and their interaction with applied optical fields (due to quantum confinement).[17]

1.4.3 – Enhanced catalytic activities

Catalysts mediate the pathways by which chemical reactions occur, enabling the highly selective formation of desired products at rates that are commercially viable. They are also essential for the reduction of air and water pollution (from automobile exhausts, for example).[6]

NCs present reactivity not observed in their bulk counterparts (Pt NCs, in particular) given their high surface-to-volume ratio, which makes them interesting for catalysis.[37] Their efficiency is determined not only by the fraction of uncoordinated atoms, but also by the NC surface structure. Pt NCs serve as an excellent catalyst for CO/NO_x oxidation in catalytic converters, production of nitric acid, refining of petroleum and many organic reactions such as hydrogenations. It is also a critical component of the fuel cell technology, acting as the most effective electrocatalyst for the oxygen reduction reaction and fuel oxidation reaction (including H, methanol, ethanol and formic acid).[38]

1.5 – Motivation for this study

The development of new technologies based on NCs requires the understanding of NC full capabilities. The development of suitable fabrication methods as well as the characterization of such systems is thus essential. Although the formation of NCs using ion beam synthesis has been extensively developed since the 1970s,[15, 16, 39] Pt NCs formed by ion implantation have received scant attention in the literature. To the best of the author's knowledge, Pt, Co-Pt and Fe-Pt NCs formed in Al_2O_3 by ion implantation have been reported,[40-43] but no record of Pt NCs formed by ion implantation in a-SiO_2 has been found.

The recent reports by D'Orleans and co-workers[24, 44-46] on deformation of Co NCs embedded in a-SiO_2 by means of swift heavy ion irradiation (SHII) have motivated a variety of studies around the world on the SHII of embedded metallic NCs,[21, 25-32, 47-53] as well as reviving the interest in changes induced by energetic ions in a-SiO_2.[54-58] The elongation of metallic NCs in the direction parallel to the incident beam offers the possibility of tailoring NCs properties by changing their shape, especially taking advantage of the high degree of alignment observed after irradiation. Although the formation of non-spherical NCs is also possible using other methods (like chemical synthesis), the non-spherical NCs are usually randomly oriented. Given many of the NC properties are size dependent and the majority of the experimental techniques used in NC characterization rely on the measurement of an ensemble of NCs (thus returning an average value for the quantity in question), the results are usually degraded by the broadening of the average size distributions. Using SHII the elongated NCs can be characterized in different directions, parallel and perpendicular to the incident beam, for example. The same is valid for several NC properties like magnetization and surface plasmon resonance, whose results depend on the orientation of the samples.[24, 59]

The study of Pt NCs in a-SiO_2 was motivated by the potential applications that metallic NCs embedded in a dielectric matrix present. In the search for fabrication conditions that minimize the broad size distribution usually observed in NCs formed by ion implantation, parameters like ion fluence, annealing temperature and ambient were tailored. The influence of defects produced in the a-SiO_2 matrix was also evaluated. SHII was used to modify the NC size and shape, which together with other parameters like structure, atomic disorder, thermal vibration, contaminants, were analyzed by means of transmission electron microscopy (TEM), small-angle x-ray scattering (SAXS), x-ray absorption fine structure (XAFS) (near-edge and extended regions), among other techniques.

1.6 – Brief outline of the thesis

The thesis is organized in the following sequence:

- **Chapter I** provides an introduction and motivation for the research developed for this thesis, with the description of some important applications for which NCs can be used;

- **Chapter II** describes the laboratory-based experimental techniques used for the NC fabrication and analysis, namely ion implantation and swift heavy ion irradiation, Rutherford backscattering spectrometry (RBS) and TEM;

- **Chapter III** describes the synchrotron based experimental techniques, namely SAXS and XAFS;

- **Chapter IV** explains the sample preparation and data analyses methods;

- **Chapter V** presents results on Pt NC formation;

- **Chapter VI** presents results on the SHII of Pt NCs;

- **Chapter VII** contains the main conclusions from the results presented in the previous chapters.

References

1 http://www.zyvex.com/nanotech/feynman.html.

2 M. E. Akerman, W. C. W. Chan, P. Laakkonen, S. N. Bhatia, and E. Ruoslahti, P. Natl. Acad. Sci. USA **99**, 12617 (2002).

3 M. V. Yezhelyev, X. Gao, Y. Xing, A. Al-Hajj, S. M. Nie, and R. M. O'Regan, Lancet Oncol. **7**, 657 (2006).

4 M. E. Davis, Z. Chen, and D. M. Shin, Nat. Rev. Drug Discov. **7**, 771 (2008).

5 A. Meldrum, L. A. Boatner, and C. W. White, Nucl. Instr. and Meth. B **178**, 7 (2001).

6 A. T. Bell, Science **299**, 1688 (2003).

7 http://www.britishmuseum.org.

8 M. Faraday, Phil. Trans. Roy. Soc. London **147**, 145 (1857).

[9] I. Borgia, B. Brunetti, I. Mariani, A. Sgamellotti, F. Cariati, P. Fermo, M. Mellini, C. Viti, and G. Padeletti, Appl. Surf. Sci. **185**, 206 (2002).

[10] R. Zsigmondy, *Colloids and the Ultramicroscope* (J.Wiley and Sons, New York, 1914).

[11] H. Fröhlich, Physica **4**, 406 (1937).

[12] R. Kubo, J. Phys. Soc. Jpn. **17**, 975 (1962).

[13] A. Kawabata and R. Kubo, J. Phys. Soc. Jpn. **21**, 1765 (1966).

[14] P. Buffat and J. P. Borel, Phys. Rev. A **13**, 2287 (1976).

[15] G. W. Arnold, J. Appl. Phys. **46**, 4466 (1975).

[16] G. W. Arnold and J. A. Borders, J. Appl. Phys. **48**, 1488 (1977).

[17] P. Chakraborty, J. Mater. Sci. **33**, 2235 (1998).

[18] R. F. Haglund, Mat. Sci. Eng. A-Struct. **253**, 275 (1998).

[19] S. Klaumunzer and G. Schumacher, Phys. Rev. Lett. **51**, 1987 (1983).

[20] A. Hedler, S. L. Klaumunzer, and W. Wesch, Nature Materials **3**, 804 (2004).

[21] S. Klaumunzer, Nucl. Instr. and Meth. B **244**, 1 (2006).

[22] E. Akcoltekin, T. Peters, R. Meyer, A. Duvenbeck, M. Klusmann, I. Monnet, H. Lebius, and M. Schleberger, Nature Nanotechnology **2**, 290 (2007).

[23] E. Snoeks, A. Polman, and C. A. Volkert, Applied Physics Letters **65**, 2487 (1994).

[24] C. D'Orleans, J. P. Stoquert, C. Estournes, C. Cerruti, J. J. Grob, J. L. Guille, F. Haas, D. Muller, and M. Richard-Plouet, Phys. Rev. B **67**, 220101 (2003).

[25] S. Roorda, T. van Dillen, A. Polman, C. Graf, A. van Blaaderen, and B. J. Kooi, Adv. Mater. **16**, 235 (2004).

[26] A. Oliver, J. A. Reyes-Esqueda, J. C. Cheang-Wong, C. E. Roman-Velazquez, A. Crespo-Sosa, L. Rodriguez-Fernandez, J. A. Seman, and C. Noguez, Phys. Rev. B **74**, 245425 (2006).

[27] F. Singh, D. K. Avasthi, O. Angelov, P. Berthet, and J. C. Pivin, Nucl. Instrum. Meth. B **245**, 214 (2006).

[28] B. Joseph, J. Ghatak, H. P. Lenka, P. K. Kuiri, G. Sahu, N. C. Mishra, and D. P. Mahapatra, Nucl. Instrum. Meth. B **256**, 659 (2007).

[29] K. Awazu, X. M. Wang, M. Fujimaki, J. Tominaga, H. Aiba, Y. Ohki, and T. Komatsubara, Phys. Rev. B **78**, 8 (2008).

[30] R. Giulian, P. Kluth, L. L. Araujo, D. J. Sprouster, A. P. Byrne, D. J. Cookson, and M. C. Ridgway, Phys. Rev. B **78**, 125413 (2008).

[31] P. Kluth, B. Johannessen, R. Giulian, C. S. Schnohr, G. J. Foran, D. J. Cookson, A. P. Byrne, and M. C. Ridgway, Radiat. Eff. Defects Solids **162**, 501 (2007).

[32] P. Kluth, R. Giulian, D. J. Sprouster, C. S. Schnohr, A. P. Byrne, D. J. Cookson, and M. C. Ridgway, Appl. Phys. Lett. **94**, 113107 (2009).

[33] A. I. Frenkel, C. W. Hills, and R. G. Nuzzo, J. Phys. Chem. B **105**, 12689 (2001).

[34] C. Q. Sun, Prog. Solid State Chem. **35**, 1 (2007).

[35] E. Roduner, Chem. Soc. Rev. **35**, 583 (2006).

[36] C. Langhammer, Z. Yuan, I. Zoric, and B. Kasemo, Nano Lett. **6**, 833 (2006).

[37] I. Lee, F. Delbecq, R. Morales, M. A. Albiter, and F. Zaera, Nat. Mater. **8**, 132 (2009).

[38] J. Y. Chen, B. Lim, E. P. Lee, and Y. N. Xia, Nano Today **4**, 81 (2009).

[39] A. Meldrum, R. F. Haglund, L. A. Boatner, and C. W. White, Adv. Mater. **13**, 1431 (2001).

[40] C. W. White, S. P. Withrow, J. M. Williams, J. D. Budai, A. Meldrum, K. D. Sorge, J. R. Thompson, and L. A. Boatner, J. Appl. Phys. **95**, 8160 (2004).

[41] C. W. White, S. P. Withrow, K. D. Sorge, A. Meldrum, J. D. Budai, J. R. Thompson, and L. A. Boatner, J. Appl. Phys. **93**, 5656 (2003).

[42] S. P. Withrow, C. W. White, J. D. Budai, L. A. Boatner, K. D. Sorge, J. R. Thompson, and R. Kalyanaraman, J. Magn. Magn. Mater. **260**, 319 (2003).

[43] C. W. White, S. P. Withrow, J. D. Budai, D. K. Thomas, J. M. Williams, A. Meldrum, K. D. Sorge, J. R. Thompson, G. W. Ownby, J. F. Wendelken, and L. A. Boatner, J. Appl. Phys. **98** (2005).

[44] C. D'Orleans, C. Cerruti, C. Estournes, J. J. Grob, J. L. Guille, F. Haas, D. Muller, M. Richard-Plouet, and J. P. Stoquert, Nucl. Instr. and Meth. B **209**, 316 (2003).

[45] C. D'Orleans, J. P. Stoquert, C. Estournes, J. J. Grob, D. Muller, C. Cerruti, and F. Haas, Nucl. Instr. and Meth. B **225**, 154 (2004).

[46] C. D'Orleans, J. P. Stoquert, C. Estournes, J. J. Grob, D. Muller, J. L. Guille, M. Richard-Plouet, C. Cerruti, and F. Haas, Nucl. Instr. and Meth. B **216**, 372 (2004).

[47] Y. K. Mishra, D. K. Avasthi, P. K. Kulriya, F. Singh, D. Kabiraj, A. Tripathi, J. C. Pivin, I. S. Bayer, and A. Biswas, Appl. Phys. Lett. **90** (2007).

[48] J. J. Penninkhof, T. van Dillen, S. Roorda, C. Graf, A. van Blaaderen, A. M. Vredenberg, and A. Polman, Nucl. Instrum. Meth. B **242**, 523 (2006).

[49] Y. Chimi, A. Iwase, N. Ishikawa, M. Kobiyama, T. Inami, T. Kambara, and S. Okuda, Nucl. Instrum. Meth. B **245**, 171 (2006).

[50] R. Giulian, P. Kluth, D. J. Sprouster, L. L. Araujo, A. Byrne, and M. C. Ridgway, Nucl. Instrum. Meth. B **266**, 3158 (2008).

[51] M. C. Ridgway, P. Kluth, R. Giulian, D. J. Sprouster, L. L. Araujo, C. S. Schnohr, D. J. Llewellyn, A. P. Byrne, G. J. Foran, and D. J. Cookson, Nucl. Instrum. Meth. B **267**, 931 (2009).

[52] D. J. Sprouster, R. Giulian, B. Johannessen, C. S. Schnohr, L. L. Araujo, P. Kluth, A. P. Byrne, G. J. Foran, and M. C. Ridgway, Phys. Rev. B (submitted in 2009).

[53] D. J. Sprouster, R. Giulian, C. S. Schnohr, P. Kluth, L. L. Araujo, A. P. Byrne, G. J. Foran, and M. C. Ridgway, AIP Conf. Proc. **1092**, 55 (2009).

[54] P. Kluth, C. S. Schnohr, O. H. Pakarinen, F. Djurabekova, D. J. Sprouster, R. Giulian, M. C. Ridgway, A. P. Byrne, C. Trautmann, D. J. Cookson, K. Nordlund, and M. Toulemonde, Phys. Rev. Lett. **101**, 175503 (2008).

[55] K. Awazu, S. Ishii, K. Shima, S. Roorda, and J. L. Brebner, Phys. Rev. B **62**, 3689 (2000).

[56] M. Toulemonde, C. Dufour, and E. Paumier, Acta Phys. Pol. A **109**, 311 (2006).

[57] M. Toulemonde, C. Trautmann, E. Balanzat, K. Hjort, and A. Weidinger, Nucl. Instr. and Meth. B **216**, 1 (2004).

[58] T. van Dillen, A. Polman, P. R. Onck, and E. van der Giessen, Phys. Rev. B **71** (2005).

[59] D. Katz, T. Wizansky, O. Millo, E. Rothenberg, T. Mokari, and U. Banin, Phys. Rev. Lett. **89**, 086801 (2002).

CHAPTER II

LABORATORY-BASED TECHNIQUES

This chapter describes the laboratory-based experimental techniques used for the research outlined in this thesis, namely ion implantation and irradiation, Rutherford backscattering spectrometry (RBS) and transmission electron microscopy (TEM). Background theory for each technique is included, as well as a description of the equipment and procedures involved in the experiments.

2.1 – Ion implantation and irradiation

Ion implantation is a technique generally used to modify the properties of a solid by embedding appropriate atoms into a substrate in the form of ionized particles.[1] The first works regarding the use of energetic ions as a tool, rather than a troublesome side-effect, appeared in the early 1950s,[2, 3] led by the development of the first transistor in 1948, and consequently the need to introduce electrically-active impurities into semiconductors. In 1961, Bredov *et al.*[4] established a distinction between doping and damaging effects produced by ion implantation, observed during O and N implantation in Ge. Since then, ion implantation has been used for a great variety of purposes, from industrial applications like doping of semiconductors to fundamental physics studies including, of course, nanocrystal (NC) formation.

In the 1970s, Arnold and co-workers[5, 6] were the first to report the formation of Au and Ag NCs in silica glass using ion implantation. Only two decades later the properties of nanocomposite materials began to be exploited, generating a vast number of studies that continuously increased over the years.[7, 8] Ion implantation became very widespread in NC formation, mainly due to the ability to control the depth and concentration of implanted ions, as well as the stability offered by the surrounding matrix. In addition, it allows any atom/matrix combination with no solid solubility limitations. NCs can be formed within a substrate when high-fluence implantation creates a solid state supersaturation of impurities (implanted ions).[7] Post-implantation thermal annealing is often required to promote NC growth.

This section describes the ion implantation technique in the light of NC formation and modification. The effects caused by the interaction of energetic ions with solid matter can be classified in two main categories: doping and damaging effects. Throughout this thesis, the term "ion implantation" will be used when the implanted ions are incorporated into the material (doping), at the at.% level. The term "ion irradiation", on the other hand, will only be used when the implanted ions completely transverse the region of interest and only the effects of the deposited energy are considered (damaging).

2.1.1 –Ion-matter interactions

Energetic ions traveling through matter slow down in two distinct ways: transferring energy to the nuclei or electrons of the material via elastic and inelastic collisions, respectively. The latter results in excitation or ionization of the target atoms while the former produces phonons or displaced target atoms, among other defects. Which of the two effects dominates depends upon the energy and mass of the accelerated ion, as well as the mass and atomic number of the medium.[9] Figure 2.1 shows the nuclear and electronic contributions to the total stopping power (energy loss per unit length) as a function of energy for Au ions in SiO_2 (given Pt and Au masses are nearly equal, the energy loss is virtually the same).

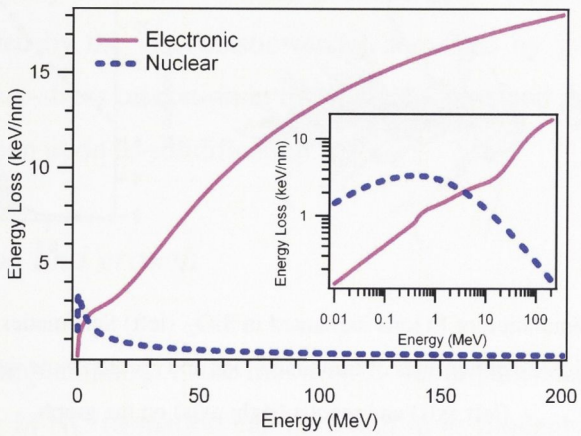

Fig. 2.1 – Nuclear and electronic contributions to the stopping power of Au ions in SiO_2 as a function of energy. The inset shows the same data with a logarithmic scale.

In this work, ion implantation usually involved energies up to 5 MeV (Pt ions). As shown in Fig.2.1, at this energy both elastic and inelastic collisions must be considered. For swift heavy ion irradiation (SHII) in the energy range of 20 – 200 MeV, on the other hand, the electronic stopping power is significantly higher than the nuclear energy loss, hence, the later can be neglected.

Considering both mechanisms as mutually independent, the total energy loss per unit length dE/dx is given by the sum of the individual contributions of nuclear and electronic stopping powers $S_n + S_e$. The range R of an ion in solid matter is usually

defined as the distance traveled by the ion (perpendicular to the surface) before coming to rest.[1] It can be defined as:

$$R = \int_0^E \frac{dE}{(dE/dx)} \tag{2.1}$$

Figure 2.2 shows simulations of 4.5 MeV Pt ions implanted in SiO_2 obtained from the Stopping and Range of Ions in Matter (SRIM 2008[10, 11]) software package. Representative ion trajectories and collision cascades are displayed on the left for 1 and 10 ion impacts, while the depth distributions of implanted ions and recoils (target atoms displaced with non-zero kinetic energy) are displayed on the right for a fluence of $1x10^{17}$ cm^{-2}.

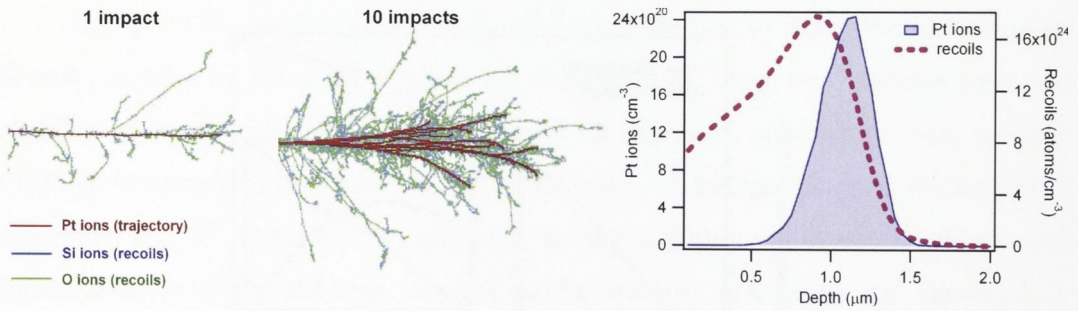

Fig. 2.2 – SRIM[11] simulation of Pt ions implanted in SiO_2. (left) Schematics of ion trajectories with collision cascades; (right) depth profile of implanted ions and recoils. Note the different scales for ions (left axis) and recoils (right axis) on the graph.

The energy transferred to the matrix via electronic energy loss, in the case of Pt ions with initial energy 4.5 MeV, has a maximum close to the surface and decreases in magnitude as the ion penetrates through the material (see Fig. 2.1). With decreasing energy, the nuclear stopping power becomes more pronounced. The nuclear energy loss results in displacement of target atoms which in turn may displace other atoms and so on, in a process known as a collision cascade. The number of atoms displaced varies as a function of depth, reaching a maximum where the maximum nuclear energy is deposited, before the peak concentration of implanted ions (projected range). Energy can also be dissipated via lattice vibrations, known as phonons, which results when an atom receives insufficient energy to be displaced from a lattice site.[12]

Both inelastic and elastic interactions can introduce disorder in matter. The nature of such defects strongly depends on the kind of material (metal, semiconductor, etc.), the structure (crystalline, amorphous, etc.) and the ion energy and mass. Examples of irradiation-induced modification in a-SiO_2 include compaction of the implanted layer[13] due to changes in the bond-angle and bond-length distributions and the formation of defect configurations including O-vacancy centers and non-bridging O-hole centers.[14-17] Such processes are dominated by nuclear stopping or elastic interactions between the incident ion and target nuclei. At high irradiation energies where the energy loss is dominated by electronic stopping, additional irradiation-induced structural modifications can include anisotropic plastic deformation[18] and latent track formation.[19] Changes in shape have been observed in silica colloids (from tens to hundreds of nm) under SHII. For increasing irradiation fluence the dimension perpendicular to the ion beam grows while the dimension parallel shrinks with no significant mass density changes.[20-23] Such phenomenon is also called ion hammering and is best explained by the viscoelastic model described by Trinkaus *et al.*[20] which accounts for the shear-stress relaxation in the fluid ion track and the subsequent freezing of the relaxation strain upon re-solidification.

2.1.2 – Nucleation and growth

During ion implantation, if the mobility of the implanted species is high, phase separation resulting in NC formation can be found in as-implanted samples. However, fabrication of NC by ion implantation often requires a thermal treatment to induce phase separation of implanted atoms. The mean NC size is the result of a complicated correlation between the impurity diffusion length during a flux-dependent time and the nucleation rate, which depends on temperature and degree of supersaturation. Consequently, the implantation temperature often contributes significantly to the mean NC size, as does the post thermal annealing.

In the classical nucleation theory from a supersaturated solution, the precipitation of NCs with radii exceeding the critical radius is followed by NC growth via draining of the supersaturated solution.[24] NCs can grow without competing effects while the supersaturation is large. However, when the supersaturation degree is reduced,

NC evolution is then governed by its chemical potential, where the solute concentration around a spherical NC of radius R_{NC} is given by the Gibbs-Thomson relation:

$$C(R_{NC}) = C_{\infty}\left(1+\frac{R_C}{R_{NC}}\right) \tag{2.2}$$

where C_{∞} is the solubility at a flat interface and R_C is the capillary length. As the equilibrium concentration at the NC surface scales with inverse NC size, the large NCs grow at the expense of the smaller ones. This process is called Ostwald ripening (if the total mass is conserved).

During ion irradiation, a NC can be considered as a source of solute. Recoils and collision cascades cause the ballistic ejection of atoms from the original NC and their deposition in the surrounding matrix. When the solute concentration overcomes the solubility threshold, the nucleation of the new phase can occur. However, the irradiation also affects the NC stability. The steady-state concentration of a NC under irradiation can be represented by:

$$C^*(R_{NC}) = C^*_{\infty}(R_{NC})\left(1+\frac{R^*_C}{R_{NC}}\right) \tag{2.3}$$

where C^*_{∞} and R^*_C are the solubility at a flat interface and the capillary length under irradiation, respectively. The model predicts that below a critical temperature the capillary length can be negative. This reverses the chemical potential gradient, favoring the small NCs to grow at the expense of the large ones. This effect, known as inverse Ostwald ripening, has been used to tailor the size of embedded NCs.[7, 25, 26]

2.1.3 – Ion track formation

During SHII, the ion-matter interaction is completely dominated by inelastic collisions. For very energetic ions (above tens of MeV), the electronic energy loss varies smoothly in the near surface region and thus the energy deposited in a thin layer (< 2μm) can be considered constant to a good approximation. Energy is transferred to

the electrons of the material over a time scale of 10^{-17} – 10^{-13} s and is concentrated in a region of a few nanometers around the ion path. In this region, the target atoms are highly excited or ionized, as illustrated in Fig.2.3. For ion energies between 1 and 30 MeV/u about 30-40% of the total stopping power is deposited in primary excitations and/or ionizations of the target atoms while the rest goes into kinetic energy of ejected electrons.[27]

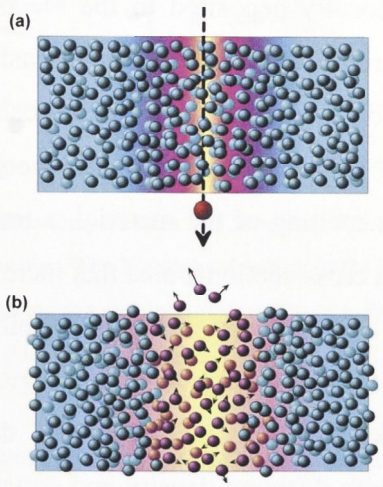

Fig. 2.3 – Schematics of ion track formation due to SHII. (a) ion passing through the material producing ionization, (b) atomic motion in the region around the ion track.
(figure extracted from G. Schiwietz *et al.*[28])

The mechanism behind the energy transfer from the electronic to the atomic system can be explained using three distinct routes, named *Coulomb explosion*, *athermal melting* and *thermal spike model*. According to the Coulomb explosion model, for sufficiently high energy deposition, the energy transferred to the electrons ionizes the target atoms so that they become positively charged and their mutual repulsion results in atomic motion (when charge recombination times are sufficiently long).[28, 29] This process is considered the fasted among the three, happening immediately after the ionization. It assumes a radial, coherent motion of all atoms in the core, corresponding to an almost instantaneous mechanical loading of the core, releasing an outgoing shock wave while the core undergoes vivid vibrations.[30] The Coulomb explosion model alone has not been able to predict, for example, the track radius in insulators and amorphous materials.[27]

Athermal melting is a model that considers atomic motion as a result of the large forces originating from the differences between the interatomic potential of atoms in the track core and the equilibrium potential. This is because the atoms at the track core, even after the re-establishment of charge neutrality, have electrons that are not in their lowest energy states. This mechanism happens in a time frame of 10^{-14} s, which is considered too rapid to be mediated by phonons, and hence is called *athermal*.[27]

The thermal spike model is based on the electron-phonon energy transfer mechanism. The energy locally deposited to the electrons is quickly shared among electrons by electron-electron interactions and then transferred to the lattice by electron-phonon and phonon-phonon interactions, in a time scale of 10^{-13}-10^{-11} s.[12, 28, 29, 31, 32] According to the thermal spike model, when the energy involved in atomic motion exceeds that necessary for melting of the material, a track of molten matter is formed around the ion path, with a cross-sectional area that increases with increasing S_e.[33, 34] In amorphous materials, like a-SiO_2, the low electron mobility allows the energy deposited in the system to be confined long enough to form a region heated transiently. The rapid quench of the molten track (10^{-11} – 10^{-8} s) "freezes-in" the disordered atoms, producing a region rich in defects, with different density and structure in some cases. Significant atomic rearrangements due to SHII have not been observed in elemental bulk crystalline metals, possibly due to the large heat conductivity and electron mobility (charge recombination/neutralization) of the material.[33]

It is important to bear in mind that Coulomb explosion and athermal melting can also produce a thermal spike. Even though these two processes start with a coherent and collective motion, collisions between atoms tend to randomize their energy so that on a picossecond time-scale a thermalized motion could occur. In this sense Coulomb explosion and thermal spike may simply denote early and late stages of track formation.[27, 29]

The electronic and lattice temperatures for bulk a-SiO_2 irradiated with 110 MeV Br ions (S_e = 9.2 keV/nm) are shown in Fig. 2.4 as a function of distance from the ion path (data extracted from calculations by Awazu *et al*[35] using the thermal spike model). The data shown if Fig. 2.4 corresponds to the maximum temperature that the electrons and lattice can achieve, the first happening at approximately 10^{-15} s while the second taking place at around 10^{-13} s after the passage of the ion. The highlighted region in Fig.

2.4(b) indicates the radius of the molten track (~2.65 nm), considering the melting temperature of a-SiO_2 to be 1972 K.

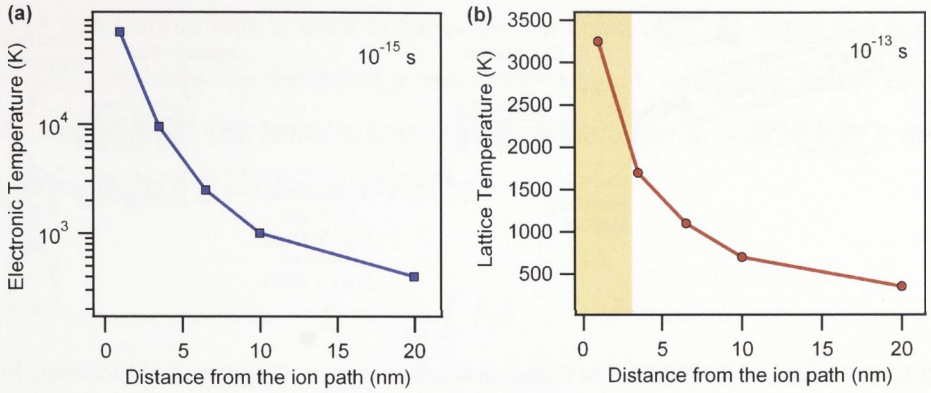

Fig. 2.4 – (a) Electronic and (b) lattice temperatures as a function of distance from the ion path for bulk a-SiO_2 irradiated with 110 MeV Br ions. The highlighted region in (b) indicates the molten track radius (2.65 nm), considering the melting temperature of a-SiO_2 to be 1972 K.
(Data extracted from Awazu *et al.*[35])

Similar calculations were also performed for bulk Au under the same irradiation conditions. Despite the significantly higher energy loss (S_e = 29.2 keV/nm), the simulated lattice temperature does not exceed the melting temperature of Au, most likely because the thermal conductivity of both the electronic and the lattice subsystems are much larger than that of a-SiO_2.[35]

2.1.4 – Ion accelerators

The ion implantations and irradiations for this thesis were performed at the Australian National University (ANU). Ion implantations were carried out using a 1.7 MV NEC tandem accelerator located at the Department of Electronic Materials Engineering, a schematic of which is shown in Fig. 2.5.

Negative ions are produced from a solid cathode in which the material is usually compressed into a Cu holder inserted in a SNICS source (Source of Negative Ions by Cesium Sputtering). Cs vapor from a molten Cs reservoir is incident onto the surface of the ionizer maintained at a temperature of ~1100 °C. Cs^+ ions are created and accelerated towards the negatively biased cathode (approximately - 5 kV). Atoms and ions (both positively and negatively charged) are sputtered from the cathode surface.

Negative ions are accelerated from the cathode, then extracted and focused by an extraction potential of ~10 kV and a bias potential of ~ 65 kV.

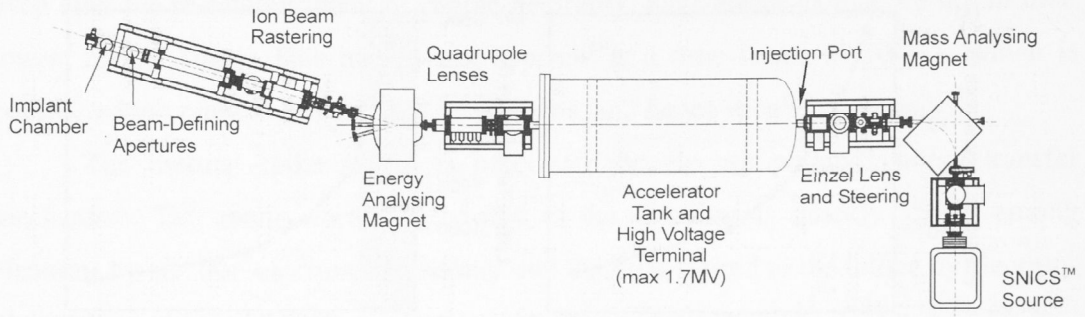

Fig. 2.5 – Schematic of the NEC 1.7 MV tandem accelerator at the Department of Electronic Materials Engineering, Australian National University

The accelerated ions pass through the field of a 90° magnet, with bending radius R. The magnetic field B can be adjusted to allow the transmission of ions with mass m and charge q according to:

$$B = \frac{1}{R}\sqrt{\frac{2m\,V_i}{eq}} \tag{2.4}$$

where e is the electronic charge and V_i is the potential of the ions. The transmitted ions pass through an Einzel lens (for focusing) and X/Y electrostatic steerers before entering the accelerating tube consisting of numerous equi-potential rings, separated by insulators and resistors, which provide a uniform potential gradient along the tube. In the middle of the tank resides the high voltage terminal (maximum 1.7 MV), positively charged by four pelletron[§] chains. The beam of negative ions is accelerated towards the positively charged terminal where they are partially stripped of electrons, becoming positively charged. The positive ions are then repelled by the positive terminal and receive an additional acceleration towards the end of the tank where the final energy of the ions Ei_f is:

[§] Pelletron chains are made of metal pellets connected by insulating nylon links and are charged by an induction scheme that does not use rubbing contacts or corona discharges. It was developed in the mid 1960s as an improvement over the older Van de Graaff charging belts.

$$Ei_f = e[V_i + (1+q)V_t] \tag{2.5}$$

where V_t is the terminal voltage.

A quadrupole lens is used to focus the ion beam onto the target that is placed in the implant chamber. A 15° energy analyzing magnet is used to select ions of the desired charge state. The beam is scanned across the target in both X and Y directions. The implant fluence Q can be calculated by:

$$Q = \frac{1}{qAe}\int_0^t I\,dt \tag{2.6}$$

where I is the beam current and A the area implanted. The temperature of the sample can be adjusted from -170 °C to 500 °C and the pressure in the target chamber is typically maintained at 10^{-7} Torr.

The ion irradiations (SHII) were performed at the Department of Nuclear Physics, using a 14 MV NEC tandem accelerator, whose picture is shown in Fig. 2.6. The principles of operation of the 14 MV are basically the same as described for the 1.7 MV tandem accelerator. The maximum terminal voltage of 14 MV allows the acceleration of ions to energies of up to 200 MeV (Au^{+13}).

Fig. 2.6 – Picture of the 14 MV NEC tandem accelerator at the Department of Nuclear Physics, Australian National University. The man standing beside the equipment demonstrates the dimensions of the machine.

2.2 – Rutherford backscattering spectrometry

Rutherford backscattering spectrometry (RBS) is a versatile technique using energetic ions for (usually) non-destructive materials analysis. Based on classical scattering theory, it provides information about elemental composition as a function of depth. When energetic ions are incident on a target, most of the ions are incorporated into the material at a certain depth (ion implantation). A few ions (~1 in each 10,000), however, are backscattered due to the collision between the light impinging ion and the more massive target nuclei. In the process, the incident ions transfer part of their energy to the stationary target atoms. The detection of the number and energy of backscattered ions provides a signature of the elemental composition of the sample, as described below.[36]

2.2.1 – Basic principles

The schematic of Fig. 2.7 shows the notation and geometry for the laboratory system of coordinates, where E_0 and M_1 denote the energy and mass of the incident ion, M_2 is the mass of the target atom, E_1 is the energy of the ion backscattered at a depth Δx and θ is the angle between the incident and scattered ion trajectories. The energy of the incident ion immediately before the collision with a target atom at a depth Δx is denoted by E.

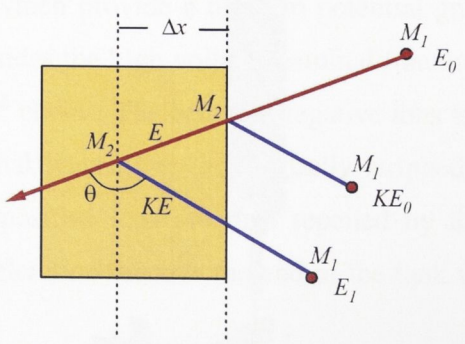

Fig. 2.7 – Schematics of an elastic collision between a projectile of mass M_1 and energy E_0 and a target mass M_2. θ represents the angle between the incident and scattered ion trajectories.

After the collision, the energy of the backscattered ions is reduced by a factor K, also called kinematic factor, which can be calculated via conservation of energy and momentum, yielding:

$$K = \left(\frac{\sqrt{M_2^2 - M_1^2 \sin^2 \theta} + M_1 \cos \theta}{M_2 + M_1} \right)^2 \tag{2.7}$$

The probability of a collision between the incident ion and the target atom, or scattering cross-section $\sigma(\theta)$, is given by:

$$\sigma(\theta) = \left[\frac{Z_1 Z_2 e^2}{4E} \right]^2 \frac{4}{\sin^4 \theta} \frac{\left[\sqrt{1 - (M_1/M_2 \sin \theta)^2} + \cos \theta \right]^2}{\sqrt{1 - (M_1/M_2 \sin \theta)^2}} \tag{2.8}$$

considering a Coulomb potential $V = \frac{Z_1 Z_2 e^2}{r}$ where Z_1 and Z_2 correspond to the atomic number of the incident ion and the target atom, respectively, e is the electron charge, r is the distance between the two particles and E is the incident ion kinetic energy.

Figure 2.8 shows a typical RBS spectrum of an SiO_2 sample for 2 MeV He^+ ions. The inset shows a schematic of the incident and scattered ions at the surface and at a depth Δx.

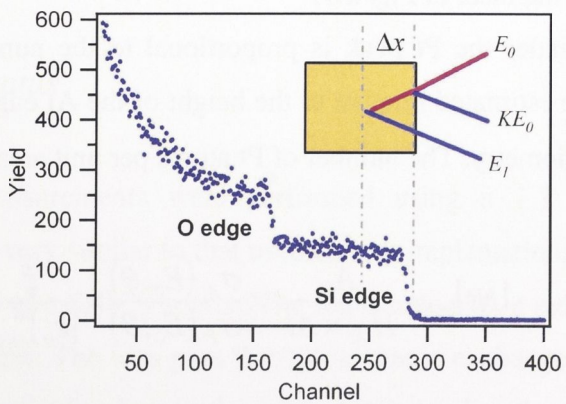

Fig. 2.8 – Typical RBS spectrum of an SiO_2 sample. The inset shows a schematic of the incident and scattered ion trajectories and the corresponding energies after a collision with a surface atom and an atom at a depth Δx.

The energy transfer during the collision is given by K (Eq. (2.7)). Ions with incident energy E_0 that are backscattered by surface atoms thus have a final energy KE_0. For ions that backscatter inside the material, however, a further decrease in energy must be considered, to account for the energy loss on the way in and out of the sample. The incident ions lose a greater amount of energy when colliding with lighter target atoms (conservation of energy and momentum). Therefore, the signal from different atomic species (O and Si in this case) appear in different channels (the channel number is proportional to the energy of the backscattered ions). The height H of the signal from each element is proportional to the number of collisions with that particular target atom in a thickness Δx, given by:

$$H = Q\Omega\sigma(\theta)N\Delta x \tag{2.9}$$

where Q is the total number of incident ions, Ω is the solid angle of the detector and N is the number of target atoms per unit volume. Using Eq. (2.9) enables the calculation of the absolute atomic composition if Ω, $\sigma(\theta)$ and Q are well know. However, the uncertainties associated with Ω and Q can be non-negligible and thus a relative measurement, as described below, is more commonly used.

It is also possible to estimate atomic concentrations relative to the amount of other elements in the same sample. Figure 2.9 shows the RBS spectrum for Pt implanted in Al_2O_3 to a total fluence of $1x10^{16}$ cm^{-2}. The peak concentration of Pt ions is located at around 0.1 μm from the surface, according to SRIM 2008[11] simulations, a schematic of which is shown in the inset of Fig. 2.9.

The area under the Pt peak is proportional to the number of Pt atoms in the sample and can be estimated relative to the height of the Al edge, as the substrate has a well known stoichiometry. The number of Pt atoms per unit area $[Nt]_{Pt}$ is given by:

$$[Nt]_{Pt} = \frac{A_{Pt}}{H_{Al} \times Al} \times \frac{\sigma_{Al}(E_0,\theta)}{\sigma_{Pt}(E_0,\theta)} \times \frac{\xi}{[\varepsilon_0]^{Al}_{Al_2O_3}} \tag{2.10}$$

where A_{Pt} is the area under the Pt peak, H_{Al} corresponds to the edge height of the substrate element (Al in this example), Al is the Al atomic concentration, $\sigma_{Al}(E_0,\theta)$

and $\sigma_{Pt}(E_0,\theta)$ are the Rutherford scattering cross-sections given by Eq. (2.8) for the substrate and impurity elements, respectively, considering a surface energy approximation. ξ is the energy calibration (keV/channel) and $[\varepsilon_0]^{Al}_{Al_2O_3}$ is the stopping cross-section factor for He scattering from Al atoms and losing energy in Al_2O_3. The concentration ratio estimated using Eq. (2.10) clearly does not require a precise measurement of Ω, and Q.

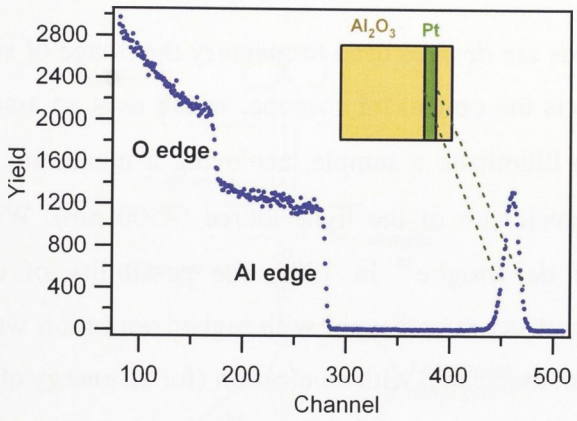

Fig. 2.9 – RBS spectrum of Pt implanted in Al_2O_3 with peak concentration at 0.1 μm from the surface. RBS measurement performed using 2 MeV He^+ ions.

Composition depth profiles can be easily obtained from RBS spectra, yielding valuable insights on, for example, diffusion, redistribution of implanted ions and layer composition. Details on the conversion from channel to depth scale can be found elsewhere.[36, 37]

2.2.2 – RBS apparatus

The RBS measurements were performed using a 1.7 MeV NEC tandem accelerator (1.7 MV) very similar to that used for ion implantation, but equipped with a He gas source instead of a SNICS source. The ion source uses a radio frequency field to positively ionize He gas. The ions pass through a charge exchange chamber containing Rb vapor, which negatively charges the ions. After passing through the accelerating tube, He ions with energies from 1 – 5 MeV are readily attainable. Backscattered ions are collected by a Si surface-barrier detector positioned at a scattering angle of 168°.

The ions impinge on the detector creating electron-hole pairs that are swept from the depletion region by an applied electric field. The resulting current pulse is amplified and sorted in a multi-channel analyzer as a function of voltage, which is proportional to the energy of the scattered ions. Calibration curves to convert channel to energy can be easily obtained by analyzing materials with well known elemental composition.

2.3 – Transmission electron microscopy

Microscopes are devices used to magnify the image of small samples. The most common example is the optical microscope, which uses an assortment of lenses and a source of light to illuminate a sample, achieving a maximum resolution of ~0.2 μm, limited by the wavelength of the light source (~500 nm). With the wave – particle duality theory of de Broglie[38] in 1925, the possibility of using other sources of illumination to construct microscopes with higher resolution was made possible, given that the wavelength associated with an electron (for an energy of 100 keV) is five orders of magnitude less than that of visible light.[39] The idea of an electron microscope was first proposed by Knoll and Ruska[40] in 1932, rendering Ruska a Nobel prize in 1986.

Transmission electron microscopy (TEM), now a widely used and important tool in materials research as well as in many other fields, enables a variety of imaging and analytical capabilities including bright and dark field imaging, micro diffraction, as well as energy dispersive x-ray analysis (EDAX) for the determination of elemental composition.[39]

2.3.1 – TEM apparatus

Figure 2.10 shows a schematic diagram of a transmission electron microscope, which resembles a transmission optical microscope in many ways. The electron beam is generated in the electron gun by thermionic emission using a lanthanum hexaboride (LaB_6) crystal (for its low work function). Magnetic lenses are used to control the trajectory of the electrons in a similar way as glass lenses are used in an optical microscope.

The first set of lenses, called condenser lenses, demagnify the source image and project it over an aperture that selects the spot size. The objective lens is responsible for most of the magnification. Since its focal length is very small, the sample is positioned very close or even inside the lens. Intermediate and projector lenses act in various combinations to vary the imaging and diffraction conditions. The image is projected on a fluorescent screen that can be viewed through a glass window. A CCD camera or photographic film, positioned bellow the fluorescent screen, is used to record images.

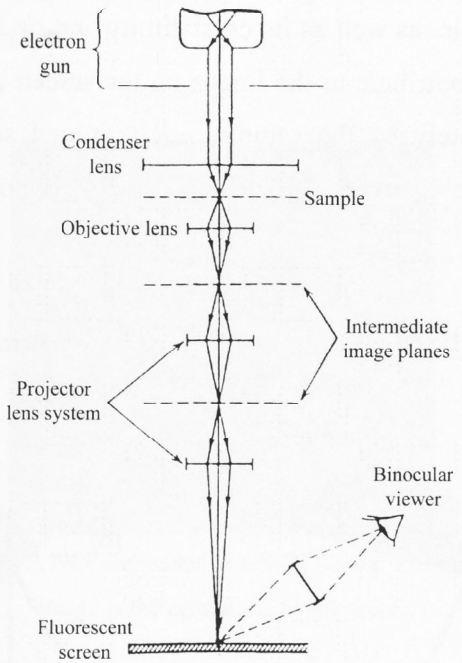

Fig. 2.10 – Schematic of a transmission electron microscope.

2.3.2 – Image formation

Similar to energetic ions, electrons also lose energy when passing through matter via elastic and inelastic collisions. Elastic scattering can occur either by interactions with single atoms or with the specimen as a whole. The former include interactions with the electron cloud, resulting in small angular deviation or with the nucleus, in which case the stronger Coulomb force yields higher angular deflections. Inelastic scattering often involves ionization of the target atoms, hence energy loss, yielding mainly characteristic x-rays as well as secondary electron emission. This form of interaction

allows the use of TEM for analytical purposes, yielding information on the atomic composition.[39]

Image contrast can be obtained either by selecting or excluding specific electrons from the imaging system. Bright field (BF) or dark field (DF) images can be formed by direct or scattered electrons, respectively, as shown in Fig. 2.11.

The uniform electron intensity in the incident beam is transformed into a nonuniform intensity after scattering by the specimen. This variable electron intensity translates into contrast on the viewing screen. When the electron beam interacts with a thin sample, the fraction of electrons that pass through is determined by the mass and thickness of the sample, as well as its crystallinity and orientation. In BF, for example, the electrons which contribute to the image on the screen are those which have neither been stopped completely by the sample, nor scattered so far that they do not pass through the objective aperture. In DF, the image is formed by selected scattered electrons.

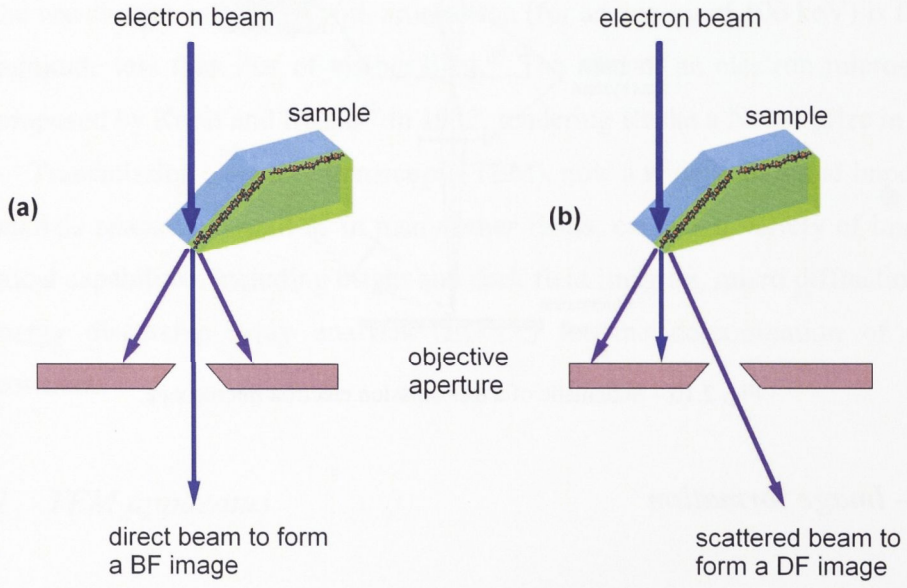

Fig. 2.11 – Schematic of (a) bright field and (b) dark field image formation (not to scale).

TEM imaging analysis relies, basically, on image contrast. A variety of features on the sample can affect image contrast, from which the respective characteristics can be identified. The mass contrast, for example, allows the distinction between high and low atomic number regions, like Pt nanocrystals embedded in a-SiO_2, as shown the BF image in Fig. 2.12. Local variations in the sample thickness, for example wedge-shaped

samples, can create thickness contours in the image (also called thickness fringes). Such phenomenon results from periodic variations in the intensity of the diffracted beam with increasing sample thickness. Given the complementary nature of the direct and diffracted beams, thickness fringes are apparent in both BF and DF image modes, and allow the evaluation of the sample thickness by measuring the distance between dark and bright lines. In a similar way, bend contours occur when a particular set of diffracting planes is not parallel everywhere in the sample (when the sample is bent). Diffraction contrast plays an important role in crystalline samples, in which case the relationship between the image and the diffraction pattern (discussed in the next section) is most critical.

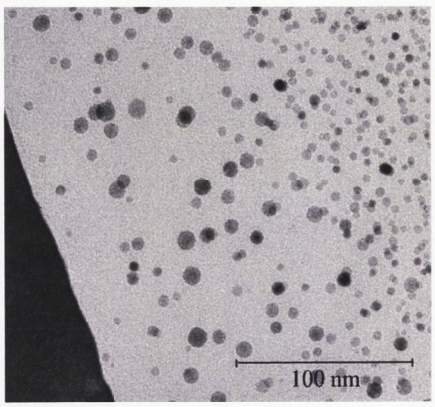

Fig. 2.12 – BF TEM image of Pt NCs embedded in a-SiO_2 matrix. The dark region on the left of the image is the crystalline Si substrate.

Contrast can also arise from differences in the phase of the scattered electrons, often called phase contrast, from which the atomic structure of crystalline materials can be investigated. This imaging mode requires the selection of more than one beam (direct + scattered), which by interference produce an image that reflects the lattice spacing of the crystal (given the crystal is favorably aligned with the electron beam). Lattice fringes are often used to identify crystallinity, as apparent in Fig. 2.13. Other phase contrast features can also be present when, for example, two crystallographic planes of nearly or identical periodicities are superimposed. Such interference patterns, known as Moiré patterns, are schematically illustrated in Fig. 2.14 by two sets of misfit[**] lines parallel to each other (Fig. 2.14(a)), two sets of misfit lines rotated (Fig. 2.14(b)) and two sets of identical lines rotated (Fig. 2.14(c)).

[**] The term misfit here means two sets of parallel lines with slightly different spacing.

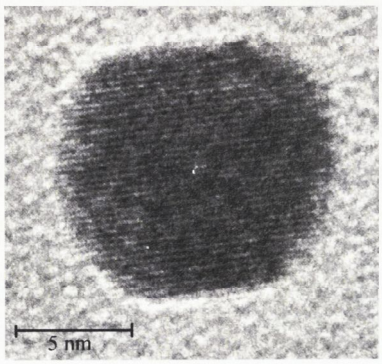

Fig. 2.13 – High resolution TEM image of C supported Pt NC.

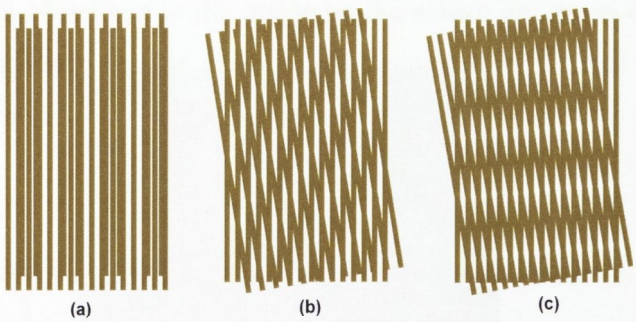

Fig. 2.14 – Moiré patterns: (a) two misfit sets of lines aligned, (b) two misfit sets of lines rotated and (c) two identical sets of lines rotated.

As shown in Fig. 2.14, the superposition of two sets of lines either identical but rotated by a small angle or misfit (aligned or rotated) can generate a pattern that differs from the one observed from a single set of lines. Moiré patterns can be observed with embedded Pt NCs when two NCs (or two crystal grains in the same NC) happen to be aligned and superimposed.

2.3.3 – Electron diffraction

A great advantage of transmission electron microscopy is the capability to obtain information on real space (electron microscope images) and reciprocal space (diffraction pattern) for the same region (using the appropriate combination of lenses and apertures). When the electron beam passes through a thin crystalline sample, the electrons are diffracted by the crystal potential, forming diffraction spots on the back focal plane, in a region between the objective lens and the image plane. Electron

diffraction can be interpreted in a similar way as x-ray or neutron diffraction. According to Bragg's law:

$$2\sin\theta_B = \frac{\lambda}{d} \tag{2.11}$$

constructive interference occurs at an angle θ_B, where λ is the electron wavelength and d is the interplanar distance in the crystal.

Figure 2.15 shows diffraction patterns for crystalline Si (Fig. 2.15(a)) and Pt NCs (3 – 5 nm diameter) embedded in a-SiO_2 (Fig. 2.15(b)). The former shows distinct spots resulting from the long range order of a Si crystal oriented along the [111] zone axis. The rings apparent in Fig. 2.15(b) correspond to the FCC structure of Pt NCs. Each ring represents a different plane in the crystal structure, resulting from the overlap of innumerous spots coming from randomly oriented nanocrystals.

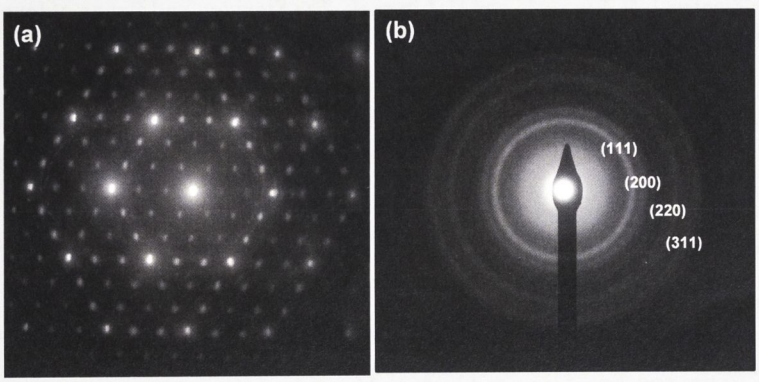

Fig. 2.15 – Diffraction pattern of (a) crystalline Si and (b) Pt NCs embedded in a-SiO_2.

TEM diffraction allows the study of selected areas as small as a few tens of nanometers. This is particularly useful for the study of NCs, where the large size distributions and small dimensions can often degrade results obtained by other techniques like conventional x-ray diffraction. Such results reflect the average of a large ensemble of NCs.[41]

References

[1] G. Dearnaley, J. H. Freeman, R. S. Nelson, and J. Stephen, *Ion Implantation* (North-Holland Publishing Company, Amsterdam, 1973).

[2] R. Ohl, Bell. Syst. Tech. J. **31**, 104 (1952).

[3] W. D. Cussins, Proc. Phys. Soc. London B **68**, 213 (1955).

[4] M. M. Bredov, V. A. Lepilin, I. B. Shestakov, and A. L. Shakh-Budagov, Soy. Phys. Solid State **3**, 195 (1961).

[5] G. W. Arnold, J. Appl. Phys. **46**, 4466 (1975).

[6] G. W. Arnold and J. A. Borders, J. Appl. Phys. **48**, 1488 (1977).

[7] A. Meldrum, R. F. Haglund, L. A. Boatner, and C. W. White, Adv. Mater. **13**, 1431 (2001).

[8] E. Roduner, Chem. Soc. Rev. **35**, 583 (2006).

[9] H. Ryssel and I. Ruge, *Ion Implantation* (John Wiley & Sons, Chichester, 1986).

[10] J. F. Ziegler, J. P. Biersack, and U. Littmark, *The Stopping and Range of Ions in Solids* (Pergamon Press, New York, 1985).

[11] www.srim.org.

[12] G. J. Dienes and G. H. Vineyard, *Radiation Effects in Solids* (Interscience Publishers Inc., New York, 1957).

[13] C. M. Johnson, M. C. Ridgway, and P. W. Leech, Appl. Phys. Lett. **69**, 984 (1996).

[14] R. A. B. Devine, Nucl. Instr. and Meth. B **91**, 378 (1994).

[15] R. A. B. Devine and M. H. Debroux, J. Appl. Phys. **54**, 4197 (1983).

[16] R. A. B. Devine, Appl. Phys. Lett. **43**, 1056 (1983).

[17] R. A. B. Devine and A. Golanski, J. Appl. Phys. **55**, 2738 (1984).

[18] A. Benyagoub, S. Loffler, M. Rammensee, S. Klaumunzer, and G. Saemannischenko, Nucl. Instr. and Meth. B **65**, 228 (1992).

[19] S. Klaumunzer, Nucl. Instr. and Meth. B **225**, 136 (2004).

[20] H. Trinkaus and A. I. Ryazanov, Phys. Rev. Lett. **74**, 5072 (1995).

[21] S. Klaumunzer, Nucl. Instr. and Meth. B **215**, 345 (2004).

[22] E. Snoeks, A. Polman, and C. A. Volkert, Appl. Phys. Lett. **65**, 2487 (1994).

[23] T. Van Dillen, E. van der Giessen, P. R. Onck, and A. Polman, Phys. Rev. B **74**, 132103 (2006).

[24] I. M. Lifshitz and V. V. Slyozov, J. Phys. Chem. Solids **19**, 35 (1961).

[25] G. Rizza, H. Cheverry, T. Gacoin, A. Lamasson, and S. Henry, J. Appl. Phys. **101**, 014321 (2007).

[26] K. H. Heinig, T. Muller, B. Schmidt, M. Strobel, and W. Moller, Appl. Phys. A **77**, 17 (2003).

[27] S. Klaumunzer, Nucl. Instr. and Meth. B **225**, 136 (2004).

[28] G. Schiwietz, K. Czerski, M. Roth, F. Staufenbiel, and P. L. Grande, Nucl. Instr. and Meth. B **225**, 4 (2004).

[29] E. M. Bringa and R. E. Johnson, Phys. Rev. Lett. **88** (2002).

[30] R. Bullough and J. J. Gilman, J. Appl. Phys. **37**, 2283 (1966).

[31] M. Toulemonde, C. Dufour, and E. Paumier, Acta Phys. Pol. A **109**, 311 (2006).

[32] C. Dufour, A. Audouard, F. Beuneu, J. Dural, J. P. Girard, A. Hairie, M. Levalois, E. Paumier, and M. Toulemonde, J. Phys.: Condens. Matter **5**, 4573 (1993).

[33] M. Toulemonde, C. Dufour, and E. Paumier, Phys. Rev. B **46**, 14362 (1992).

[34] M. Toulemonde, C. Dufour, E. Paumier, and F. Pawlak, Mat. Res. Soc. Symp. Proc. **504**, 99 (1998).

[35] K. Awazu, X. M. Wang, M. Fujimaki, J. Tominaga, H. Aiba, Y. Ohki, and T. Komatsubara, Phys. Rev. B **78**, 8 (2008).

[36] L. C. Feldman and J. W. Mayer, *Fundamentals of surface and thin film analysis* (North-Holland, New York, 1986).

[37] J. R. Bird and J. S. Williams, *Ion beams for materials analysis* (Academic Press, Sydney, 1989).

[38] L. de Broglie, Ann. de Physiques **3**, 22 (1925).

[39] D. B. Williams and C. B. Carter, *Transmission Electron Microscopy* (Plenum Press, New York, 1996).

[40] M. Knoll and E. Ruska, Z. Physik **78**, 318 (1932).

[41] L. A. Bendersky and F. W. Gayle, J. Res. Natl. Stand. Technol. **106**, 997 (2001).

CHAPTER III

SYNCRHOTRON-BASED TECHNIQUES

The fundamental principles of synchrotron radiation and some examples of applications to materials analysis are described in this chapter. The small-angle x-ray scattering and x-ray absorption spectroscopy techniques (extended and near edge regions) are explained in the light of NC characterization, including details of the apparatus for each technique.

3.1 – Synchrotron radiation

A synchrotron is a particular type of cyclic particle accelerator in which the electric and magnetic fields (used to accelerate the particles and maintain their circular trajectory, respectively) are carefully synchronized with the traveling particle beam. The radiation emitted by the accelerated charged particles (usually electrons or positrons) is more than five orders of magnitude greater than conventional sources like x-ray tubes and can be used in a broad range of fields, including materials analysis, medical applications as a substitute for conventional x-ray imaging and many more.[1] Synchrotron radiation (SR) offers a brilliant, collimated, pulsed, polarized, continuous* spectrum for a variety of techniques, among them x-ray absorption spectroscopy (XAS) and small-angle x-ray scattering (SAXS), which are described in the present chapter.

3.1.1 – Historical overview

The idea of electromagnetic radiation being produced by charged particles in circular motion dates back to the early 1870s with Maxwell.[2] In 1898 Liénard[3] published a simplified version of the complicated algebraic equations, which allowed the direct use of the theory to calculate field patterns produced by moving charges. The first experimental evidence of SR, however, dates from almost 50 years later, in the General Electric Company Research Laboratory. Using a 70 MeV synchrotron accelerator in 1947, Elder and coworkers[4, 5] observed a small bright spot through the glass vacuum vessel. The visible beam of SR was an immediate sensation, attracting the attention of many researchers.[6]

The development of a comprehensive theoretical treatment and the construction of electron accelerators in the early 1950s aroused much interest in SR. The use of storage rings (late 1960s) offered superior research opportunities including constant spectral distribution, stability and relatively low radiation hazard compared to the earlier apparatus. In most cases, however, the primary function of the synchrotron was high-energy physics research.[1] This period was later classified as the first generation of SR.

* Continuous here means any wavelength from infrared to x-rays.

The second generation began with the construction of sources exclusively dedicated to SR, the first of which was installed at the University of Tokyo and operated from 1976 to 1997. The main body of the equipment is now on display at the Spring8 Synchrotron Facility, Japan, as shown in Fig. 3.1 (picture taken in September 2007 at the 1st Cheiron School organized by the Asia Oceania Forum for Synchrotron Radiation Research (AOFSRR)).

Fig. 3.1 – First dedicated synchrotron equipment on display at the Spring8 – Japan. Picture taken during the 1st AOFSRR Cheiron School – Sep 2007.

With the advent of dedicated light sources, the accelerators were optimized to offer higher stability and brightness (photons per second per solid angle), stimulating the development of novel research techniques as well as renewing those already established on laboratory-based sources such as x-ray crystallography.[1]

The use of wigglers and undulators as insertion devices (as explained in detail below) defined the beginning of third generation light sources. Second generation light sources started to be upgraded to meet the full capability of the new insertion devices, as these rings were not designed specifically with low emittance (product of the transverse size and the angular divergence of the electron beam). New facilities were built to provide more powerful SR. The Spring8 – Japan storage ring, operational since 1997, is currently the largest third generation synchrotron facility, with 8 GeV electrons traveling around a storage ring of circumference 1,436 m. (Fig. 3.2).

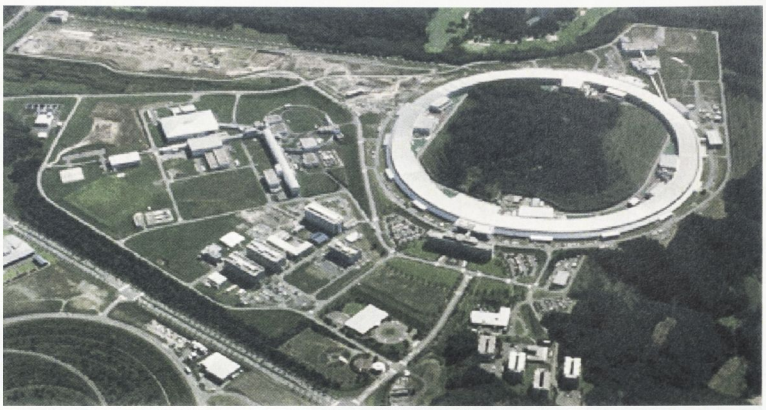

Fig. 3.2 – Aerial view of the Spring8 – Japan.

The fourth generation light source is still in development, with research under way in many laboratories around the world. Some designs utilize free electron lasers with a very long undulator in a high-energy linear electron accelerator and aim at providing a peak brightness many orders of magnitude beyond that of the third generation sources, as well as coherent radiation with a pulse length of 100 fs or less (usually the pulse length for a third generation synchrotron is ps).

3.1.2 – Basic principles

A charged particle generates an electric field $\vec{E}$ whose magnitude decreases outwardly. The electric $\vec{E}$ and magnetic $\vec{B}$ fields associated with charges are given by Maxwell's equations:

$$\begin{aligned} \nabla \cdot \vec{E} &= \frac{\rho}{\mu_0} \\ \nabla \cdot \vec{B} &= 0 \\ \nabla \times \vec{E} &= -\frac{\partial \vec{B}}{\partial t} \\ \nabla \times \vec{B} &= \mu_0 \vec{J} + \mu_0 \varepsilon_0 \frac{\partial \vec{E}}{\partial t} \end{aligned} \tag{3.1}$$

where ρ is the charge density, $\vec{J}$ is the current density and μ_0 and ε_0 are the magnetic and electric constants, respectively. If the particle is at rest, the time derivation of $\vec{E}$ is zero, thus the magnetic field is zero and no energy is lost, only information is transferred. When a charged particle orbits in a circular trajectory a spiral-shaped electric field is generated, which is condensed in a bright spiral zone if the particle velocity approaches the speed of light. This is synchrotron radiation. When the particle is periodically deflected from its trajectory (traversing an undulator, for example), radiation is generated with each bend. If the velocity of the particle is relativistic, the wavelength of the accumulated periodic radiation becomes very short due to Doppler effects. All three situations are depicted in Fig. 3.3, which shows snapshots from Radiation 2D, a simulation program used to visualize the electric fields generated by charged particles in motion.[7, 8]

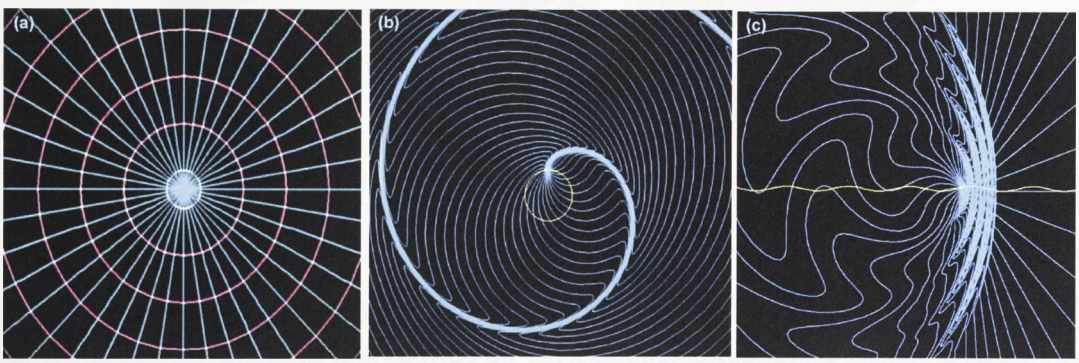

Fig. 3.3 – Snapshots of Radiation 2D simulator. (a) charged particle at rest; (b) charged particle in circular motion and (c) undulator trajectory. The blue lines correspond to the direction of propagation of $\vec{E}$. The red lines in panel (a) correspond to the regions where the electric field has the same magnitude. For panels (b) and (c) the velocity of the particles moving along the yellow line corresponds to $0.9c$.

The energy of the electromagnetic radiation produced by a charged particle moving through a magnetic field is given by[9]:

$$E_{rad} = \frac{hE^3}{2\pi \cdot r \cdot m^3 c^5} \tag{3.2}$$

where E is the energy of the moving particle, h is Plank's constant, r is the radius of curvature, m is the particle mass and c is the speed of light.

3.1.3 –Instrumentation for SR research

A schematic of a typical synchrotron facility is shown in Fig. 3.3, where (a) indicates the linear accelerator (linac), (b) the booster synchrotron, (c) the storage ring and (d) one of the beamlines.

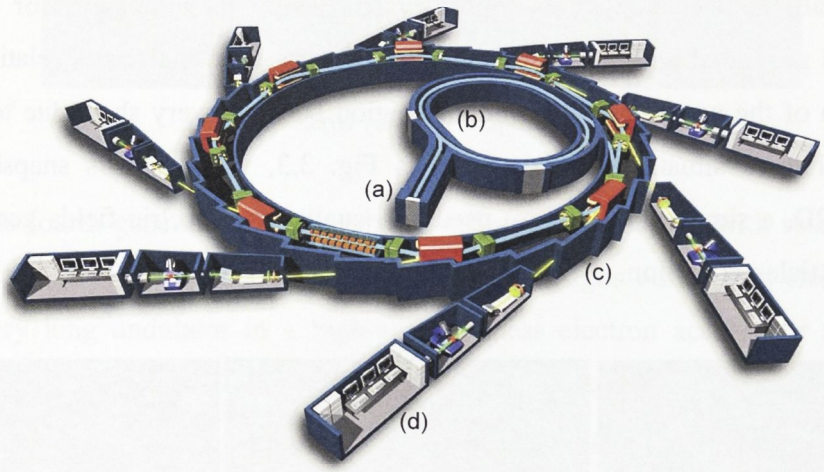

Fig. 3.4 – Schematic of a typical synchrotron facility. (a) Linear electron accelerator; (b) booster synchrotron; (c) storage ring; (d) beam line.

Electrons are first accelerated by the linac and transferred to the booster synchrotron, where their energy is increased. At Spring8, for instance, the energy of the electron beam is 1 GeV from the linac and 8 GeV upon leaving the booster synchrotron. Electrons are then transferred to a storage ring composed of a series of bending magnets and insertion devices, among other components, where the radiation produced by the electron beam can be directed to experimental stations (beam lines) around the ring.

Inside the storage ring, the electrons travel in bunches through vacuum vessels, with revolution times of a few μs. Quadrupole magnets focus the beam while bending magnets deflect the beam, thus producing a cone of electromagnetic radiation in the direction tangential to the electron trajectory. Insertion devices consist of periodic arrays of alternating north-south magnets, which change the trajectory of the electron bunch many times (wiggling or undulating the beam) thus increasing the amount of radiation produced, as well as other factors like confinement, brilliance and coherence. Wigglers produce a broad cone of light in each bend, which superimpose on each other

producing incoherent radiation of intensity proportional to the number of deflections. Undulators, on the other hand, produce much narrower cones of radiation that interfere with one another, given the electrons are only gently deflected from their trajectory. The constructive interference of certain wavelengths results in coherent radiation enhanced by up to 10,000 times. Specific wavelengths can be tuned by altering the gap between the magnets. Schematics of a bending magnet and an undulator are shown in Fig. 3.4. The energy lost by the electron beam, as it emits SR, is replenished by radio-frequency cavities positioned around the ring.

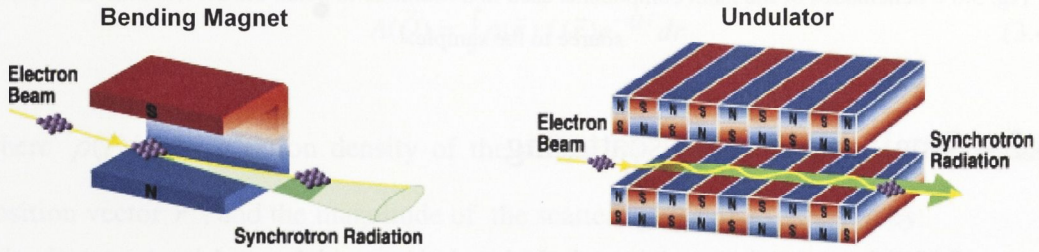

Fig. 3.5 – Schematic of bending magnet and undulator used as sources of synchrotron radiation.

In a synchrotron facility many beam lines can be operated simultaneously and independently, utilizing the radiation produced by the bending magnets and insertion devices. Typically, each beam line has a unique setup dedicated to a particular analytical technique. XAS and SAXS, for example, require a monochromatic and well-focused beam; hence, the polychromatic radiation passes through a series of apertures, monochromators and reflective mirrors before entering the experimental station. The schematic shown in Fig. 3.6 is an example of such beamline configuration, where slits, focusing mirrors and a double crystal monochromator are used to guide the SR from the source (bending magnet, wiggler or undulator) to the sample.

The storage ring and the beam lines are usually separated by a Be window, which protects the vacuum within the storage ring while transmitting almost all of the radiation. The slits define the size of the photon beam, which is collimated and/or focused by mirrors that can be flat, bent-flat or toroidal. The monochromator is typically a pair of Si crystals that, based on diffraction, select a particular wavelength band of radiation.

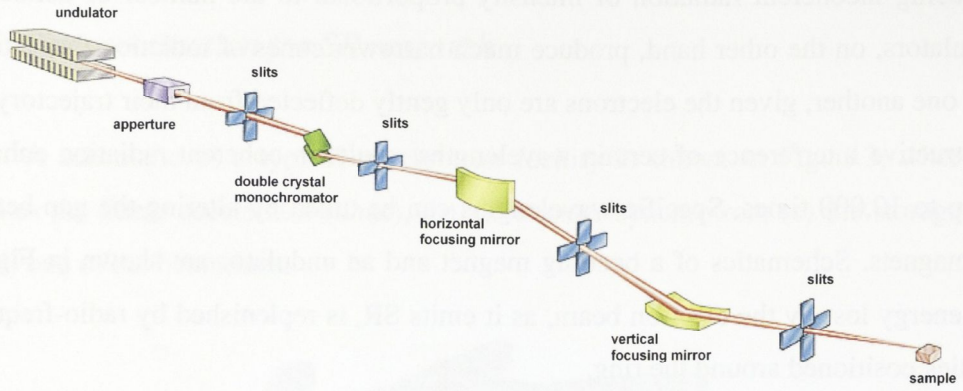

Fig. 3.6 – Schematics of the main components used in a beamline to guide the SR from the undulator source to the sample.

3.2 – Small-angle x-ray scattering

SAXS is a non-destructive analytical technique widely used in characterization of materials, probing inhomogeneities in the electronic density in the nm range from the elastic scattering of x-rays at angles close to 0^{o}. SAXS yields information on the mean size, shape, orientation and sometimes structure of domains (particles or voids), which can be solid, liquid or gaseous, surrounded by the same or another material in solid or liquid state. This section describes the basic principles of the SAXS technique and interpretation of the acquired data for NC analysis.

3.2.1 – Basic principles

The diffraction of x-rays by crystalline matter is such that the sin of angle of diffraction θ varies inversely with the separation of the diffracting lattice planes d:

$$j\lambda = 2d \sin\theta \tag{3.3}$$

where λ is the wavelength of the x-rays and j is an integer. When d is an interplanar lattice spacing, d and λ are usually of the same order of magnitude and as a consequence, the diffracted angles are rather large. For larger spacings, either the respective angles decrease considerably or longer wavelengths must be used. The latter,

however, is not always feasible as low energy photons are strongly absorbed by matter.[10] The solution relies on detecting the scattered x-rays far away from the sample, to enable the separation of the scattered signal from the direct beam and hence resolve scattering from small angles.

If a sample has a non-periodic structure or a sufficiently perturbed lattice, the diffraction patterns are not limited to spots or lines, but contain more or less extended regions of scattering. The diffraction pattern of a sample can be described in terms of reciprocal space, for which the amplitude of the scattering radiation $A(\vec{Q})$ is given by:[10]

$$A(\vec{Q}) = \int \rho(\vec{r}) f(\vec{r}) e^{-i\vec{Q}\cdot\vec{r}} dr \tag{3.4}$$

where $\rho(\vec{r})$ is the electron density of the diffracting body at a point defined by the position vector $\vec{r}$, and the magnitude of the scattering vector $\vec{Q}$ is given by:

$$Q = \frac{4\pi \sin\theta}{\lambda} \ . \tag{3.5}$$

The term $f(\vec{r})$ in Eq.(3.4) is a form factor that represents the system. For example, when considering a particle with dimensions from several tens to several hundred times the x-ray wavelength, $f(\vec{r})$ then equals the product of the electronic density and the volume of the particle.

In the special case of an isotropic system composed of isolated and identical particles embedded in a matrix with a constant electronic density, the normalized SAXS intensity $I(Q)$ is usually approximated by:

$$I(Q) = N\, I_1(Q)\, S(Q) \tag{3.6}$$

where N is the number of particles per unit volume and $I_1(Q)$ is the scattering function of a single isolated particle given by:

$$I_1(Q) = \int_0^\infty 4\pi r^2 \gamma(r) \frac{\sin Qr}{Qr} dr \tag{3.7}$$

where $\gamma(r)$ is the correlation function given by:

$$\gamma(r) = \int_V [\rho(\vec{r}') - \rho_0][\rho(\vec{r}'+\vec{r}) - \rho_0] d\vec{r}' \tag{3.8}$$

where $\rho(\vec{r})$ is the electronic density function inside the particle and ρ_0 is the constant electronic density of the matrix. Equation (3.8) represents an average of all particle orientations. The term $S(Q)$ in Eq. (3.6) accounts for the short range spatial correlation between the particles, the so called structure factor. If the system is dilute, i.e. the particles are well separated and without spatial correlation, $S(Q) = 1$ over the whole Q range and Eq. (3.6) simply becomes:

$$I(Q) = N\, I_1(Q) \tag{3.9}$$

For a system consisting of homogeneous particles with a constant electronic density ρ_1 immersed in an homogeneous matrix with a constant electronic density ρ_0, the scattering function for a single particle is given by:

$$I_1(Q) = (\rho_1 - \rho_0)^2 V \int_0^{D_{\max}} 4\pi r^2 \gamma_0(r) \frac{\sin Qr}{Qr} dr \tag{3.10}$$

where V is the particle volume with maximum dimension D_{max} and $\gamma_0(r)$ is a function defined by the orientation average of the intersection between the volume of the particle and the same volume displaced by a vector $\vec{r}$. The value of the integral only depends on the shape and size of the particle.

Equation (3.10) implies that $I_1(Q)$ is the same for particles or voids (of the same shape and size) embedded in a homogeneous matrix, provided the difference in electronic density between particle/void and the surrounding matrix is the same.

At small Q the function $I_1(Q)$ has an asymptotic behavior given by:

$$I_1(Q) = (\rho_1 - \rho_0)^2 V^2 e^{-\frac{R_g^2 Q^2}{3}} \tag{3.11}$$

where R_g is the radius of gyration of the particles defined by:

$$R_g = \left(\frac{1}{V} \int_V r^2 \, dV \right)^{\frac{1}{2}} \tag{3.12}$$

The scattering function corresponding to an isotropic dilute system of N identical particles (at small Q), known as the Guinier law, is given by Eq. (3.11) multiplied by N. It can also be applied to particles of identical shape with a size distribution, in which case R_g corresponds to an average of the radius of gyration (that weights much more large particles).

At high Q, the asymptotic behavior of $I(Q)$ is given by Porod's law:

$$I(Q) = \frac{2\pi(\rho_1 - \rho_0)^2 T}{Q^4} \tag{3.13}$$

where T is the surface area of the interface between the two phases. For spherical particles, for example, this function is characterized by a primary maximum at $Q = 0$ and secondary maxima that oscillate around a curve $I(Q) \propto Q^{-4}$. These oscillations are damped for spheres having a narrow size distribution and vanish for wider size distributions.

For a system of non-spherical particles, the scattering intensity $I(Q)$ can be approximated by:

$$I(Q) = n^2 N e^{-Q^2 D^2(l_0)} \tag{3.14}$$

where n is the number of electrons per particle and $D(l_0)$ is the diameter of the particle in the direction defined by $\vec{l}_0$ (a full description of the basis of Eq. (3.14) can be found in ref.[10]). The scattering from a single particle is projected in a plane of observation as shown in Fig. 3.7.

The scattered intensity of an ensemble of widely separated particles is identical (on a relative scale) to the mean intensity scattered by one isolated particle.[10] When considering an ensemble of particles, the resulting scattering image is a superposition of

the scattering intensities from each individual particle. If the particles have a similar shape and orientation, the scattering image yields qualitative information about the shape of the particles, as for the example shown in Fig. 3.7, where the image is compressed in the direction parallel to the major dimension of the particle. On the other hand, if the particles are randomly oriented, the scattering from each individual particle is also randomly oriented, and the resulting scattering is isotropically distributed around the beam stop, hence information about the shape of the particles cannot be retrieved.

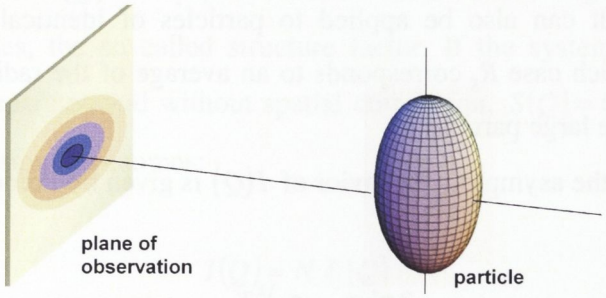

Fig. 3.7 – Relationship between the orientation of a particle and the distribution of scattered intensity in the plane of observation.

3.2.2 – Experimental setup

SAXS measurements were performed at the ChemMatCARS beamline 15ID-D, Advanced Photon Source, USA, with a setup similar to that shown in Fig. 3.8.

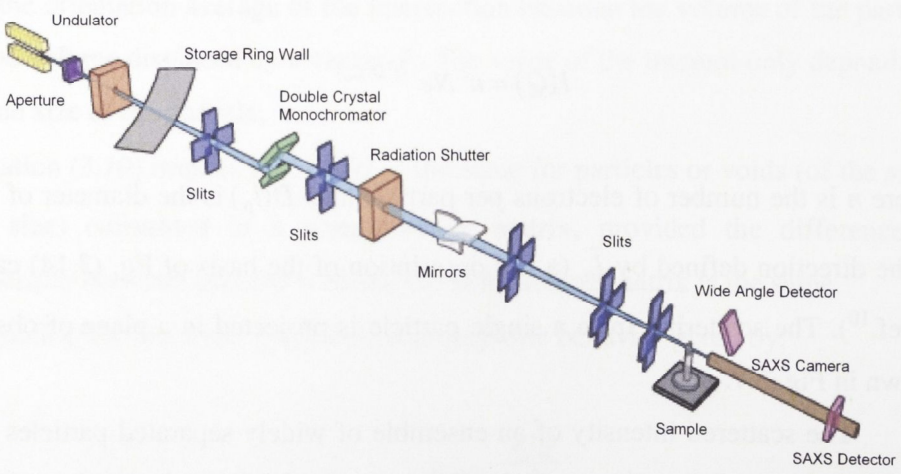

Fig. 3.8 – Schematic of SAXS beamline.

The scattered intensity I was collected as a function of the scattering vector Q using a MAR-165 charge coupled device (CCD) detector with exposure times of 1 – 5 s using x-rays of wavelength 1.11 Å. The measurements were performed in transmission mode with the sample surface normal oriented at angles of 0 – 45° relative to the photon beam, as shown in the schematic of Fig. 3.9 (not to scale).

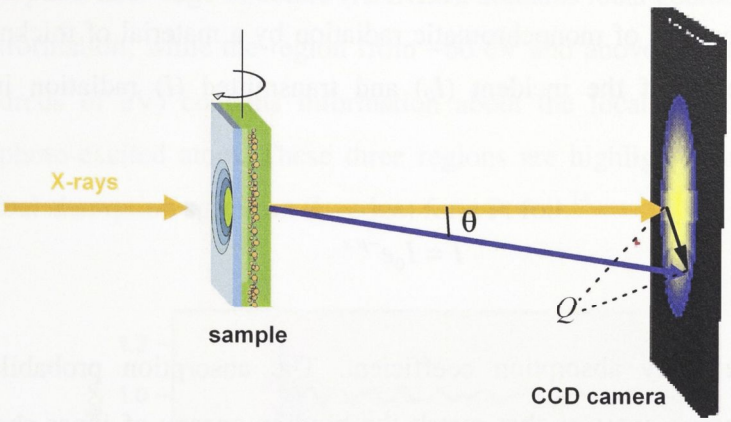

Fig. 3.9 – Sample orientation setup used in transmission SAXS measurements (distances and sizes not to scale).

Camera lengths (distance between the sample and the detector) can be adjusted according to the dimension range of the domains being measured. Larger particles scatter at lower angles, thus requiring longer camera lengths. The results presented in chapters V and VI were obtained using camera lengths of 550, 1880 and 6880 mm. The sample preparation method and data analysis are described in chapter IV. A detailed description of the beamline 15ID-D at the Adavanced Photon Source can be found in Ref..[11]

3.3 – X-ray absorption fine structure

X-ray absorption fine structure (XAFS) is a technique that uses x-rays to probe the physical and chemical structure of matter at an atomic scale. Usually, photon energies lower than 100 keV are used to probe atomic numbers higher than 20, hence the interaction between radiation and matter primarily occurs via the photoelectric effect (given Compton scattering and pair production are negligible at such energies).[12]

When x-rays are incident in solid or liquid matter, the photons may transfer their energy to bound electrons, with a probability that depends on both the initial and final states of the electron.[13] The initial state is the localized unperturbed core level corresponding to the absorption of the x-ray. The final state is that of the ejected photoelectron produced and subsequently scattered, which can initially be represented as an outgoing spherical wave emanating from the absorbing atom.

The absorption of monochromatic radiation by a material of thickness x can be expressed in terms of the incident (I_0) and transmitted (I) radiation intensities as follows:

$$I = I_0 e^{-\mu x} \tag{3.15}$$

where μ is the x-ray absorption coefficient. The absorption probability abruptly increases for photon energies that match the binding energy of inner shell electrons, yielding what is known as an absorption edge. Figure 3.10 schematically shows the absorption of x-rays by electrons in the K (Fig. 3.10(a)) and L (Fig. 3.10(b)) shells of an atom. For Pt atoms, absorption by electrons in the K shell necessitate x-ray energies > 78 keV, while electrons in the L shells can absorb x-rays with energies > 11.5 keV (L_1, L_2 and L_3). The L_3 ($2p_{3/2}$) level has the highest probability and lowest energy for absorption (among the L transitions). The main graph in Fig. 3.10 shows the absorption coefficient as a function of the incident photon energy for Pt, with the K and L edges apparent.

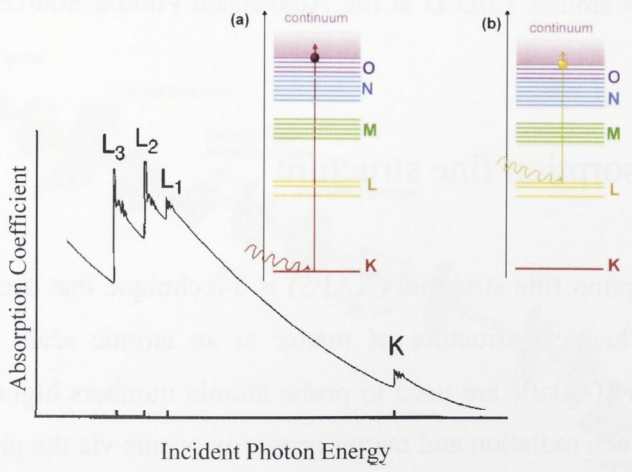

Fig. 3.10 – Schematic representation of x-ray absorption by electrons in the (a) K and (b) L shells of an atom. The main graph shows the absorption coefficient as a function of the incident photon energy for Pt.

The absorption spectrum is composed of three distinct regions. The pre-edge region is before the absorption edge and can contain electron excitations to unoccupied bound states below the vacuum level. Close to and above the edge, XAFS probes both bound and continuum states, resulting in pronounced peaks superimposed on a smooth isolated atom contribution. The region that extends to ~60 eV beyond the edge, known as x-ray absorption near edge structure (XANES), contains local geometrical as well as electronic information, while the region from ~60 eV and above (usually extending to several hundreds of eV) contains information about the local geometrical structure around the photo-excited atom. These three regions are highlighted in Fig. 3.11 that shows a typical absorption spectrum (L_3 edge) for a Pt foil.[14]

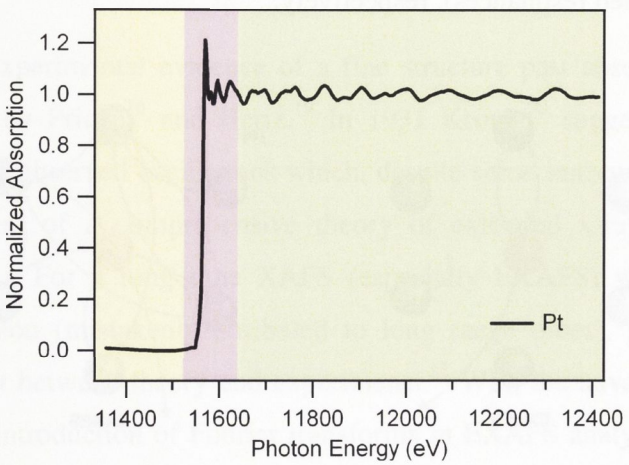

Fig. 3.11 – X-ray absorption spectrum as a function of the photon energy for bulk Pt. The pre-edge, near-edge and extended regions are highlighted in yellow, pink and green, respectively.

3.3.1 - XANES region

The near-edge structure in an absorption spectrum encompasses all the unoccupied states from the Fermi level up to the EXAFS limit. In a transition metal, for example, the XANES includes the unoccupied part of the narrow *d* bands, just above the Fermi level, as well as the less tightly bound *s* and *p* bands.[15] A theoretical analysis of XANES involves solving the Schrödinger equation for a range of photoelectron energies at the lower end of which the interaction of the electrons with the atoms is very strong. Such an approach can be found in Refs.[14-16]

The scattering of photoelectrons depends strongly on their energy. At high energies (EXAFS), photoelectron scattering is weak such that the most significant contribution to the final state wave function in the vicinity of the absorbing atom comes from paths in which the electron is scattered only once (single scattering). In the XANES regime, the photoelectron has enough energy to reach the continuum and has a wavelength larger than the interatomic distance between the central atom and first neighbor. At such low kinetic energy the photoelectron is strongly scattered by neighboring atoms and its wave function is mainly determined by multiple scattering effects inside a cluster formed by the first coordination shell and eventually the second and third shells.[17] Figure 3.12 shows a schematic representation of single (Fig. 3.12(a)) and multiple (Fig. 3.12(b)) scattering determining the EXAFS and XANES oscillations (the latter also called resonances), respectively.

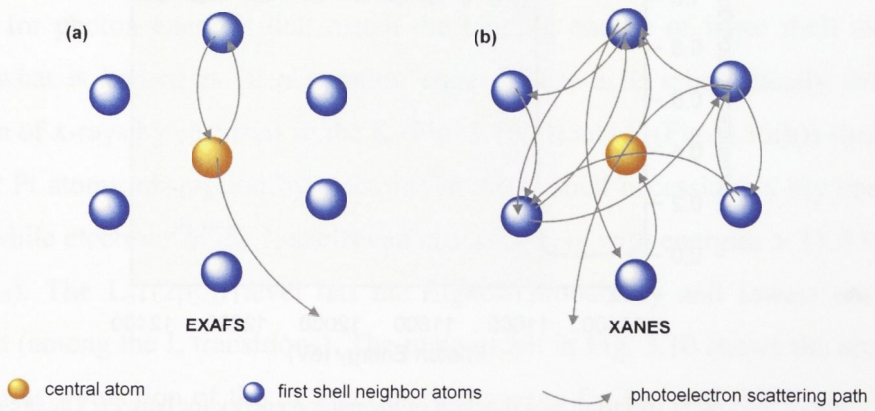

Fig. 3.12 – Schematic representation of a photoelectron (a) single scattering and (b) multiple scattering.

Because EXAFS is dominated by single scattering, the information contained therein is purely geometrical. In the XANES regime, however, multiple scattering effects confer sensitivity to details of the spatial arrangement of atoms surrounding the absorber, not only radial distance but also bond angles, electronic configuration and so on. Furthermore, changes in the charge distribution around a given atom in different chemical environments can alter core-level binding energies and thus shift the absorption edge.[15]

Information such as the average oxidation/hydrogenation state can be extracted from XANES spectra by examining edge energy shifts and the position and intensity of the continuum resonances, which can be calculated theoretically or relative to well

known references. Calibration of the energy scale and normalization of the absorbance are mandatory. One of the most satisfactory means is the measurement of a reference simultaneously with the sample. Analytical methods include fitting the sample spectrum with a linear combination of reference spectra (often used to estimate the fraction of O bonding in a certain material, given the availability of a reference sample whose oxide fraction is well known) and the subtraction of the sample and a reference spectrum. The latter pursues, for example, the isolation of the electronic effects induced in metals by sorption and has been widely used to study the effects of H adsorption/chemisorption in Pt.[14]

3.3.2 - EXAFS region

The first experimental evidence of a fine structure past absorption edges was reported in 1920 by Fricke[18] and Hertz.[19] In 1931 Kronig[20] suggested a theoretical explanation for the observed oscillations which, despite some inaccuracies, contributed in the development of a comprehensive theory of extended x-ray absorption fine structure (EXAFS). For a long time XAFS (especially EXAFS) was considered an obscure phenomenon (mistakenly attributed to long range order), given the lack of detailed agreement between theory and experiments.[15] With the advent of synchrotron radiation and the introduction of Fourier transforms in EXAFS analysis, the technique became experimentally accessible to the general scientific community, finding wide applicability in many areas.

Figure 3.13 shows a schematic representation of the outgoing and backscattered photoelectron waves. The backscattered waves interfere constructively or destructively with the outgoing wave depending on their relative phase. The total amplitude of the electron wave function is thus enhanced or reduced, modifying the probability of x-ray absorption. The maxima in the EXAFS region of Fig. 3.11 correspond to the backscattered wave being in phase with the outgoing component while the minima result when the two are out of phase.

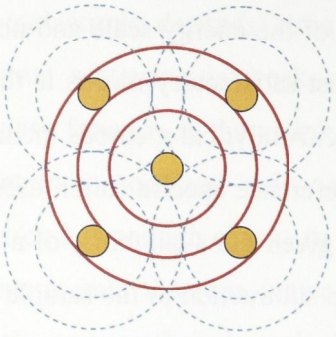

Fig. 3.13 – Schematics of the radial portion of the photoelectron wave. The solid red lines indicate the outgoing waves and the dashed blue lines represent scattering from the surrounding atoms.

The EXAFS function χ is defined as the normalized, oscillatory part of the x-ray absorption above a given absorption edge:

$$\chi(E) = \frac{\mu(E) - \mu_0(E)}{\Delta\mu_0} \tag{3.16}$$

where $\mu(E)$ is the x-ray absorption coefficient (Eq.(3.15)), $\mu_0(E)$ is the smoothly varying atomic-like background absorption and $\Delta\mu_0$ is a normalization factor that arises from the net increase in the total atomic background absorption at the edge in question.[21] Conventionally, χ is defined with respect to the photoelectron wavenumber $k = \frac{\sqrt{2m(E_{ph} - E_c)}}{\hbar}$, where E_{ph} is the energy of the photoelectron and E_c is the threshold energy for photoexcitation (see Fig. 3.10). A quantitative parametrization of EXAFS can be obtained through the following equation:

$$\chi(k) = \sum_R S_0^2 \cdot CN \cdot \frac{|f(k)|}{kR^2} \sin(2kR + 2\delta_c + \Phi) e^{-2R/\lambda(k)} e^{-2\sigma^2 k^2} \tag{3.17}$$

The amplitude factor S_0^2 is a many-body effect due to the relaxation of the system in response to the creation of the core hole. As it is weakly energy dependent, it is usually approximated by a constant.

The backscattering amplitude is given by:

$$f(k) = |f(k)| e^{i\Phi(k)} \tag{3.19}$$

δ_c is the central-atom partial-wave phase shift of the final state and $\lambda(k)$ is the energy-dependent mean-free-path of the photoelectron (~6 – 8 Å). The phase factor Φ reflects the quantum-mechanical wavelike nature of the backscattering. A somewhat larger contribution to the overall phase is given by the phase shift δ_c at the absorbing atom, since the photoelectron sees the potential created by this atom twice. These phase shifts account for the difference between the measured and geometrical interatomic distances, which is typically a few tenths of an Å and must be corrected by either a theoretical or experimental reference standard.

The dependence of the oscillatory structure on interatomic distance and energy is clearly reflected by the $\sin(2kR)$ term. The decay of the $\chi(k)$ due to the mean-free-path or finite lifetime of the photoelectron is represented by the exponential term $e^{-2R/\lambda}$. This factor is largely responsible for the relatively short range (generally a few Å) around the absorbing atom probed by an EXAFS experiment. The strength of the scattered interfering wave depends on the type and number of neighboring atoms through the backscattering amplitude $|f(k)|$ and hence is primarily responsible for the magnitude of the EXAFS signal. Parameters like the spherical-wave factor $1/kR^2$ and the mean-free-path term are secondary but important for a quantitative analysis of the EXAFS amplitude.

The Debye-Waller factor, given to a good approximation by $e^{-2\sigma^2 k^2}$, is due in part to thermal effects ($\sigma^2_{thermal}$), or the motion of atoms about their equilibrium position. Such atomic motion smears the sharp interference pattern of the rapidly varying $\sin(2kR)$ term that would be apparent if the atoms were static. The Debye-Waller factor becomes more pronounced greater the photoelectron wavenumber, and hence damps the EXAFS beyond about $k \approx 1/\sigma$, which is typically about 10 Å^{-1}. Therefore the Debye-Waller factor is essential in EXAFS, but is negligible in XANES.

The structural parameters are the interatomic distance *R*, the coordination number *CN*, and the mean-square relative displacement (MSRD) of the distribution of interatomic distances σ^2. The latter includes effects due to structural and thermal disorder:

$$\sigma^2 = \sigma^2_{thermal} + \sigma^2_{static} \tag{3.18}$$

For systems weakly disordered, the distribution of interatomic distance can be approximated by a Gaussian, with width σ^2. To account for anharmonicities in the radial distribution function, particularly for disordered systems, one can define the XAFS in terms of the cumulant moments of the distribution (or cumulants), where the Debye-Waller factor is generally complex and has a natural cumulant expansion in powers of k in the form:

$$\left\langle e^{i2k(r-R)} \right\rangle = \exp \sum_{n=0}^{\infty} \frac{(2ik)^n}{n!} C_n \tag{3.19}$$

where C_n denotes the nth cumulant average. The leading cumulants are given by:

$$\begin{aligned} C_1 &= \langle (r-R) \rangle \\ C_2 &= \left\langle (r-R)^2 \right\rangle \equiv \sigma^2(T) \\ C_3 &= \left\langle (r-R)^3 \right\rangle \\ C_4 &= \left\langle (r-R)^4 \right\rangle - 3(C_2)^2 \end{aligned} \tag{3.20}$$

The amplitude of the Debye-Waller factor contains only even moments, whereas odd moments contribute to the XAFS phase. The k_3 is particularly important for large disordered systems. If not corrected for, the term with the third cumulant gives rise to an apparent contraction of distances extracted from XAFS with increasing temperature.[21]

3.3.3 – Experimental setup

EXAFS and XANES measurements were performed at beamline 20-B of the Photon Factory, Japan, at the Pt L_3 edge (11,564 eV). Figure 3.14 shows a schematic of a typical experimental setup, where the fluorescence detector is positioned at 90° with respect to the beam direction and the sample normal is rotated at 45° with respect to the

incident beam. Given the majority of the samples studied were inhomogeneous and diluted, the measurements were all performed in fluorescence mode[†], and a reference Pt foil was measured simultaneously (for energy calibration) in transmission mode in the last ionization chamber (transmission detector 2).

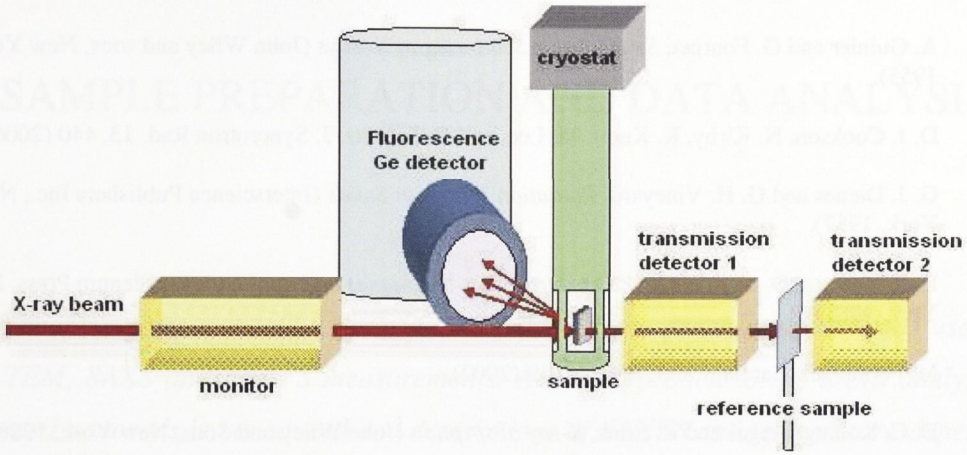

Fig. 3.14 – XAS experimental setup.

A temperature controller and He cryostat were used to maintain the sample temperature with an accuracy of ±1 K. The sample temperature was maintained at 12 ± 1 K to minimize thermal vibration except for temperature-dependent studies, when measurements were performed in the range from 20 to 295 K. Data were collected using a 6 x 6 pixel array Ge detector and the Si (111) monochromator was detuned by 50% for harmonic rejection.

References

1 H. Winick and S. Doniach, *Synchrotron radiation research* (Plenum Press, New York, 1980).

2 J. C. Maxwell, *A Treatise on Electricity and Magnetism* (Claredon Press, Oxford, 1873).

3 A. Lienard, L'Eclairage Elect. **16**, 5 (1898).

4 F. R. Elder, A. M. Gurewitsch, R. V. Langmuir, and H. C. Pollock, Journal of Applied Physics **18**, 810 (1947).

[†] Dilute inhomogeneous samples are best investigated by means of the fluorescent x-rays originating from the de-excitation of the atoms after the photoelectron is generated (also know as fluorescence measurements). Transmission measurements require homogeneous samples sufficiently thick to absorb ~50% of the incident x-rays.

[5] F. R. Elder, R. V. Langmuir, and H. C. Pollock, Physical Review **74**, 52 (1948).

[6] J. P. Blewett, J. Synchrotron Rad. **5**, 135 (1998).

[7] http://www.shintakelab.com/en/enEducationalSoft.htm.

[8] T. Shintake, Nucl. Instrum. Meth. A **507**, 89 (2003).

[9] I. H. Munro and G. V. Marr, *Handbook on Synchrotron Radiation* (North-Holland, Amsterdam, 1987).

[10] A. Guinier and G. Fournet, *Small-Angle Scattering of X-Rays* (John Wiley and sons, New York, 1955).

[11] D. J. Cookson, N. Kirby, R. Knott, M. Lee, and D. Schultz, J. Syncrotron Rad. **13**, 440 (2006).

[12] G. J. Dienes and G. H. Vineyard, *Radiation Effects in Solids* (Interscience Publishers Inc., New York, 1957).

[13] B. K. Teo and D. C. Joy, *EXAFS spectroscopy, techniques and applications* (Plenum Press, New York, 1981).

[14] M. Fernandez-Garcia, Catal. Rev. **44**, 59 (2002).

[15] D. C. Koningsberger and R. Prins, *X-ray absorption* (John Wiley and Sons, New York, 1988).

[16] J. Stöhr, *NEXAFS spectroscopy* (Springer-Verlag, Berlin, 1996).

[17] A. Bianconi, Appl. Surf. Sci **6**, 392 (1980).

[18] H. Fricke, Phys. Rev. **16**, 202 (1920).

[19] G. Hertz, Z. Phys. **3**, 19 (1920).

[20] R. d. L. Kronig, Z. Phys. **70**, 317 (1931).

[21] J. J. Rehr and R. C. Albers, Rev. Mod. Phys. **72**, 621 (2000).

CHAPTER IV

SAMPLE PREPARATION AND DATA ANALYSIS

This chapter gives a detailed description of the sample preparation methods used for the TEM, SAXS and EXAFS measurements. A new approach to the SAXS analysis of oriented nanorods is introduced and descriptions of XANES and temperature-dependent EXAFS analysis of embedded Pt NCs are given.

4.1 – TEM sample preparation method

Transmission electron microscopy (TEM) is a versatile technique widely used in NC characterization for the direct observation of parameters like shape, size and distribution of NCs embedded or supported in a variety of matrices. Crystallographic information can also be obtained through micro-diffraction, yielding insights into NC structure. The samples must be carefully prepared to produce a region transparent to the electron beam (approximately a few hundred nm thickness for a-SiO_2).

For the present work, samples were prepared using the small-angle cleavage technique,[1-3] which consists of the cleaving of selected planes of the Si substrate resulting in tips sufficiently thin to be transparent to the electron beam in cross-section. The sample consisting of 2 μm a-SiO_2 film (containing Pt NCs) on ~500 μm Si substrate was first back-thinned to ~100 μm by mechanical polishing as shown in Fig. 4.1(a) and (b). Subsequently, the Si substrate was scribed along the (120) plane, corresponding to an angle of ~71.5° as shown in Fig. 4.1(c). The sample was then cleaved along the (120) plane, followed by another cleave in the (110) direction, resulting in a wedge with a fine tip as shown in Fig. 4.1(d). The process was repeated and several wedges were attached to a copper ring using epoxy mixed with silver powder to improve electrical conductivity, as shown in Fig. 4.1(e).

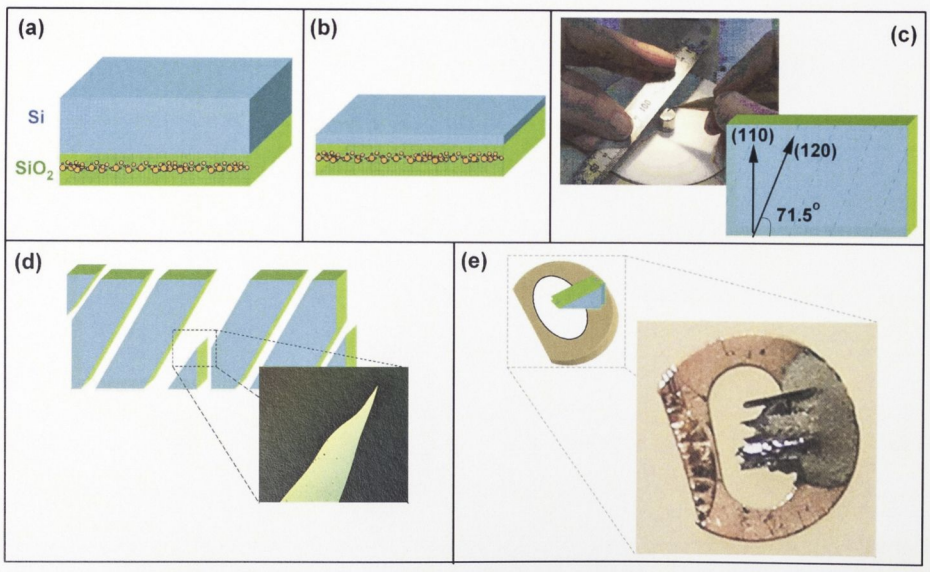

Fig. 4.1 – Schematic of small-angle cleavage technique for TEM sample preparation.

Figure 4.2 shows TEM images of a sample prepared using this method. The main panel shows the cross-sectional image of the NC containing SiO_2 layer, the small panels shows magnified views of selected areas across the sample edge.

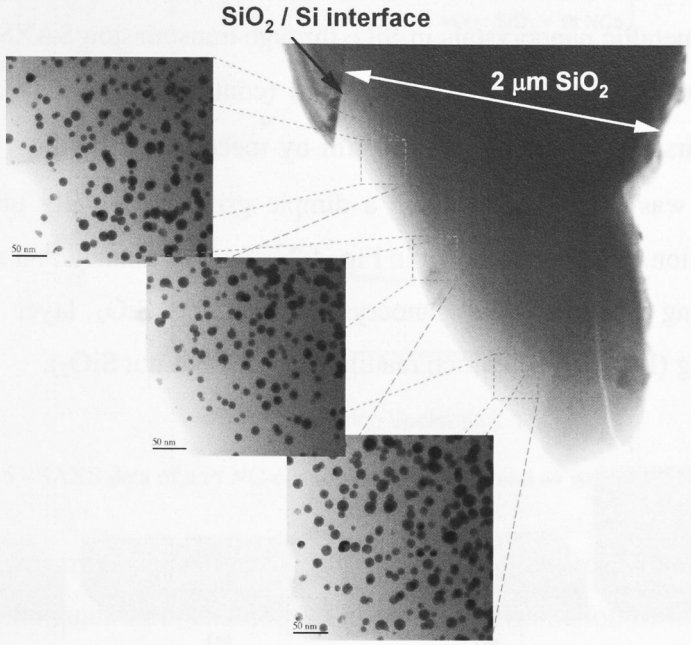

Fig. 4.2 – TEM micrographs of a sample prepared using the small-angle cleavage technique. The main figure shows a cross-sectional image of the NC containing SiO_2 layer with the SiO_2/Si interface visible on the left and the SiO_2 surface visible on the right. The small panels show magnified views of the NCs across the sample.

The benefits of using the small-angle cleavage technique include significantly less time spent in sample preparation, absence of artifacts caused by sample heating or ion milling and, most importantly, a uniform thickness across the entire SiO_2 layer (from surface to interface), which significantly improves the image quality and the analysis of NC depth distribution.

4.2 – SAXS sample preparation method

Small-angle x-ray scattering (SAXS), as described in the previous chapter, is widely used to determine the size distribution of NCs formed within a variety of matrices including SiO_2 (for examples see Refs.[4-7]). This oxide is typically grown on a Si substrate for compatibility with electronic and photonic device fabrication and SAXS measurements are thus commonly performed in a grazing-incidence geometry.[8-10]

Transmission measurements are also possible with the appropriate photon energy and flux to penetrate the thick Si substrate though scattering from the latter can degrade image quality.

We have developed a novel sample preparation method for determining the size distribution of metallic nanocrystals in SiO_2 through transmission SAXS measurements. The sample consisting of a 2 μm a-SiO_2 film (containing Pt NCs) on ~500 μm Si substrate was first back-thinned to ~150 μm by mechanical grinding. A concavity of 130 μm depth was then formed using a dimple grinder normally utilized for TEM sample preparation. Finally, as shown in Fig. 4.3, a hole of diameter ~1 mm was opened in the remaining Si below the nanocrystal-containing SiO_2 layer using selective chemical etching (KOH/H_2O) (which readily etches Si but not SiO_2).

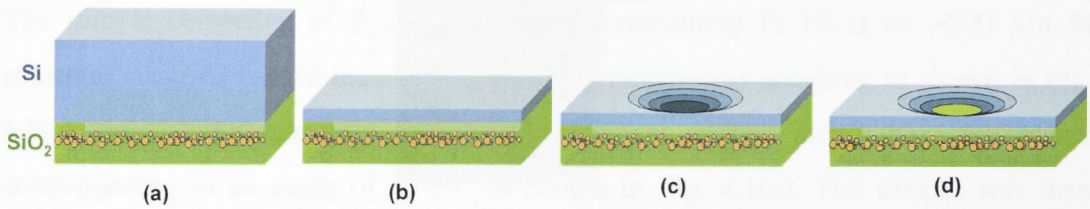

Fig. 4.3 - Schematic of SAXS sample preparation method: (a) sample containing Pt NCs, (b) part of Si substrate removed, (c) a concavity produced in the remaining Si substrate, (d) hole opened in the Si substrate by chemical etching.

Figure 4.4 shows an optical image of a sample prepared with this method, with a magnified view of the SiO_2 layer with both transmitted and reflected illumination.

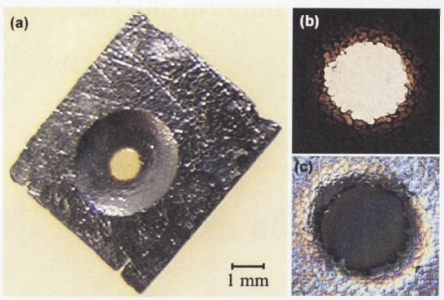

Fig. 4.4 – (a) Optical micrograph of SAXS sample with the SiO_2 membrane visible in the center. (b) Magnified views of the hole in both transmission and (c) reflection modes.

Using this method, we were able to prepare self-supported thin-film samples ideal for transmission SAXS measurements. As an example, Fig. 4.5 shows the SAXS

intensity $I(Q)$ as a function of the scattering vector Q for an isolated SiO_2 layer and a Pt NC-containing sample.

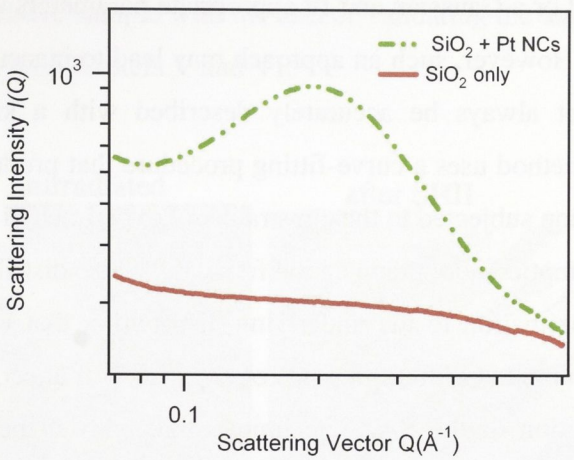

Fig. 4.5 - SAXS data of a Pt NC-containing SiO_2 layer and an isolated SiO_2 layer.

As apparent from Fig. 4.5, the scattering contribution from the SiO_2 layer can be easily isolated and quantified, enabling an absolute determination of the Pt nanocrystal size distribution. Precision alignment for grazing-incidence geometry is no longer required and scattering and diffraction from the underlying Si substrate are eliminated. Furthermore, given our ability to form nanocrystals with oriented, non-spherical shapes (such as ellipsoids with the major axis aligned along the ion-beam direction), this sample preparation method also enables incident-angle-dependent SAXS measurements to better extract both the nanocrystal size and shape distributions.

4.3 – Angle-dependent SAXS analysis

The well-established models used in the analysis of spherical particles[11] in addition to readily available fitting procedures like the maximum entropy method[12] make SAXS a powerful tool in the analysis of spherical NCs embedded in a matrix. Analysis of non-spherical particles, however, usually requires complex modeling[13-15] that depends on the shape and orientation of the particles. An additional complication arises in the case of randomly oriented but otherwise identical non-spherical particles. In such case the scattering is azimuthally isotropic but can be mistaken for a broad size distribution of spherical NCs.[11]

The size distribution of inhomogeneities (in this case Pt NCs) can be approximated by fitting appropriate distribution parameters to the measured SAXS intensity data. One such method is to assume some functional form for the distribution such as a log-normal or a Gaussian and fit appropriate parameters using nonlinear least-squares refinement. However, such an approach may lead to inaccuracies given the size distribution may not always be accurately described with a known function. The maximum entropy method uses a curve-fitting procedure that produces structures in the probability distribution subjected to the constraints of experimental observations. It does not require any assumption about the general form of the size distribution, producing the most uniform approximation to the underlying distribution that is consistent with the experimental intensity data (within the limits of experimental uncertainty).[12, 16]

It is a limitation of the SAXS technique that both shape and size cannot be determined independently, thus requiring the use of a form factor that constraints the shape of the particles, where the latter can be determined by auxiliary methods, like TEM.[17] A common assumption about the morphology is that all the scatterers have the same shape, or in the case of cylindrically shaped scatterers, for example, the ratio between the cylinder length and diameter might be assumed to remain constant. For the analysis of unirradiated Pt NCs, the shape of the scatterers was considered spherical, as determined by TEM and the SAXS data analyses were performed using the maximum entropy method.[12, 16, 18] In the case of elongated Pt NCs (after SHII), TEM analysis shows that neither the dimensions, the volume or the aspect ratio of the particles could be considered the same without significant loss of accuracy. In this case, information about the NC volume or aspect ratio would still be required to yield a unique solution even if an appropriate form factor (to account for the rod-like shape of the NCs) was employed.

Given the non-spherical NCs are highly aligned, we demonstrate the possibility of determining the major (D_{major}) and minor (D_{minor}) dimensions of rod-shaped NCs by the separate analysis of selected angular sectors of the scattering pattern (detector image). A few corrections to the spherical model are required to recover the total volume of scattering centers. The dimensions of the major and minor axes of the NCs, however, are in excellent agreement with TEM results (shown in chapter VI).

Figure 4.6 shows representative TEM micrographs of Pt NCs before and after SHII. Prior to irradiation the particles are spherical, with mean diameter ~14.5 nm, as

determined by TEM and SAXS measurements. The irradiation of the NCs with $2x10^{14}$ cm^{-2} Au ions at 185 MeV induces a significant change in the NCs shape, elongating the particles in the direction of the ion beam. The present section compares TEM and SAXS results of a representative sample with the aim of validating the analysis procedure. For the complete results, see Chapters V and VI.

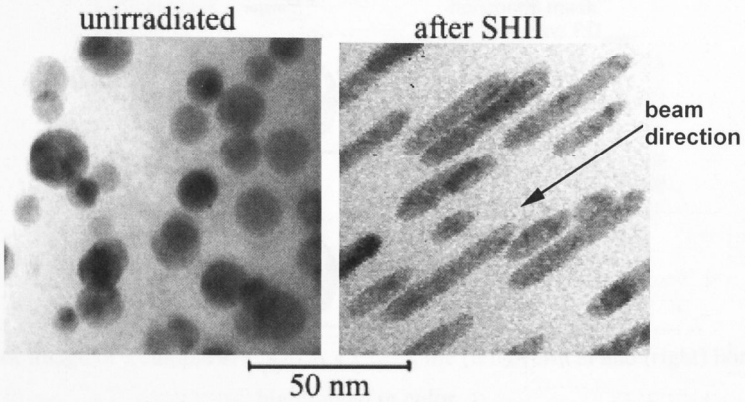

Fig. 4.6 - (left) TEM micrographs of unirradiated sample containing Pt NCs and (right) a sample irradiated with 185 MeV Au ions to a total fluence of $2x10^{14}$ cm^{-2}.

Figure 4.7 shows SAXS detector images for the rod-like NCs shown in Fig. 4.6, with the sample normal oriented at different angles relative to the x-ray beam. The projected dimensions of a rod-like NC (for each measurement angle) are schematically shown in the right column.

Figure 4.6 shows the elongated particles are highly oriented in one direction (perpendicular to the SiO_2 surface). This causes the x-rays to scatter isotropically around the beam stop when the sample is measured at 0^o (D_{major} of the particles is oriented parallel to the x-ray beam and the projected D_{major} = D_{minor}). Based on the geometry of ellipsoids of revolution, the projected D_{major} (PD_{major}) of elongated particles is given by:

$$PD_{major} = \sqrt{D_{major}^2 \sin^2 \beta + D_{minor}^2 \cos^2 \beta}\,. \tag{4.1}$$

where β is the angle of orientation.

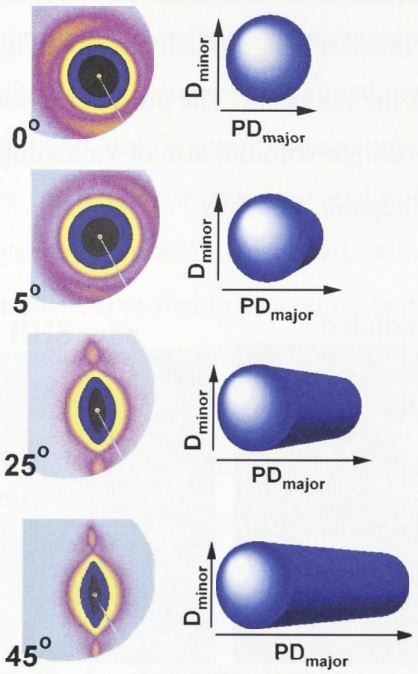

Fig. 4.7 - (left) Experimentally obtained SAXS detector images and (right) schematic of elongated particles at different angles of rotation.

The anisotropy observed in the detector images for samples oriented at 25° and 45° are due to differences between the D_{minor} and the PD_{major} of the elongated NCs. In this particular case of oriented NCs, the scattering contribution from the minor axis remains unaltered even after sample rotation, while the projection from the major axis result in scattering at smaller angles, thus appearing to compress the detector image in one direction. For this reason, selected angular sectors of the detector image were integrated and analyzed separately to enable the individual evaluation of both D_{minor} and PD_{major} of the rod-shaped NCs. Arc sector areas (masks) of 10° (with origin at the beam stop), shown in Fig. 4.8, were chosen to avoid non-isotropic intensity within the selected areas without compromising the statistics of the integrated signals.

Figure 4.9 shows the scattering intensity as a function of the scattering vector Q for selected area masks representing the D_{minor} and the PD_{major} of the elongated particles. Panel (a) shows the comparison between the vertical masks for samples oriented at 0° and 45° as well as the whole detector image of a sample at 0°. The results shown in Fig. 4.9(a) are basically the same for the three examples, which demonstrates that the use of masks do not significantly affect the quality of the scattering intensity, despite the reduced integrated area (of the detector). The scattering contribution due to D_{minor} is not

affected by the rotation of the sample if a vertical mask is used. Fig. 4.9(b) shows the scattering contribution corresponding to horizontal masks applied to a sample oriented at different angles. The scattering contribution from the PD_{major} becomes significantly different than the one from D_{minor} for angles > 20°, becoming more like that characteristic of particles with broader size distributions.

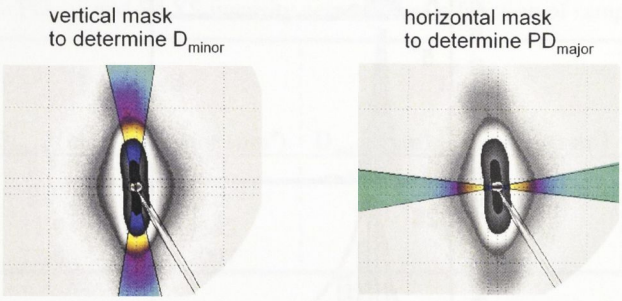

Fig. 4.8 – Detector image of a sample oriented at 45° with the (left) vertical and (right) horizontal masks highlighted in color.

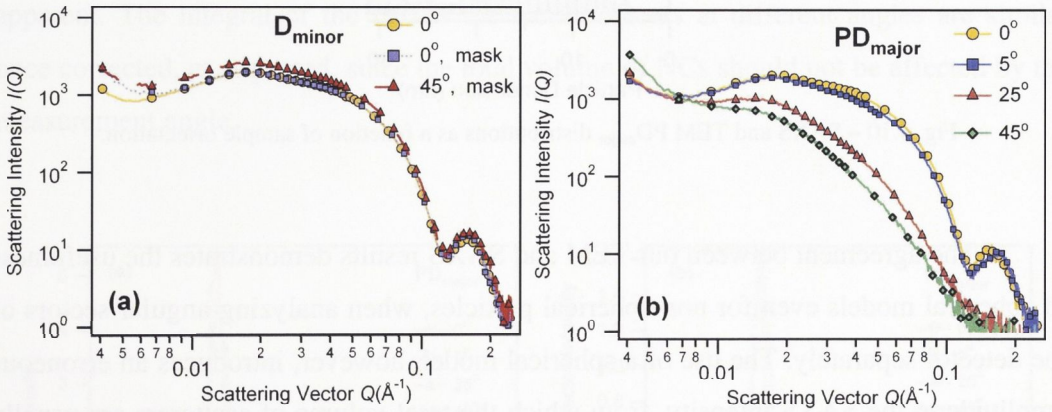

Fig. 4.9 – SAXS scattering intensity as a function of the scattering vector $Q(Å^{-1})$ from selected area masks: (a) comparison between the integral of the whole detector and the 10 ° vertical mask for a sample oriented at 0° and 45°; (b) 10° horizontal mask applied to the sample at different angles of rotation.

Despite the non-spherical nature of the NCs, the D_{minor} and PD_{major} distributions were separately estimated with the maximum entropy method[12] assuming spherical particles. This was only possible because of the high degree of orientation of the particles and the separate integration and analysis of selected areas of the detector. Fig. 4.10 shows the PD_{major} distributions for samples oriented at different angles, whose scattering intensity as a function of Q are shown in Fig. 4.9(b). Both SAXS and TEM

results are shown. For the latter, D_{minor} and D_{major} were manually measured from TEM micrographs and, subsequently, the PD_{major} was calculated using Eq. (4.1).

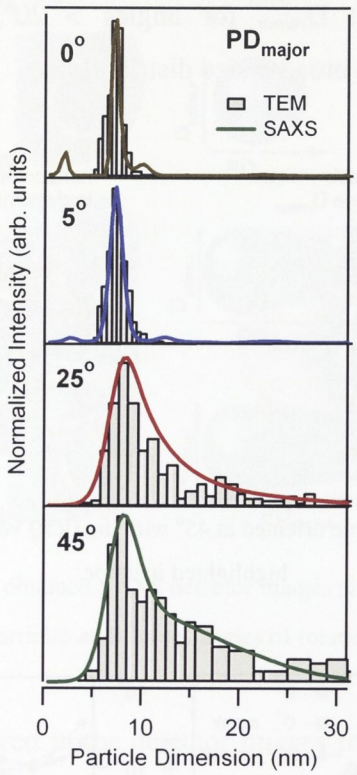

Fig. 4.10 – SAXS and TEM PD_{major} distributions as a function of sample orientation.

The agreement between our TEM and SAXS results demonstrates the usefulness of spherical models even for non-spherical particles, when analyzing angular sectors of the detector separately. The use of a spherical model, however, introduces an erroneous amplitude to the SAXS intensity, from which the total volume of scatterers are usually determined. This is due to a difference in the real volume of the particles and that of the theoretical spheres used by the fitting procedure. Fortunately, this can be corrected after the fit is completed. We relate the real volume of the particles and the spherical or projected volume evaluated by the program using Eq. (4.2), bearing in mind that the number of electrons in a particle is proportional to the volume of the particle and using Eq. (3.6):

$$V_{real}^2 N_{real} = V_S^2 N_S \tag{4.2}$$

where V_{real} and N_{real} are the real volume occupied by the particles and the real number of particles, respectively, and V_S and N_S represent the spherical volume estimated by the fitting procedure and the respective number of particles. Table 1 presents the PD_{major} evaluated by SAXS and the corresponding intensity correction (V_S^2/V_{real}^2) applied to each distribution.

Table 4.1 – PD_{major} and SAXS intensity correction as a function of sample rotation.

Sample orientation	Projected		Real		SAXS Intensity Correction
	PD_{major} (nm)	Volume (nm^3)	D_{major} (nm)	Volume (nm^3)	
0°	8.3	571	16.1	1117	0.261
5°	8.7	658			0.347
25°	11.9	1685			2.275
45°	12.8	2097			3.524

Figure 4.11 shows the particle dimension distributions estimated by SAXS (Fig. 4.11(a)) and the effect of the intensity correction applied to the results (Fig. 4.11(b)). The huge differences between the results for samples oriented at 0° and 45° are readily apparent. The integral of the curves for measurements at different angles are similar once corrected, as expected, since the total volume of NCs should not be affected by the measurement angle.

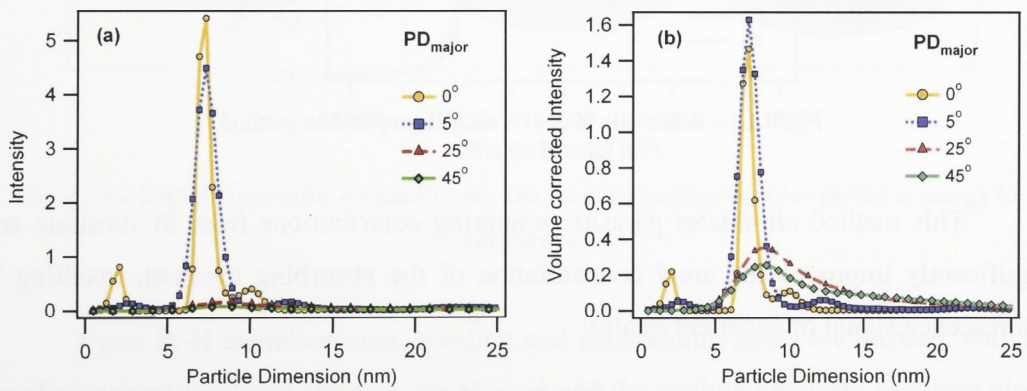

Fig. 4.11 – (a) Particle dimension distribution estimated by SAXS (non-corrected) and (b) the same distributions corrected using Eq. (4.2) (correction values are listed in Table 4.1).

4.4 – XAS sample preparation method

For x-ray absorption spectroscopy (XAS), including both the extended (EXAFS) and near edge (XANES) regions, the NC samples were prepared according to the schematic shown in Fig. 4.12. Approximately 480 μm of the Si substrate were removed from the SiO_2/NC layer by mechanical grinding (Fig. 4.12(a)). Subsequently, the samples were immersed in a KOH solution where the remaining Si substrate was chemically etched (Fig. 4.12(b)). The SiO_2/NC films were then stacked together (approximately 10 fold) between kapton films (Fig. 4.12(c)).[19, 20]

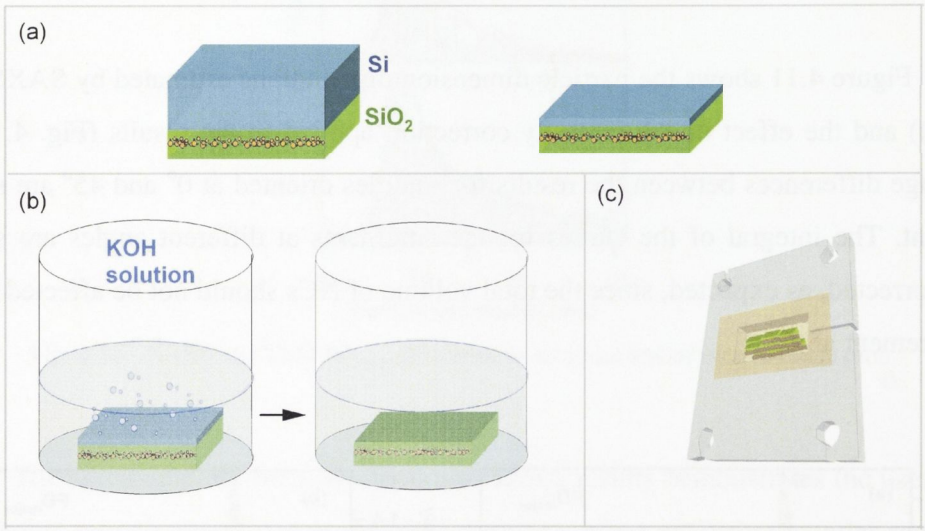

Fig. 4.12 – Schematic of XAFS sample preparation method.

This method eliminates parasitic scattering contributions from Si substrate and significantly improves the areal concentration of the absorbing element, resulting in fluorescence signal of excellent quality.

4.5 – XANES analysis of Pt NCs

Following the XANES discussion presented in Chapter III, the L_3 edge (also called white line) represents electronic transitions from a core level $2p_{3/2}$ to vacant *d* states of the absorbing atom.[21] Thus, the *d* electron-vacancy present in Pt metal (see Fig.

4.13) results in a prominent white line peak (as shown in Fig. 4.14) that is absent in the XANES of Au, for example, where the *d* states are completely filled.

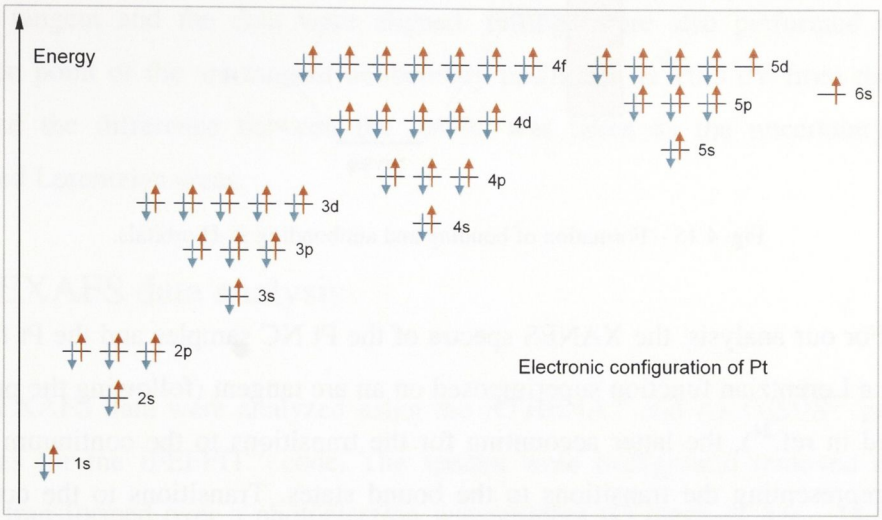

Fig. 4.13 – Electronic ground state configuration of a neutral Pt atom.

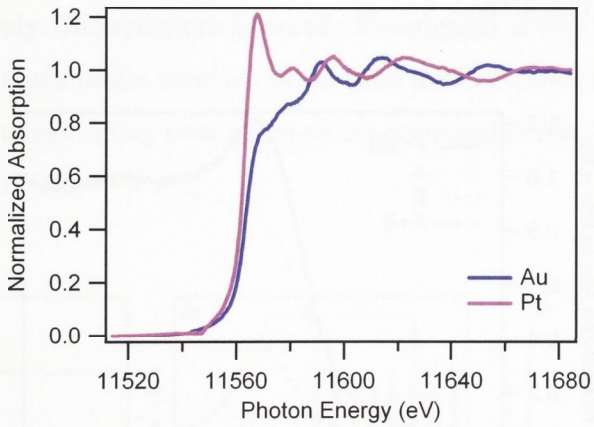

Fig. 4.14 – XANES region for Au and Pt foils. The Au edge position has been shifted in energy for comparison.

Upon Pt-H chemisorption, bonding and antibonding states are created, with the bonding orbital localized closer to the H atom and the antibonding state localized closer to the Pt atom, as shown in Fig. 4.15.[22] As a consequence, the area of the white line increases proportionally with the amount of H chemisorbed by Pt atoms. At the same time, size-related perturbations in the NC electronic properties (for NCs < ~3 nm) are manifested in the XANES data as an increase in the white line intensity and a positive shift in the absorption edge energy relative to bulk Pt.[23]

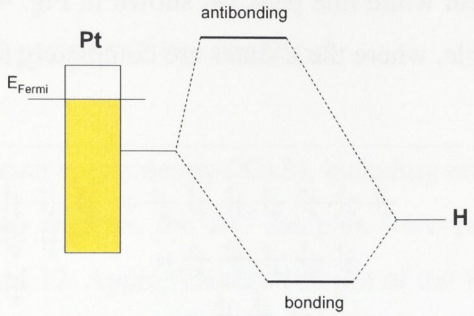

Fig. 4.15 – Formation of bonding and antibonding Pt-H orbitals.

For our analysis, the XANES spectra of the Pt NC samples and the Pt foil were fitted to a Lorentzian function superimposed on an arc tangent (following the procedure described in ref.[24]), the latter accounting for the transitions to the continuum and the former representing the transitions to the bound states. Transitions to the continuum were considered the same for all samples. Fitting was performed with aligned inflection points of the arc-tangent and the data. The separate contributions to the spectrum for the Pt foil are shown in Fig. 4.16.

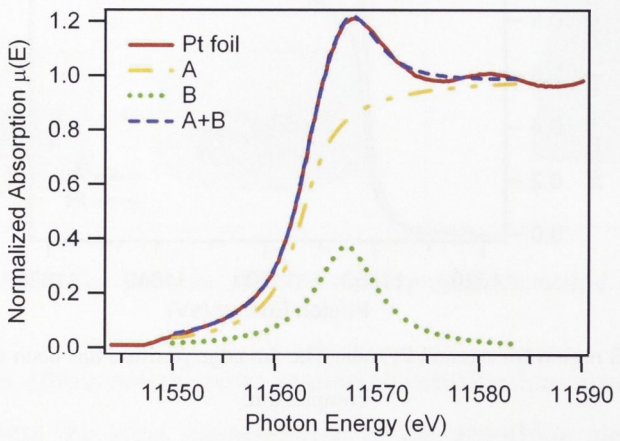

Fig. 4.16 - Normalized XANES spectrum for the L_3 edge of the Pt foil fitted with a Lorentzian superimposed on an arc tangent curve (A+B). The individual curves are also shown (A-arc tangent, B-Lorentzian).

The area encompassed by the Lorentzian was considered proportional to the number of *d* electron vacancies in each sample.[24, 25] Given that size-related effects are apparent only for NCs smaller then 3 nm, independent of the annealing environment, the difference between the Lorentzian area of the NC samples (> 3 nm) and the foil is an

indicative of the amount of H chemisorbed in the sample, for each Pt-H bond will generate one extra *d* electron vacancy in the Pt atom.[22]

The best fit to the experimental data was obtained when the inflection points of the arc tangent and the data were aligned. Fittings were also performed with the inflection point of the arc tangent deliberately positioned at +0.5 eV from the Pt foil edge and the difference between the results was taken as the uncertainty of the integrated Lorentzian areas.

4.6 – EXAFS data analysis

EXAFS data were analyzed using the ATHENA[26] and ARTEMIS[26] programs, interfaces for the IFEFFIT[27] code. The spectra were background removed and then Fourier transformed over a photoelectron wavenumber (k) range of 4.9 – 14.6 Å^{-1}, as shown in Fig. 4.17(a) and (b). The window upper and lower limits are chosen to avoid contribution from the XANES region and excessive noise coming from the end of the spectrum, respectively. The spectrum is usually k^2-weighted to highlight the signal from higher k. Structural parameters were extracted from the first coordination shell, isolated by inverse Fourier transforming over a non-phase-corrected radial distance (R) range of 1.8 – 3.1 Å (Fig. 4.17(c)).

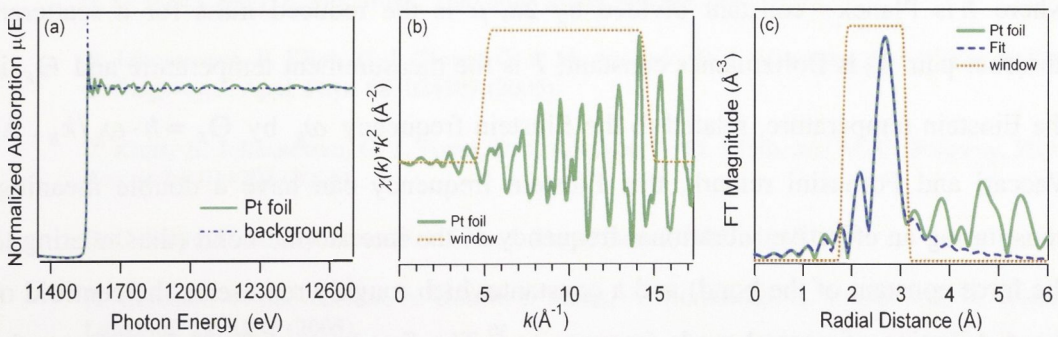

Fig. 4.17 – EXAFS spectra of Pt foil: (a) normalized absorption of Pt foil as a function of photon energy and spline function used for background removal, (b) k^2-weighted and (c) Fourier-transformed spectra with the fitting to the first NN apparent. The window in (b) highlights the region used in the Fourier transformation, while in (c) it indicates the first shell coordination number, where the fitting was performed.

Theoretical standards generated by the FEFF8 code[28] were fitted to the experimental spectra, as shown in Fig. 4.17(c). The amplitude reduction factor (S_0^2) and energy shift parameter (ΔE_0) were determined for the Pt foil and then kept constant for all the NC samples.

4.6.1 – Temperature-dependent EXAFS analysis

Temperature-dependent EXAFS analysis was also performed with the coordination number (*CN*) for each NC sample determined from the lowest temperature data and kept constant thereafter, given the *CN* is not measurement temperature dependent. A fixed *CN* value of 12 was used for the Pt foil at all temperatures.

The experimental data was analyzed in two steps. First, the mean interatomic distance (*R*), mean-square relative displacement (MSRD or σ^2) and asymmetry (third cumulant or C_3) for the first shell around the absorbing atom was determined from individual fits to each spectrum. The values obtained for the MSRD were plotted as a function of temperature and then fitted with a correlated Einstein model [29, 30] given by:

$$\sigma^2 = \frac{\hbar^2}{2\mu k_B \Theta_E} \cdot \coth\left(\frac{\Theta_E}{2T}\right) + \sigma^2_{static} \qquad (4.5)$$

where $\hbar$ is Planck's constant divided by 2π, μ is the reduced mass for a scatterer-absorber pair, k_B is Boltzmann's constant, T is the measurement temperature and Θ_E is the Einstein temperature, related to the Einstein frequency ω_E by $\Theta_E = \hbar \cdot \omega_E / k_B$. As Vaccari and Fornasini remark, this Einstein frequency can have a double meaning, constituting an effective vibrational frequency of the interatomic bond (thus relating to the force constant of the bond) and a constant which roughly represents the centroid of the distribution of normal mode frequencies.[30] The first term of Eq.(4.5) accounts for the thermal contribution to the total disorder, while the second term (σ^2_{static}) corresponds to disorder of structural origin.

In the second step, to reduce the correlation between *R* and C_3 during the fitting and consequently improve the quality of the results, the C_3 values were restrained to

follow the relation derived from the anharmonic one-dimensional effective potential shown in refs. [29, 31]:

$$C_3(T) = \frac{k_3 \cdot k_B^2 \cdot \Theta_E}{2 \cdot k_{eff}^3} \cdot \frac{1+10z+z^2}{(1-z)^2} + C_{3static} \ , \tag{4.6}$$

where $z \equiv \exp(-\Theta_E/T)$, k_3 is the cubic anharmonic force constant, $C_{3static}$ is the asymmetry from structural contributions and k_{eff} is the effective harmonic spring constant defined as $k_{eff} = \mu \cdot k_B^2 \cdot \hbar^2 \cdot \Theta_E^2$.

In this second step, all datasets at different temperatures for a given sample were fitted simultaneously with S_0^2, ΔE_0, CN and MSRD values fixed to those obtained from the individual dataset fits. While C_3 was restrained using equation (4.6), R was freely floated.

References

1 J. P. McCaffrey, Ultramicroscopy **38**, 149 (1991).

2 J. P. McCaffrey, Microsc Res Tech **24**, 180 (1993).

3 S. D. Walck and J. P. McCaffrey, Thin Solid Films **308-309**, 399 (1997).

4 B. Johannessen, P. Kluth, C. J. Glover, G. d. M. Azevedo, D. J. Llewellyn, G. J. Foran, and M. C. Ridgway, J. Appl. Phys. **98**, 024307 (2005).

5 P. Kluth, B. Johannessen, G. J. Foran, D. J. Cookson, S. M. Kluth, and M. C. Ridgway, Phys. Rev. B **74**, 014202 (2006).

6 D. C. Bazin, D. A. Sayers, and J. J. Rehr, J. Phys. Chem. B **101**, 11040 (1997).

7 H. Borchert, V. Shevchenko, A. Robert, I. Mekis, A. Kornowski, G. Grubel, and H. Weller, Langmuir **21**, 1931 (2005).

8 M. Buljan, K. Salamon, P. Dubcek, S. Bernstorff, I. D. Desnica-Frankovic, O. Milat, and U. V. Desnica, Vacuum **71**, 65 (2003).

9 U. V. Desnica, P. Dubcek, I. D. Desnica-Frankovic, M. Buljan, K. Salamon, O. Milat, S. Bernstorff, and C. W. White, Nucl. Instr. and Meth. B **200**, 191 (2003).

10 P. Dubcek, U. V. Desnica, I. D. Desnica-Frankovic, S. Bernstorff, and A. Meldrum, Nucl. Instr. and Meth. B **200**, 138 (2003).

[11] A. Guinier and G. Fournet, *Small-Angle Scattering of X-Rays* (John Wiley and sons, New York, 1955).

[12] J. A. Potton, G. J. Daniell, and B. D. Rainford, J. Appl. Cryst. **21**, 663 (1988).

[13] P. Fratzl, F. Langmayr, and O. Paris, J. Appl. Cryst. **26**, 820 (1993).

[14] R. J. Rule and T. M. W. Nye, Nucl. Instr. and Meth. B **97**, 248 (1995).

[15] W. Ruland and B. Smarsly, J. Appl. Cryst. **38**, 78 (2005).

[16] J. A. Potton, G. J. Daniell, and B. D. Rainford, J. Appl. Cryst. **21**, 891 (1988).

[17] P. R. Jemian and A. J. Allen, J. Appl. Cryst. **27**, 693 (1994).

[18] J. Ilavsky, available at http://usaxs.xor.aps.anl.gov/staff/ilavsky/irena.html.

[19] M. C. Ridgway, C. J. Glover, P. Kluth, B. Johannessen, and G. J. Foran, AIP Conference Proceedings **882**, 908 (2007).

[20] A. Cheung, G. d. M. Azevedo, C. J. Glover, D. J. Llewellyn, R. G. Elliman, G. J. Foran, and M. C. Ridgway, Appl. Phys. Lett. **84**, 278 (2004).

[21] F. W. Lytle, P. S. P. Wei, R. B. Greegor, G. H. Via, and J. H. Sinfelt, J. Chem.Phys. **70**, 4849 (1979).

[22] B. Hammer and J. K. Norskov, Nature **376**, 238 (1995).

[23] A. I. Frenkel, C. W. Hills, and R. G. Nuzzo, J. Phys. Chem. B **105**, 12689 (2001).

[24] A. K. Shukla, R. K. Raman, N. A. Choudhury, K. R. Priolkar, P. R. Sarode, S. Emura, and R. Kumashiro, J. Electroanal. Chem. **563**, 181 (2004).

[25] M. Fernandez-Garcia, Catal. Rev. **44**, 59 (2002).

[26] B. Ravel and M. Newville, J. Synchrotron Rad. **12**, 537 (2005).

[27] M. Newville, J. Synchrotron Rad. **8**, 322 (2001).

[28] J. J. Rehr and R. C. Albers, Rev. Mod. Phys. **72**, 621 (2000).

[29] L. L. Araujo, P. Kluth, G. D. M. Azevedo, and M. C. Ridgway, Phys. Rev. B **74**, 184102 (2006).

[30] M. Vaccari and P. Fornasini, J. Synchrot. Radiat. **13**, 321 (2006).

[31] A. I. Frenkel and J. J. Rehr, Phys. Rev. B **48**, 585 (1993).

CHAPTER V

PLATINUM NANOCRYSTAL FORMATION

This chapter reports on the formation of Pt NCs in amorphous SiO_2 using ion implantation and thermal annealing. The NCs were investigated by laboratory and synchrotron based techniques, including TEM, SAXS and XAFS. The influence of the annealing conditions on the NC growth and structure was studied, as well as the preferential nucleation at defects produced in the matrix. Temperature-dependent EXAFS analyses were also performed.

5.1 – Introduction

Ion implantation is one of many techniques used to form embedded NCs[1-5] and is advantageous for the control of the depth and concentration of implanted atoms. Furthermore, the protection offered by the surrounding matrix enhances NC stability and durability.[6] Ion irradiation of the SiO_2 matrix *subsequent* to metal NC formation represents a means of altering the NC size distributions[7-9] to better suit specific applications. In general, such applications are governed by the unique optical,[10] catalytic[11] and therapeutic[12] properties of metal NCs that can differ dramatically from those of their bulk counterparts.[13] Finite size effects and the high proportion of surface atoms in a NC are responsible for these differences.

Given NC properties depend on size and structure,[14] it is important to understand the influence of the synthesis parameters on NC formation. This chapter reports on the formation of Pt NCs in amorphous SiO_2 (a-SiO_2) by ion implantation, focusing on the influence of the annealing conditions on NC size and structure, as well as the influence of defects produced in a-SiO_2 (by ion irradiation *prior* to metal NC formation) on NC size. In addition, temperature-dependent EXAFS measurements were performed to investigate the thermal/vibrational properties of embedded Pt NCs.

5.2 – Defect-mediated nucleation of Pt nanocrystals

In this study, we have sought to investigate how defects produced in a-SiO_2 by ion irradiation *prior* to metal NC formation can subsequently influence the size of Pt NCs formed by ion implantation. (We note that Pt NC formation in SiO_2 has received scant attention in the literature.) High-energy Ge ion irradiation was used to generate a constant defect distribution over the extent of a thin SiO_2 layer. Pt ions were then implanted into the structurally-modified SiO_2 layer and the size evolution of Pt NCs was measured as a function of the Ge-ion fluence. We show that prior Ge-ion irradiation yielded a significant reduction in mean Pt NC diameter and thus demonstrate a simple means of controlling the Pt NC size.

5.2.1 - Experimental

5 MeV Ge* ions were implanted into amorphous, 2 μm thick SiO_2 (a-SiO_2) films (thermally grown on (100) Si substrates) at liquid N_2 temperature with ion fluences ranging from $1x10^{15}$ to $5x10^{16}$ cm^{-2}. Samples were then implanted with 4.5 MeV Pt ions, again at liquid N_2 temperature, to a fluence of $1x10^{17}$ cm^{-2}. Following implantation, samples were annealed in forming gas (FG, 95% N_2/5% H_2) for 1 hr at 1100 °C to promote NC growth.

TEM and RBS measurements were used to investigate the NC size as a function of depth and the concentration of implanted Pt ions, respectively. Details on the experimental setup, sample preparation methods and data analysis are described in Chapters II and IV.

5.2.2 – Results and Discussion

The depth distributions of irradiated and implanted atoms and the number of vacancies generated by both Ge and Pt ions, as simulated by SRIM 2008[15], are plotted in Fig. 5.1. Clearly the Ge atoms are located at depths far beyond the SiO_2 layer (thus negating impurity effects) while the Pt atomic concentration has a maximum within the SiO_2 layer at a depth of approximately 1.4 μm.† Vacancy production by Ge ions is nearly constant over the extent of the SiO_2 layer while, as expected, the maximum in Pt-induced vacancy production is at slightly lesser depths (~1.1 μm) than the atomic concentration maximum.

Figure 5.2 shows representative results obtained by TEM. Images displayed in the same row represent different depths in the same sample, while different samples at the same depths are displayed vertically, with increasing Ge irradiation fluence from top to bottom. The top row shows the sample without Ge irradiation where differences in

* Ge ions were chosen for their feasibility and almost constant nuclear energy deposition in the region of interest.

† The SRIM depth scales for the Pt-induced vacancy production and atomic depth distribution were increased by 0.15 μm to coincide with the experimental determination of the latter using RBS and TEM. Such differences are possibly due to inaccuracies in some of the simulation parameters, like the Ge stopping power in SiO_2 and sputtering effects, for example.

the NC size as a function of depth are readily apparent. The largest NCs formed at depths of ~1.8 μm below the surface where both the vacancy production and atomic concentration resulting from Pt implantation were lowest. In the samples first irradiated with Ge ions, the second to fourth rows show a progressively decreasing NC size with increasing Ge irradiation fluence at depths of 1.6-1.8 μm. No significant change in NC size is apparent as a function of fluence at 1.5 μm where the vacancy generation due to Pt implantation far exceeds that due to Ge irradiation.

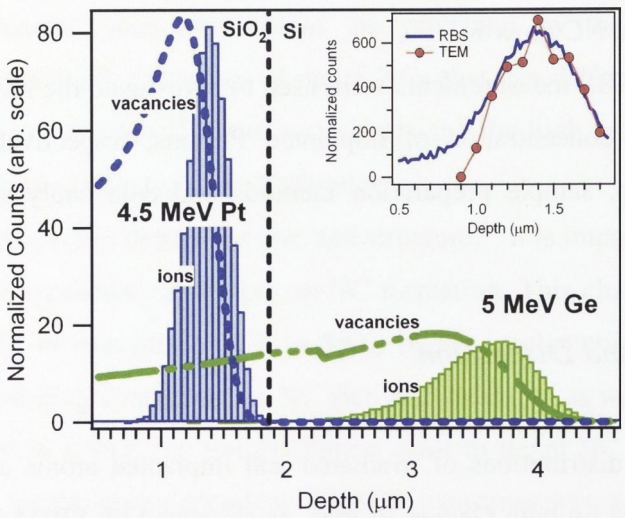

Fig. 5.1 – Ge ($5x10^{16}$ cm^{-2}) and Pt ($1x10^{17}$ cm^{-2}) atomic depth distributions and vacancy production as simulated by SRIM 2008.[16] The inset shows the experimental Pt atomic depth distribution determined by TEM and RBS, used in the rescale of the SRIM data.

Figure 5.3(a) shows a magnified view of the Pt atomic depth distribution and the vacancy production by both Ge and Pt ions, the former corresponding to an irradiation fluence of $5x10^{16}$ cm^{-2}. (Rutherford backscattering spectrometry (not shown) demonstrated the Pt atomic depth distribution was not influenced by either the annealing process or Ge-ion irradiation.) Figure 5.3(b) shows the mean Pt NC diameter as a function of depth over the same region. For depths of 1.6-1.8 μm, the mean NC diameter decreases from ~5.5 nm to ~3.5 nm as the Ge irradiation fluence increases. At lesser depths (1.2-1.5 μm), a slight reduction in NC diameter with increasing Ge irradiation fluence is also apparent despite the vacancy production being dominated by Pt ion implantation. This may reflect Pt NC nucleation on Ge irradiation-induced defects during the early stages of the Pt implantation. Figure 5.3 thus demonstrates that

Pt NC size is not governed by the Pt atomic concentration but by nuclear energy deposition.

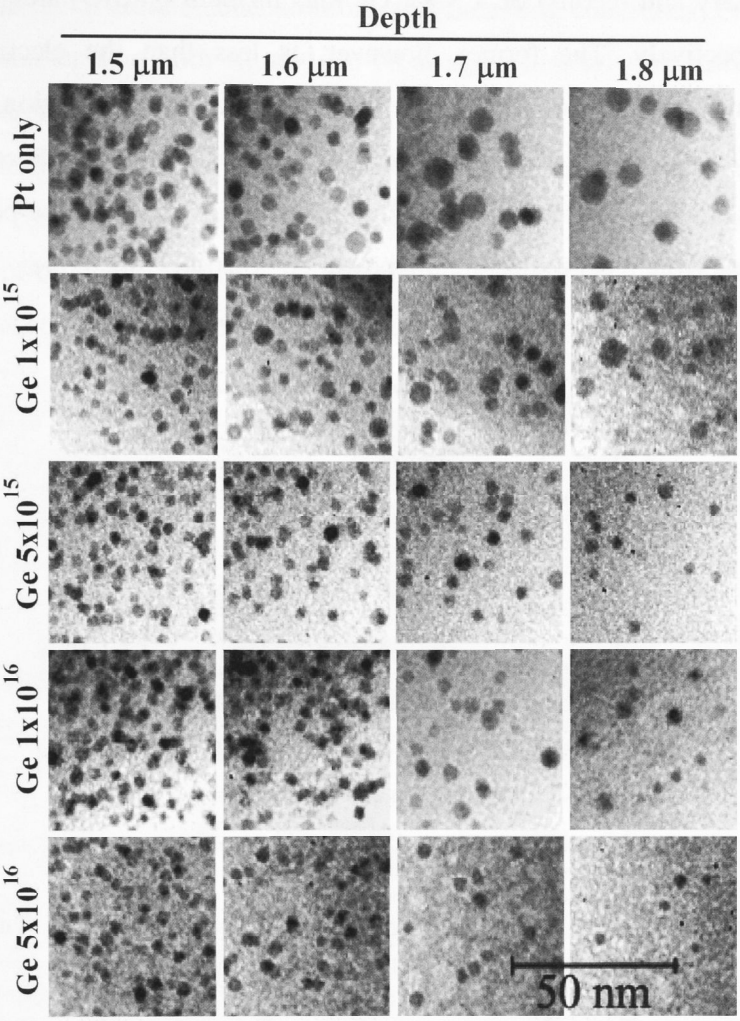

Fig. 5.2 – TEM micrographs of samples implanted with increasing fluences of 5 MeV Ge ions and subsequently implanted with $1x10^{17}$ cm^{-2}. Images in the same row represent different depths for the same sample.

Figure 5.4 shows the mean Pt NC diameter as a function of the total energy deposited in vacancy production (Ge irradiation plus Pt implantation using a full cascades simulation) over the 0.1 μm depth intervals shown in Fig. 5.3. Clearly the mean Pt NC diameter decreases as the total energy deposited in vacancy production increases. Experimental results were best fitted with a power function with the fit included in Fig. 5.4 as a guide for the eye. The mean diameter saturates at ~3 nm when the energy deposited in vacancy production exceeds ~$2x10^{23}$ keV/cm^3. Figure 5.4 thus

quantifies the correlation between Pt NC diameter and nuclear energy deposition. We note that the potential influence of electronic stopping must also be considered. At depths of ~1.7 μm, SRIM values for the total electronic and nuclear stopping (including both the primary and recoils) of 5 MeV Ge ions incident on SiO_2 are ~1.07 and 0.19 keV/nm, respectively. The former, however, is less than the electronic stopping threshold values required for ion hammering and latent track formation in amorphous SiO_2 (~2 keV/nm)[17] and irradiation-induced NC nucleation in Cu-oxide containing glass (~5 keV/nm).[18] Whilst we anticipate negligible influence of the above processes, other effects resulting from electronic stopping power could still be operative.

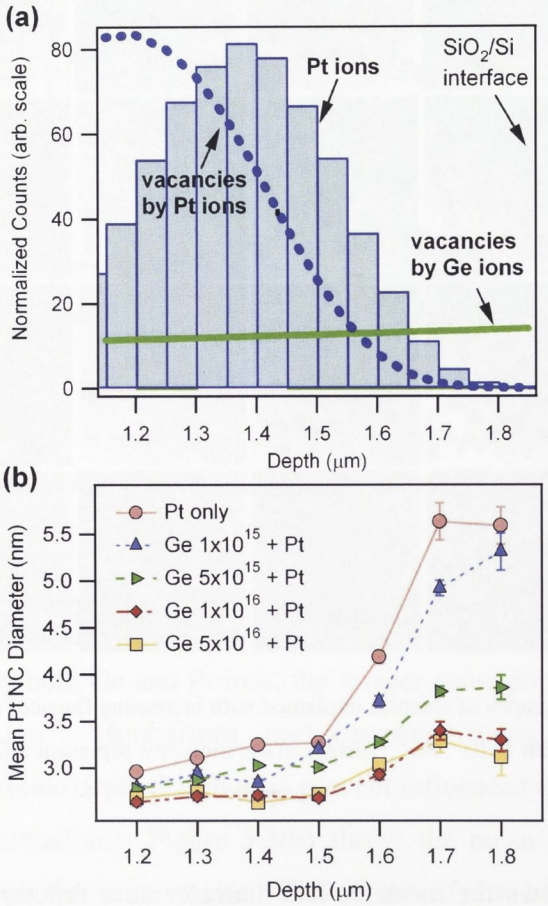

Fig. 5.3 – (a) Pt ($1x10^{17}$ cm^{-2}) atomic depth distribution and vacancy production for Ge irradiation ($5x10^{16}$ cm^{-2}) and Pt implantation over depths of 1.0-1.8 μm (results calculated by SRIM 2008[16]) and (b) mean Pt NC diameter as a function of depth and Ge irradiation fluence for the same region shown in panel (a).

Striking differences are apparent upon a comparison of Pt NC formation, as presented above, with earlier reports for Au[19] and Cu[4] NC formation. For the latter two

metals, the largest NCs are observed at the atomic concentration maximum, in close proximity to the vacancy production maximum. In contrast, the largest Pt NCs observed herein are at the vacancy production minimum (in the absence of Ge ion irradiation). For comparable metal atomic concentrations and annealing conditions, Pt NCs are also significantly smaller than both Au and Cu NCs, again indicative of differences in the nucleation and/or growth processes. We thus speculate that Pt NCs preferentially nucleate on irradiation-induced defects resulting from nuclear energy deposition. A more detailed comparison of NC formation as a function of metal would necessitate consideration of differences in metal diffusivity (in the presence of irradiation-induced disorder), metal solubility and metal/matrix interfacial energies.

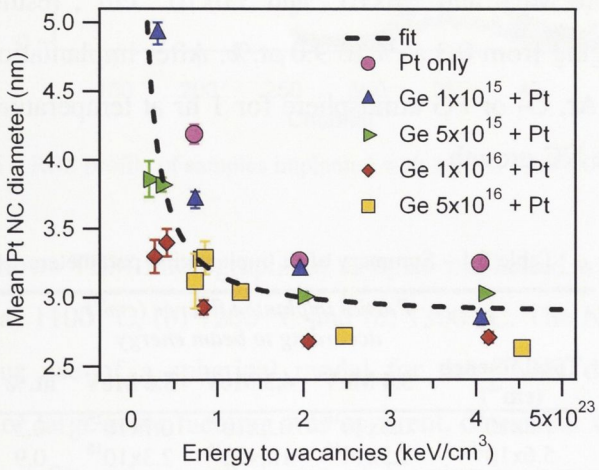

Fig. 5.4 – Mean Pt NC diameter as a function of the total energy deposited in vacancy production, the latter simulated by SRIM 2008.[16]

As noted previously, irradiation-induced structural modifications of a-SiO_2 can be of many forms with examples that include compaction and the formation of O-vacancy centers. However, both the compaction[20] and O-vacancy center concentration[21] saturate when the energy deposited in vacancy production exceeds ~10^{20} keV/cm^3, three orders of magnitude less than that observed herein for the saturation of the mean Pt NC diameter. The observations presented in this study are unlikely the result of a single defect configuration but most probably relate to an ensemble of irradiation-induced structural modifications. A final irradiation-induced structural modification for consideration is the potential influence of atoms, both Si and O, recoiled from the SiO_2 layer by Ge-ion irradiation. The resulting imbalance in vacancy/interstitial

concentrations and stoichiometry (both microscopic and macroscopic) may also influence Pt NC nucleation. Furthermore, such effects may not saturate[22] for the given Ge-ion fluence range.

5.3 – Influence of annealing conditions

5.3.1 – Experimental

Amorphous SiO_2 layers (2 μm thick) were implanted with Pt ions at liquid nitrogen temperature. The energies and fluences are presented in Table 5.1 and vary between 3.4 and 5.6 MeV and $1.8x10^{16}$ and $3.0x10^{17}$ cm^{-2}, resulting in peak atomic concentrations ranging from 0.3 at.% to 9.0 at.%. After implantation, the samples were annealed in either Ar, O_2 or FG atmosphere for 1 hr at temperatures between 500 and 1300 °C to promote NC growth.

Table 5.1 – Summary of Pt implantation parameters

	Partial implanted fluence (cm^{-2}) according to beam energy			
Total fluence (cm^{-2})	**3.4 MeV**	**4.5 MeV**	**5.6 MeV**	**at.%**
$1.8x10^{16}$	$0.5x10^{16}$	$0.6x10^{16}$	$0.7x10^{16}$	0.3
$5.6x10^{16}$	$1.5x10^{16}$	$1.8x10^{16}$	$2.3x10^{16}$	0.9
$1.0x10^{17}$		$1.0x10^{17}$		3.0
$3.0x10^{17}$		$3.0x10^{17}$		9.0

Transmission SAXS measurements were performed to determine the NC size distributions. Additionally, TEM was used to determine the shape and size distribution of selected NC samples. XAS measurements yielded information on the local atomic/electronic structure of the Pt NCs. Details about the experimental setup, sample preparation and data analysis methods can be found in Chapters II, III and IV.

5.3.2 - NC growth

Figure 5.5 shows the RBS profile for samples implanted with Pt at different fluences, where the area under the peak is proportional to the total Pt fluence. Samples implanted with the same fluence but annealed at different temperatures exhibit no

differences in the Pt depth profile (not shown), consistent with no significant redistribution of Pt within the matrix for temperatures up to 1100 °C (as measurable with RBS for the given scattering geometry).

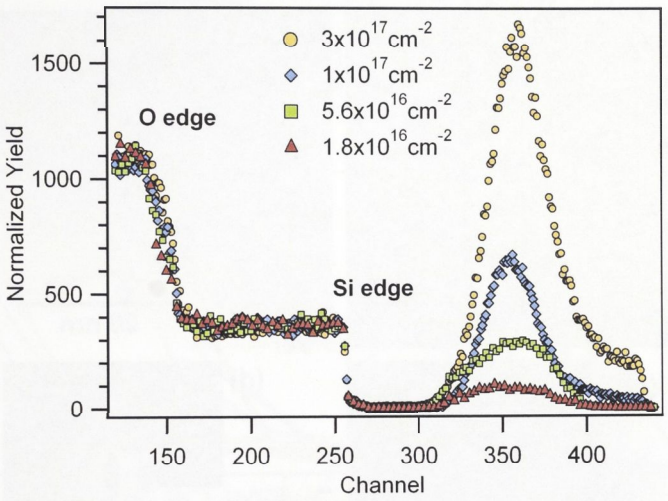

Fig. 5.5 – RBS profile of samples implanted with $1.8x10^{16}$-$3.0x10^{17}$ cm^{-2}.

Figure 5.6 shows TEM micrographs of samples implanted with $1x10^{17}$ cm^{-2} and annealed in FG at (a) 1100 °C, (b) 1200 °C and (c) 1300 °C. The NCs are spherical in shape, justifying our use of a spherical model for the SAXS data analysis. (No definitive evidence of large scale faceting was apparent, consistent with the amorphous nature of the matrix. Should a small degree of faceting be present, we anticipate a negligible influence on the SAXS data analysis.) The largest average particle sizes are observed in samples annealed at the highest temperatures. The diffraction pattern for Pt NCs annealed at 1100 °C (Fig. 5.6(d)) demonstrates the NCs retain the face-centered cubic (FCC) structure characteristic of bulk Pt while the high resolution image of Fig. 5.6(e) shows the NCs are single crystalline.

Figure 5.7 presents x-ray scattering intensities *I(Q)* as a function of scattering vector *Q* and the corresponding size distributions for samples implanted with $1x10^{17}$ cm^{-2} and annealed in Ar, O_2 or FG (note the different horizontal scales in the size distributions). Mean diameters are listed in Table 5.2 which also includes the maximum and standard deviation from a Gaussian fit to the distributions. Though the latter may not always be most accurately described by a Gaussian,[23] the standard deviation is indicative of the extent of NC size variation in a given sample. As shown in Fig. 5.7, the NCs increase in size with increasing annealing temperature for all ambients, though

at a given temperature annealing in Ar yields significantly smaller NCs than annealing in either O_2 or FG. Although these two ambients produce NCs of similar sizes, differences are apparent in the growth rates as a function of temperature.

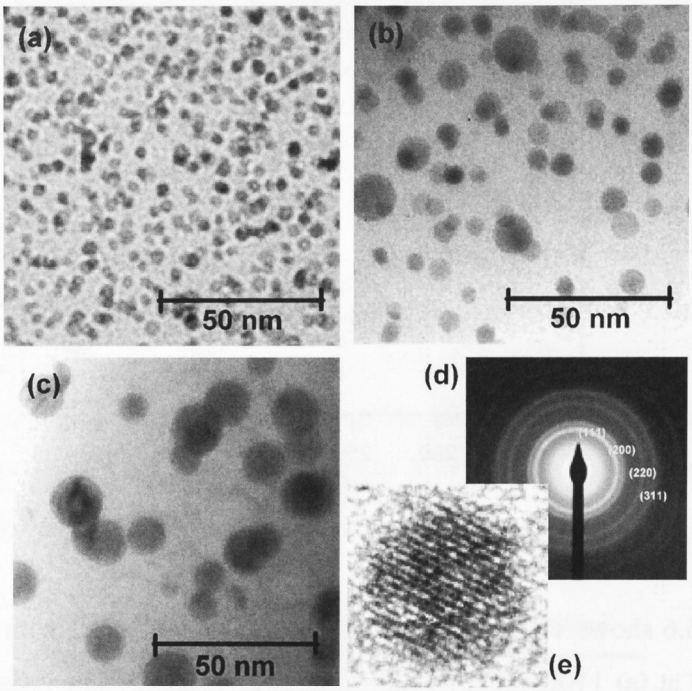

Fig. 5.6 – TEM micrographs of Pt NCs in SiO_2 for an implantation fluence of $1x10^{17}cm^{-2}$ and annealing in FG at (a) 1100 °C, (b) 1200 °C and (c) 1300 °C. (d) Selected area diffraction pattern and (e) high resolution image of an individual NC.

Table 5.2 – Mean NC diameter $\mathbf{D_{mean}}$ obtained from SAXS measurements. **Peak** is the peak of each distribution determined from a Gaussian fit to the experimental distributions, with standard deviation **σ.**

Annealing Temp.	*Argon*			*Oxygen*			*Forming Gas*		
	$\mathbf{D_{mean}}$	**Peak**	**σ**	$\mathbf{D_{mean}}$	**Peak**	**σ**	$\mathbf{D_{mean}}$	**Peak**	**σ**
500 °C	-	-	-	-	-	-	1.2	1.2	0.1
800 °C	1.1	1.0	0.1	1.1	1.1	0.2	1.4	1.2	0.1
900 °C	1.6	1.7	0.3	-	-	-	-	-	-
1000 °C	1.8	1.4	0.2	2.9	2.7	0.5	2.7	2.4	0.4
1100 °C	2.8	2.7	0.4	4.7	4.6	1.1	3.5	3.1	0.5
1200 °C	4.0	3.4	0.6	7.7	7.5	1.6	7.4	6.1	1.3
1300 °C	-	-	-	10.1	10.0	2.2	13.9	12.3	2.9

* $\mathbf{D_{mean}}$, **Peak** and **σ** values are in units of nm.

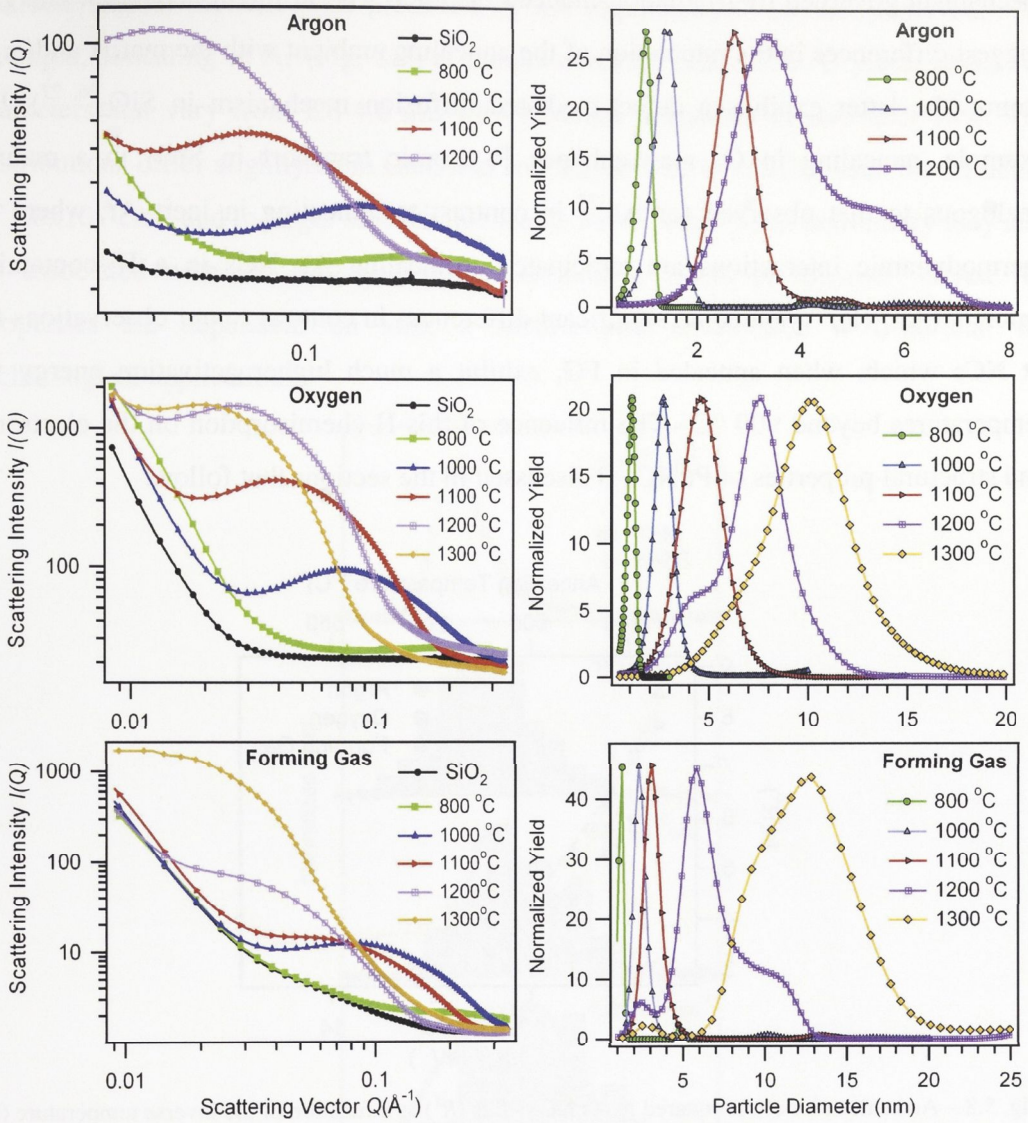

Fig. 5.7 – (left) Measured SAXS intensity $I(Q)$ as a function of the scattering vector Q and (right) respective diameter distributions for samples implanted with $1x10^{17}cm^{-2}$ and annealed in either Ar, O_2 or FG at the temperatures indicated. The scattering contribution of unimplanted SiO_2 is also plotted for comparison. Note the different horizontal scales on the diameter distributions.

Figure 5.8 shows an Arrhenius plot of the squared mean NC radius for samples annealed in Ar, O_2 or FG. Activation energies (E_{act}) for Pt NC growth were 0.83 ± 0.10 and 1.34 ± 0.05 eV for annealing in Ar and O_2, respectively. Two distinct temperature regimes for NC growth are apparent for annealing in FG - at temperatures < 900 °C, E_{act} = 0.09 ± 0.01 eV while above 900 °C, E_{act} = 1.93 ± 0.33 eV. Similar observations have been reported for other metals,[24, 25] where the sluggish and effectively temperature independent increase in NC size at low temperatures was attributed to a growth

mechanism governed by irradiation-induced disorder. The different activation energies suggest differences in the interaction of the annealing ambient with the matrix and/or Pt atoms (the latter exhibits a defect-mediated diffusion mechanism in SiO_2[26, 27]). For example, annealing in O_2 may enhance Pt atomic transport in SiO_2 in a manner analogous to that observed for Au,[25] in contrast to annealing in inert Ar, where no thermodynamic interactions are anticipated. Annealing Au NCs in a H_2-containing ambient (Ar : H_2)[25] yielded no significant differences in contrast to our observations for Pt NCs which, when annealed in FG, exhibit a much higher activation energy for temperatures beyond 900 °C. The influence of this H chemisorption on the electronic and structural properties of Pt NCs is discussed in the sections that follow.

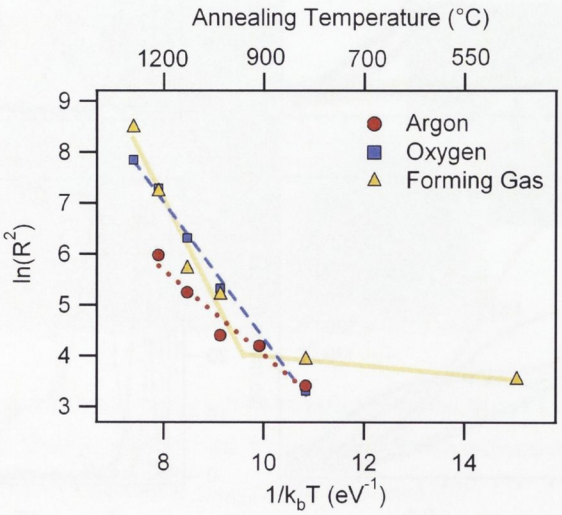

Fig. 5.8 – Arrhenius plot of the squared mean NC radius (R^2) as a function of the inverse temperature (k_b is the Boltzmann constant, T is the annealing temperature). The corresponding annealing temperatures are shown on the top. The lines are linear fits to the experimental data.

Figure 5.9 compares the size distributions determined from SAXS and TEM for samples implanted with different fluences and annealed in FG at 1100 °C for one hour. In contrast to other metals,[4, 5] the implantation fluence does not significantly affect the mean Pt NC size, therefore, it must influence the NC density (number of particles per unit volume). Greater Pt fluence (or equivalently greater concentration) results in greater disorder, hence, greater NC density, consistent with the results shown in section 5.2.[2] Samples with concentration maxima ranging from 0.3-9.0 at. % exhibit mean NC diameters varying from only 3.4-2.9 nm. Higher fluences yield smaller NCs as a result of the disorder-mediated nucleation of Pt NCs. Similarly, the broad size distributions

characteristic of metallic NCs produced by ion implantation[28] are not observed. For example, annealing in Ar (Fig. 5.7) at temperatures of 1100-1200 °C yields mean NC diameters that vary from 2.8-4.0 nm with standard deviations of less than 15%. The distributions differ slightly from Gaussian and are skewed to smaller sizes for a fluence of $1.8x10^{16}$ cm^{-2} and to larger size for fluences $\geq 5x10^{16}$ cm^{-2}. Such asymmetry may also be associated with the different, fluence-dependent extent of disorder. Given NC properties are dependent on size, a narrow size distribution is beneficial for technological applications.

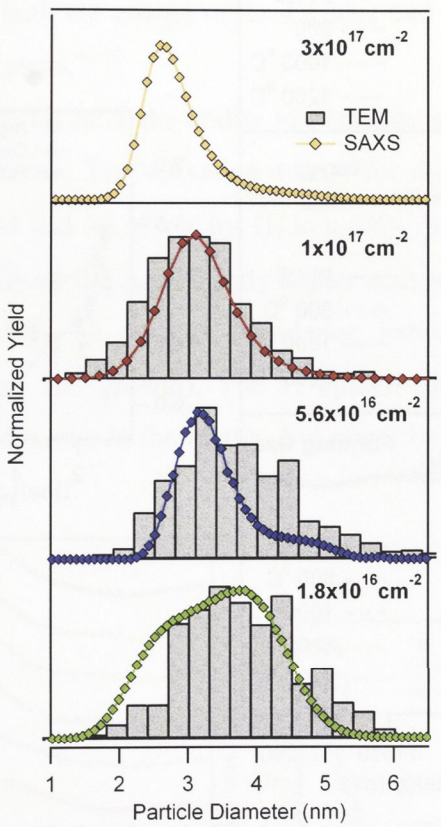

Fig. 5.9 –Diameter distributions obtained from SAXS and TEM measurements for samples implanted with different fluences (as indicated in each panel) and annealed in FG at 1100 °C.

5.3.3 – H chemisorption

Figure 5.10(a) shows Pt L_3 near-edge absorption spectra for samples annealed in Ar, O_2 or FG. The difference in energy between the inflection points of the absorption edges (E_i) for NC samples and the crystalline foil is shown in Fig. 5.10(b) as a function of NC size. Annealing in Ar or O_2 ambients yields similar results in both Figs. 5.10(a)

and (b). For NCs with mean diameter < 2.0 nm, E_i is shifted to higher energies (0.5-1.5 eV) relative to the crystalline foil as a result of finite-size-related perturbations to the electronic properties of Pt NCs.[13] This shift decreases with increasing diameter, as the NCs become more bulk-like and is negligible beyond 4.0 nm. In contrast, samples annealed in FG exhibit the largest shift (1.5-2.0 eV) for the biggest NCs.

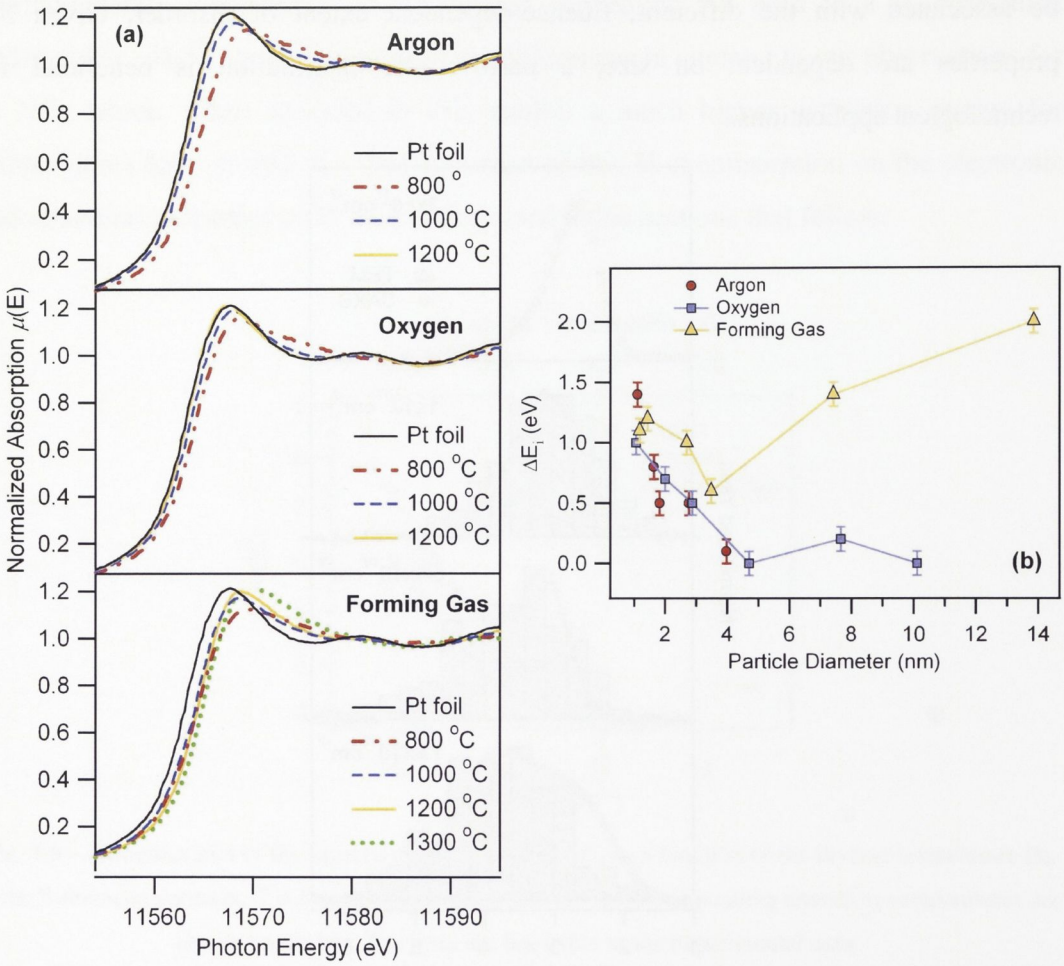

Fig. 5.10 – (a) Normalized XANES spectra for the L3 edge of the Pt foil and the NC samples annealed in either Ar, O_2 or FG, at different temperatures, as indicated on the graphs. All spectra were energy calibrated relative to a Pt reference foil measured simultaneously with the samples. (b) Difference between E_i of the NC samples and the Pt foil as a function of NC diameter, where E_i is the inflection point of the Pt L_3 edge.

The white lines of samples annealed in Ar, O_2 and FG were fitted as described in Chapter IV and the fits for samples annealed in the latter atmosphere are shown in Fig. 5.11(a). The area encompassed by the Lorentzian was considered proportional to the number of *d* electron vacancies.[29, 30] For NCs > 3.0 nm (where finite-size-related perturbations are negligible), the difference between the area of the Lorentzian and that

of the foil is indicative of the amount of H chemisorbed (where each Pt-H bond generates one extra *d* electron vacancy in the Pt atom[31]). Fitting results are listed in Table 5.3 and plotted in Fig. 5.11(b) as a function of NC size. For NCs < 3.0 nm in diameter, results are independent of ambient and dominated by finite-size effects. For larger particles, annealing in Ar or O_2 yields near bulk-like behavior while annealing in FG results in a significant increase in white line area as consistent with H chemisorption. For such samples, the shift in E_i apparent in Fig. 5.10(b) results from the broadening of the white line. Our results are consistent with previous studies for supported Pt NCs where both the energy of the L_3 edge and white line intensity where influenced by H chemisorption.[32-34]

Both atomic H and H_2 have the ability to permeate a-SiO_2 with diffusion rates that increase with temperature. The activation energy for diffusion was reported to be 0.16-0.19 eV for atomic H and ~0.38 eV for H_2 in a-SiO_2 (for temperatures between 5 and 80 °C, at least).[35, 36] Given the significantly higher activation energy for NC growth (annealing in FG, Fig. 5.8), no obvious correlation between the two processes is apparent (H diffusion and NC growth). The H uptake by the Pt NCs is thus not hampered by the H diffusion rate in the matrix, but rather by size related effects and/or the annealing temperature itself.

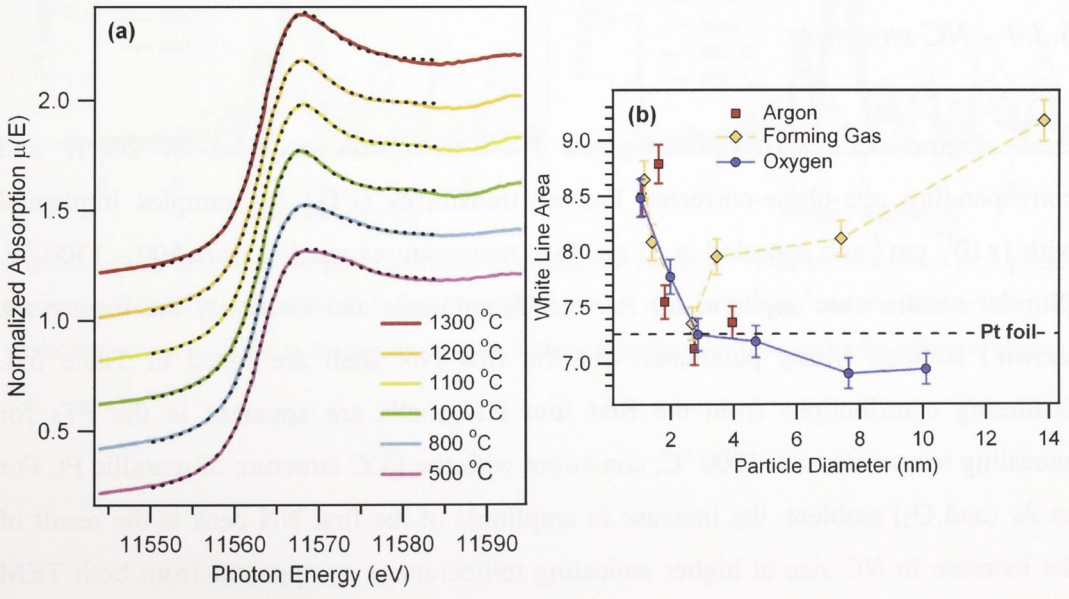

Fig. 5.11 – (a) Normalized XANES spectra for the Pt L_3 edges of samples implanted with $1x10^{17}$ cm^{-2} and annealed in FG at the temperatures shown. The doted lines represent the fitting to the data. Spectra vertically offset for clarity. (b) Area of the Lorentzian fitted to the XANES data (white line peak) as a function of NC diameter.

Table 5.3 – Results obtained by fitting a Lorentzian curve to the white line of the XANES spectra for each annealing environment at different temperatures. **Area Lor.** is the area of Lorentzian and $N_{NC\text{-}foil}$ is the difference between the area of the Lorentzian fit to the NC and the Pt foil, shown in percentage relative to the area for the Pt foil. The light green shaded values are the ones dominated by the finite-size effects.

Annealing Temp.	*Argon*		*Oxygen*		*Forming Gas*	
	Area Lor.	$N_{NC\text{-}foil}$ (%)	**Area Lor.**	$N_{NC\text{-}foil}$ (%)	**Area Lor.**	$N_{NC\text{-}foil}$ (%)
500 °C	-	-	-	-	8.7	18.8 ± 0.8
800 °C	8.5	16.6 ± 0.6	8.5	16.5 ± 3.3	8.1	4.0 ± 7.1
900 °C	8.8	20.7 ± 4.3	7.8	6.8 ± 1.0	-	-
1000 °C	7.6	3.7 ± 0.6	7.3	-0.4 ± 0.4	7.4	1.1 ± 1.2
1100 °C	7.1	-2.1 ± 1.5	7.2	-1.2 ± 1.3	8.0	9.3 ± 0.6
1200 °C	7.4	0.4 ± 0.4	6.9	-5.2 ± 0.5	8.1	11.5 ± 0.8
1300 °C	-	-	6.9	-4.7 ± 0.2	9.2	26.1 ± 2.2

Following Kubota and co-workers[37, 38], quantification of the H content from XANES analysis would necessitate an appropriate calibration curve, at present lacking for our materials system (though under development). None the less, our qualitative findings demonstrate the applicability of this form of XANES analysis to the study of H chemisorption in Pt NCs and, as shown in the following section, are invaluable for the interpretation of the EXAFS results.

5.3.4 – NC structure

Figure 5.12 shows k^2-weighted EXAFS spectra acquired at 20 K and corresponding non-phase-corrected Fourier transforms (FTs) for samples implanted with $1x10^{17}$ cm^{-2} and annealed in Ar or FG at temperatures ranging from 500 – 1300 °C. (Similar results were apparent for Ar and O_2 ambients and thus only the former are shown.) Refined fitting parameters for the first NN shell are listed in Table 5.4. Scattering contributions from the first four NN shells are apparent in the FTs for annealing temperatures > 1000 °C, consistent with the FCC structure of metallic Pt. For an Ar (and O_2) ambient, the increase in amplitude of the first NN peak is the result of the increase in NC size at higher annealing temperatures as apparent from both TEM and SAXS (Figs. 5.6 and 5.7, respectively). With reference to Table 5.4, the decrease in surface-to-volume ratio with increasing NC size yields an increase in average CN (due to a lesser relative fraction of undercoordinated surface atoms) and a decrease in structural disorder (due to a lesser relative fraction of relaxed/reconstructed surface

atoms[‡]) both of which contribute to the increase in amplitude. For samples annealed in FG, the largest NCs (1300 °C) yield an amplitude less than that of smaller sized NCs (1000-1200 °C).

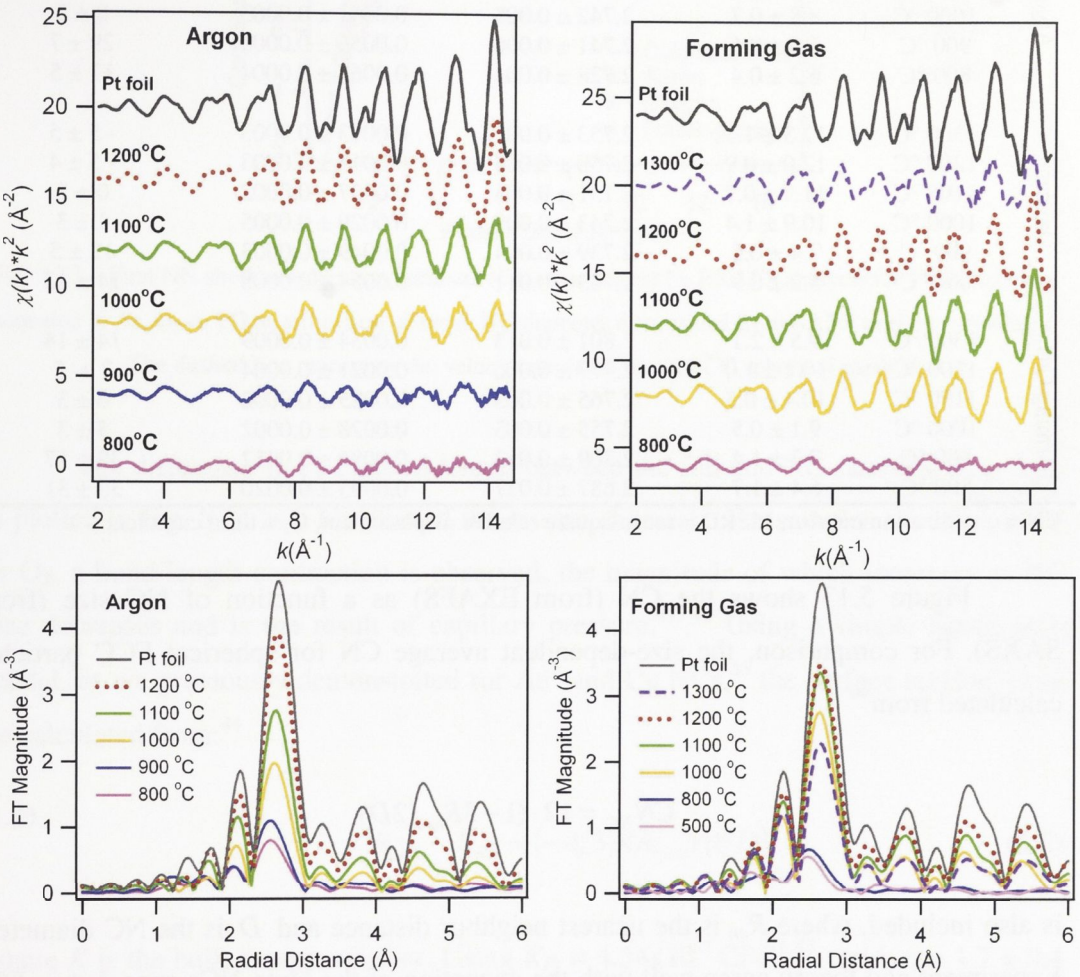

Fig. 5.12 – (top graphs) k^2-weighted and (bottom graphs) the respective Fourier-transformed (non-phase corrected) EXAFS spectra of the Pt foil and Pt NCs implanted with $1x10^{17}$ cm^{-2} and annealed in Ar or FG at the temperatures shown in the graphs. Spectra in the top graphs have been vertically offset for clarity.

[‡] A complete description of disorder at NC surface layers can be found in ref.[39]

Table 5.4 – Structural parameters obtained from first NN shell EXAFS analysis.

	Sample	CN (atoms)	Bond-length (Å)	MSRD (Å^2)	C_3 (10^{-5} Å^3)
	Pt foil	12	2.759 ± 0.001	0.0017 ± 0.0001	-2 ± 1
Argon	1200 °C	11.5 ± 0.7	2.745 ± 0.003	0.0023 ± 0.0002	-4 ± 3
	1100 °C	9.8 ± 0.5	2.747 ± 0.003	0.0031 ± 0.0002	5 ± 3
	1000 °C	8.8 ± 0.7	2.742 ± 0.005	0.0041 ± 0.0003	8 ± 5
	900 °C	6.6 ± 0.6	2.741 ± 0.006	0.0055 ± 0.0005	29 ± 7
	800 °C	6.2 ± 0.4	2.728 ± 0.004	0.0067 ± 0.0004	17 ± 5
Oxygen	1300 °C	12.3 ± 1.1	2.753 ± 0.005	0.0013 ± 0.0003	- 5 ± 5
	1200 °C	12.0 ± 0.9	2.750 ± 0.004	0.0015 ± 0.0003	- 5 ± 4
	1100 °C	11.9 ± 0.7	2.751 ± 0.003	0.0017 ± 0.0002	0 ± 3
	1000 °C	10.9 ± 1.4	2.743 ± 0.008	0.0029 ± 0.0005	1 ± 3
	900 °C	7.4 ± 0.5	2.739 ± 0.004	0.0049 ± 0.0003	12 ± 5
	800 °C	5.2 ± 0.9	2.723 ± 0.011	0.0054 ± 0.0008	14 ± 13
Forming Gas	1300 °C	9.5 ± 2.1	2.801 ± 0.013	0.0034 ± 0.0009	14 ± 14
	1200 °C	10.1 ± 1.0	2.777 ± 0.006	0.0021 ± 0.0004	7 ± 5
	1100 °C	10.4 ± 0.5	2.765 ± 0.003	0.0025 ± 0.0002	6 ± 3
	1000 °C	9.1 ± 0.5	2.755 ± 0.003	0.0028 ± 0.0002	5 ± 3
	800 °C	7.3 ± 1.4	2.709 ± 0.012	0.0086 ± 0.0012	38 ± 17
	500 °C	6.4 ± 1.7	2.687 ± 0.017	0.0093 ± 0.0020	35 ± 31

CN = coordination number, MSRD = mean-square relative displacement, C_3 = third cumulant.

Figure 5.13 shows the CN (from EXAFS) as a function of NC size (from SAXS). For comparison, the size-dependent average CN for spherical FCC particles calculated from[40]

$$CN_{NC} = 12 \cdot (1 - 3R_{nn}/2D) \tag{5.1}$$

is also included, where R_{nn} is the nearest neighbor distance and D is the NC diameter. Experiment and theory agree well with the exception of the large NCs annealed in FG. For such samples, H chemisorption not only reduces the CN but, as shown in Fig. 5.14, also increases the MSRD (circled). Clearly H chemisorption induces considerable structural perturbations in the Pt NCs. The general increase in structural disorder with decreasing NC size apparent in Fig. 5.14 is the result of the greater fraction of (relaxed/reconstructed) surface atoms, mentioned above, and the associated broadening of the bond-length distribution.[13] Note the increase in MSRD is linear with inverse diameter or, equivalently, the surface-to-volume ratio.

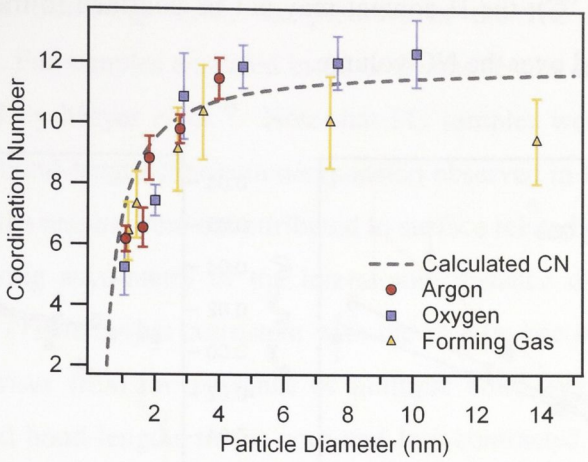

Fig. 5.13 – First NN shell coordination numbers (CN) determined by EXAFS analysis for Pt NC samples annealed in Ar, O_2 or FG as a function of mean NC diameter determined from SAXS analysis (symbols). The dashed line represents the values calculated for an FCC spherical particle.

The difference in Pt-Pt bond-length between the foil and NC samples, R_{bulk}-R_{NC}, is plotted in Fig. 5.14 as a function of the inverse diameter. For samples annealed in Ar or O_2, a bond-length contraction is observed, the magnitude of which increases as NC size decreases and is the result of capillary pressure.[41, 42] Using a simple liquid-drop model, as we previously demonstrated for Au[5] and Cu NCs,[43] the surface tension γ can be calculated from:[44]

$$R_{bulk} - R_{NC} = (-4/3)KR_{bulk}\gamma(1/D) \tag{5.2}$$

where K is the bulk compressibility. Using $K_{Pt} = 4.34\text{x}10^{-3}$ GPa^{-1},[45] yields $\gamma = 1.7 \pm 0.4$ and 2.2 ± 0.1 J/m^2 for annealing in Ar and O_2, respectively, similar to that reported for bulk Pt (2.6-3.5 J/m^2 [44]) but less than that determined from high energy electron diffraction of Pt NCs (3.7-10.6 nm) formed by vacuum evaporation on C grids (3.37-3.89 J/m^2).[44] Such differences may be influenced by the embedding matrix in the present case.

Annealing in FG yields a significantly greater value of surface tension (8.6 ± 0.5 J/m^2) and a bond-length expansion for the larger NCs where an appreciable H content was measurable with XANES. A bond-length expansion has also been reported in small Pt clusters subsequent to H chemisorption and attributed to a H-induced decrease in electron density between Pt atoms.[32, 46, 47] H atoms were bound to the Pt cluster surface for temperatures up to 500 °C.[32, 46, 47] For the much increased annealing temperatures

used herein (≤ 1300 °C), the H content may not be confined to the NC surface but is potentially distributed over the NC volume.

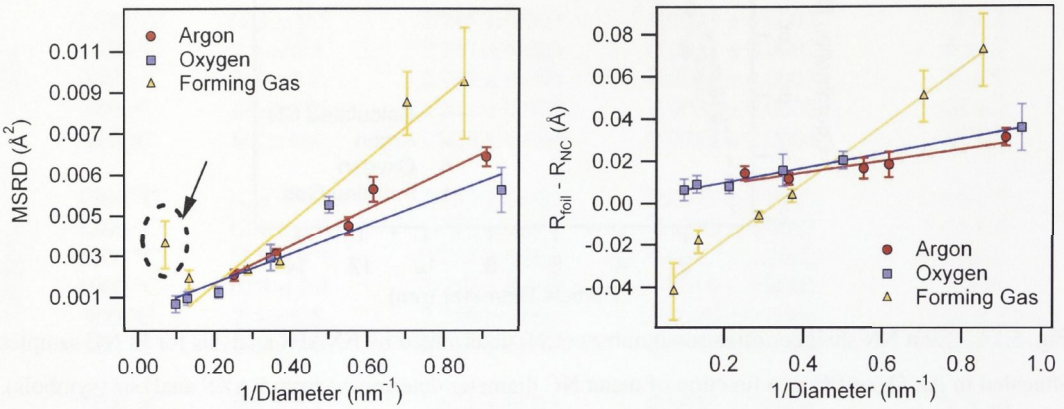

Fig. 5.14 – (left) MSRD as a function of the inverse NC diameter for samples annealed in Ar, O_2 or FG (symbols). (right) Difference between the bond-length of Pt foil and NCs, $R_{bulk} - R_{NC}$, as a function of the inverse NC diameter for samples annealed in Ar, O_2 or FG. In both graphs the solid lines are linear fits to the experimental values.

It is known that inside a sphere of diameter D acts a capillary pressure CP of magnitude:

$$CP = \frac{4\gamma}{D} \tag{5.3}$$

where γ is the average surface stress of the material.[48] Figure 5.15 shows the capillary pressure as a function of inverse NC diameter for Pt NCs annealed in Ar or O_2, with γ values calculated using Eq. 5.2

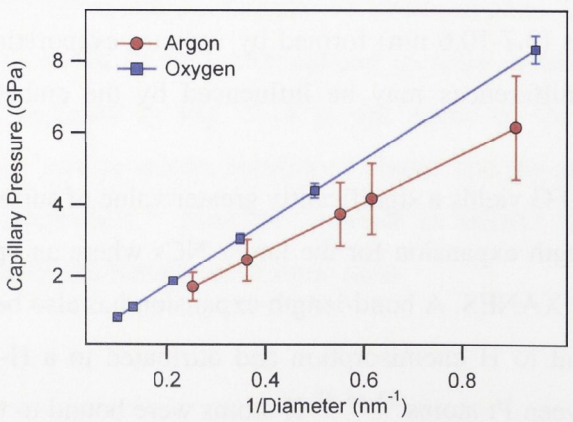

Fig. 5.15 – Capillary pressure as a function of inverse NC diameter.

As apparent from Fig. 5.15, the pressure in the NC core increases with decreasing NC size. For samples annealed in Ar or O_2, the results are in good agreement with those reported by Meyer *et al.*[48] Note that FG samples were not included here given the non-zero bond-length contraction/expansion observed in large NCs (Fig. 5.14) and, consequently, the results were not attributed to surface related effects only.

The decreasing asymmetry of the interatomic distance distribution (C_3) with increasing NC size (Table 5.4) is consistent with the Pt NCs becoming more bulk like. Such asymmetry arises from the presence of multiple bond-lengths within the NCs, including contracted bond-lengths in the core and less contracted (possibly expanded) bond-lengths at the surface. The former is a result of capillary pressure (Fig. 5.15), while the latter results from the relaxation of surface atoms. The greatest asymmetry was observed for the smallest NCs, which also exhibited the shortest average bond-lengths, suggesting the bond-length relaxation of surface atoms must be small compared to the contraction of the core atoms. The smaller the NC, the greater the surface-to-volume ratio and the greater the capillary pressure. The overall effect is an average bond-length contraction and positive C_3 that increases with decreasing NC size.

5.4 – Temperature-dependent EXAFS

The use of EXAFS as a probe of vibrational and thermal properties has been under constant development as evident in the representative works comprising references[3, 49-61]. Recently, Fornasini and co-workers[49, 50] have highlighted the differences between parameters measured by EXAFS and x-ray diffraction. From temperature-dependent EXAFS measurements, one can obtain information on the variation of the mean value (interatomic distance), variance (MSRD) and asymmetry (C_3) of the first-shell interatomic distance distribution over the given temperature range. The Einstein temperature, the thermal and structural contributions to total disorder, the anharmonicity of the effective pair potential and the linear thermal expansion coefficient can all be extracted from the experimental data via the appropriate combination of a correlated Debye or Einstein model and thermodynamic perturbation theory.[49-52] It has been previously demonstrated that this approach can be readily extended to the study of embedded metal and semiconductor NCs [3, 61] and here we have

applied this method to Pt NCs produced by ion implantation in a-SiO_2 to study their vibrational and thermal properties as a function of NC size.

Temperature-dependent EXAFS measurements were performed in samples implanted with Pt ions to a total fluence of $1x10^{17}$ cm^{-2} and subsequently annealed in Ar or FG for one hour at 1000-1200 °C. Samples were measured at a minimum of eight temperatures and analyzed according to the procedure described in Chapter IV. Representative spectra are shown in Fig. 5.16 within which scattering from the first four nearest neighbours (NN) shells is apparent. Clearly the amplitude decreases as the measurement temperature increases or, equivalently, as thermal disorder becomes more significant. Comparing NC and bulk sample spectra at a given measurement temperature, the decreased amplitude of the former is the result of finite-size effects, specifically the reduced average CN and enhanced structural disorder associated with the non-negligible surface-to-volume ratio in the NCs.

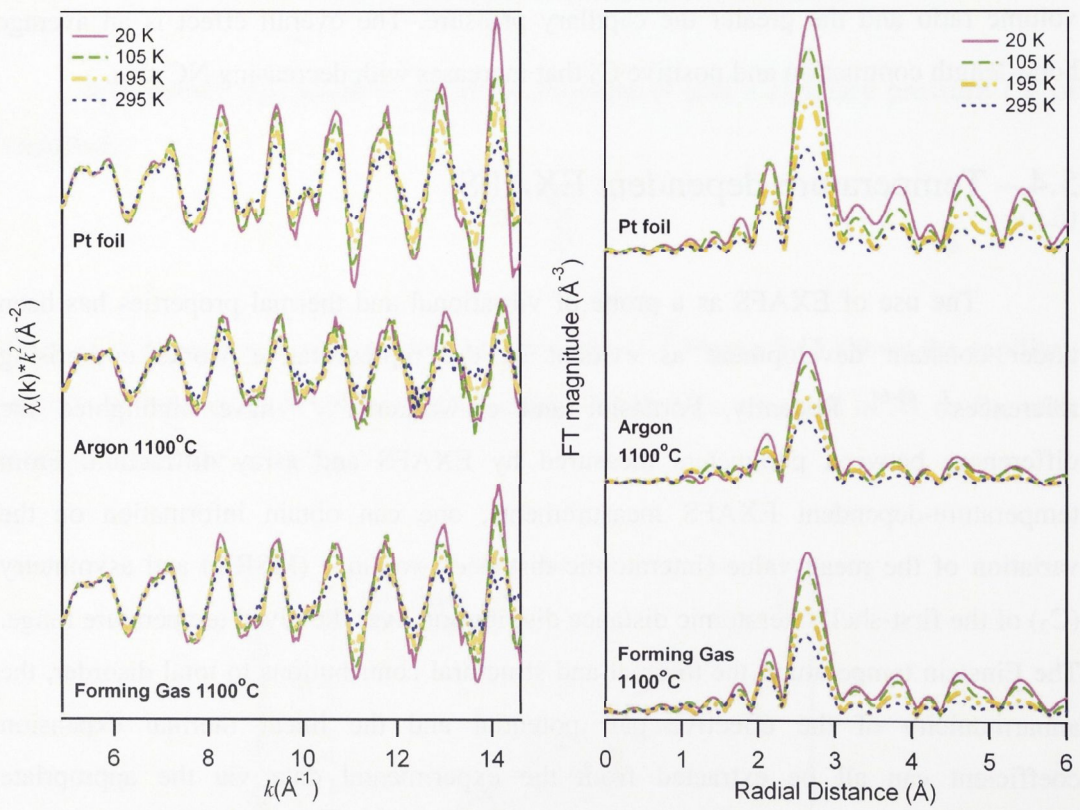

Fig. 5.16 – (left) k^2-weighted and (right) Fourier-transformed (non-phase-corrected) EXAFS spectra. Measurement temperatures are specified in the legend.

5.4.1 – MSRD and Einstein temperatures

The general increase in MSRD with increasing measurement temperature is readily apparent in Fig. 5.18 for all samples and, as before, is the result of increasing thermal disorder. Fitting with Eq. (4.5) enables us to separate the structural and thermal contributions to the total disorder and determine the Einstein temperature. Values are listed in Table 5.5 as a function of annealing temperature, annealing ambient and mean NC diameter. For the Pt foil, our results agree well with those of Kang *et al.* [62]. For the Pt NCs, Fig. 5.19(a) demonstrates that structural disorder increases with a decrease in NC size or increase in surface-to-volume ratio as the relaxation of under-coordinated surface atoms results in a wider distribution of interatomic distances, consistent with the results shown in Fig. 5.14.[13, 63, 64] Similar values have been reported for Pt [13, 62, 63, 65] and other metallic NCs.[49, 55, 66] Note that samples annealed in FG at 1200 °C (7.4 nm) exhibit greater structural disorder due to H chemisorption as outlined earlier.[64]

Table 5.5 – Values of mean NC diameter (D_{mean}) estimated from SAXS measurements, the structural contribution to total disorder (σ^2_{static}), the Einstein temperature (Θ_E) and the thermal expansion of interatomic distances (ΔR) between 20 and 295 K obtained from EXAFS analysis.

Sample		D_{mean} (nm)	σ^2_{static} (Å^2)	Θ_E (K)	ΔR (Å)
Pt foil		-	0.0003 ± 0.0001	179 ± 2	0.014 ± 0.001
Ar	1200 °C	4.0 ± 0.6	0.0007 ± 0.0001	178 ± 2	0.013 ± 0.001
	1100 °C	2.8 ± 0.4	0.0019 ± 0.0001	177 ± 3	0.006 ± 0.001
	1000 °C	1.8 ± 0.2	0.0031 ± 0.0001	194 ± 5	0.005 ± 0.001
FG	1200 °C	7.4 ± 1.3	0.0012 ± 0.0001	178 ± 2	0.016 ± 0.002
	1100 °C	3.5 ± 0.5	0.0013 ± 0.0001	182 ± 1	0.010 ± 0.001
	1000 °C	2.7 ± 0.4	0.0015 ± 0.0001	183 ± 1	0.006 ± 0.001

With reference to Table 5.5, the Einstein temperature of the smaller NCs (< 3 nm) increases relative to that of the Pt foil indicative of stiffer bonding. Higher Θ_E values have also been reported for free-standing and/or functionalised Pt NCs of comparable size.[13, 62, 65] The larger Pt NCs (including those with chemisorbed H) rapidly converge to bulk-like values again consistent with previous observations for free-standing Pt NCs.[13] Neither the a-SiO_2 matrix nor chemisorbed H significantly

influence the Einstein temperature of the Pt NCs examined here. The higher Θ_E values observed for the smaller NCs are due to capillary pressure which shifts the vibrational density of states (VDOS) upwards [48, 67] (as shown in Fig. 5.17 for Cu[48]) and, as described previously, reduces the interatomic distance.

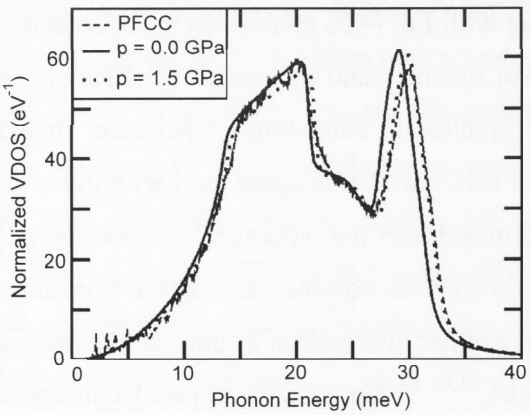

Fig. 5.17 – Normalized VDOS of crystalline fcc Cu under pressures of 0 and 1.5 GPa and the contribution of the core atoms in a cluster with 791 atoms (PFCC). Figure extracted from Meyer *et al.*[48]

Capillary pressure is the result of surface curvature and, according to the Kelvin equation, varies inversely with NC diameter,[48, 67] as shown in Fig. 5.15. Figure 5.19(b) shows that Θ_E scales with inverse NC diameter and thus capillary pressure. Reports for other metal NCs (~3 nm) embedded in a-SiO_2 indicate the Einstein temperature may be either lower (Cu [61] and Sn [68]) or similar (Au [61]) to that of bulk standards. The former was attributed to loosely-bound surface/interfacial atoms shifting the VDOS downwards to a greater extent than the counter balancing effect of capillary pressure. Clearly an intricate interplay between finite-size effects (capillary pressure and surface disorder), surface functionalisation (including H chemisorption) and the embedding matrix must govern the vibrational properties of NCs. From the results presented here, we conclude that finite-size effects, specifically capillary pressure, are the dominant influence for Pt NCs.

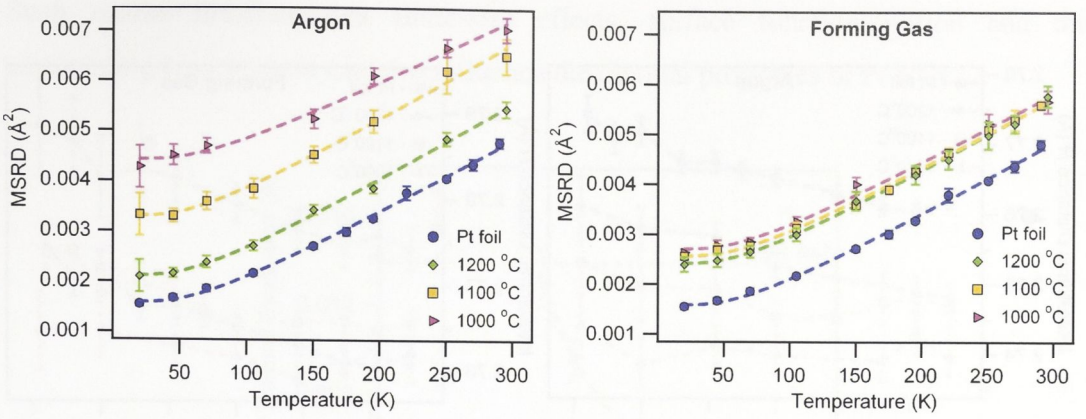

Fig. 5.18 – MSRD as a function of measurement temperature. Dashed lines are fits to the experimental values using Eq.(4.5).

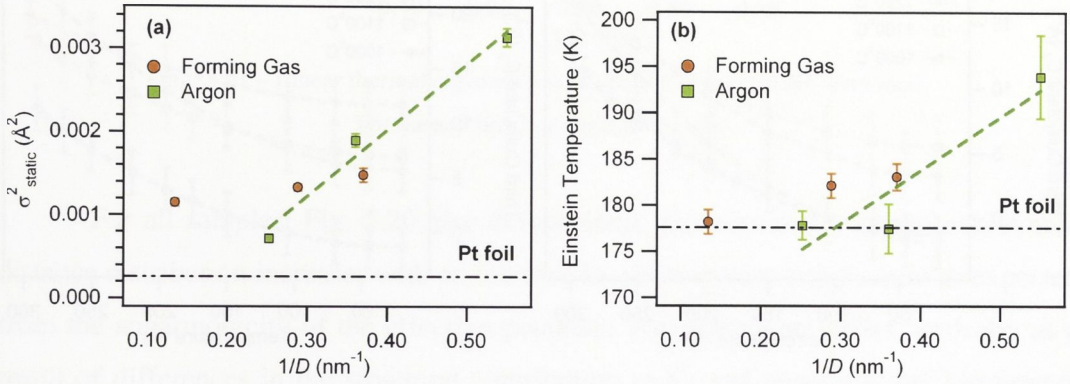

Fig. 5.19 – (a) Structural contribution to the MSRD as a function of inverse NC diameter. (b) Einstein temperature as a function of inverse NC diameter.

5.4.2 – Bond-lengths and third cumulants

Values for R and C_3 are plotted in Fig. 5.20 as a function of the measurement temperature. The pressure exerted on the NC core as a result of surface curvature yields, in general, a reduced interatomic distance relative to that of the Pt foil, consistent with previous reports for other metals.[13, 63, 66] As the NCs increase in size, the capillary pressure decreases in magnitude and, accordingly, R approaches the bulk value. Samples with chemisorbed H (those annealed in FG at 1100 and 1200 °C) remain the exception with R values comparable to or greater than the bulk value. This difference increases as a function of H content or, equivalently, the annealing temperature in FG.

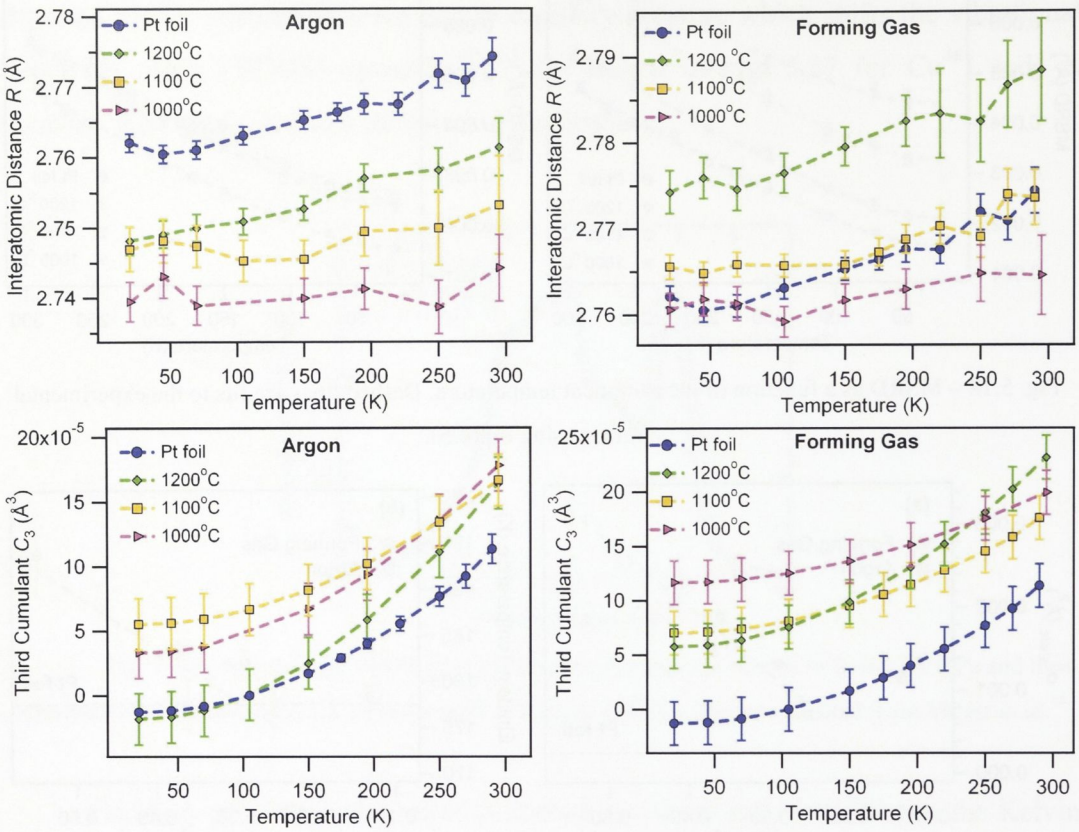

Fig. 5.20 – Interatomic distance R (top) and asymmetry C_3 (bottom) as a function of measurement temperature.

From Fig. 5.20, the interatomic distances clearly increase with measurement temperature. The linear thermal expansion ($\Delta R = R_{295K} - R_{20K}$) is presented in Fig. 5.21 as a function of inverse NC diameter, with values listed in Table 5.5. Excluding the sample with appreciable chemisorbed H, NCs exhibit less thermal expansion than the Pt foil and the difference becomes more pronounced as the NC size decreases. Comparing our results with those for free-standing Pt NCs[13] (where NC > 2.4 nm show positive thermal expansion similar to that of the bulk), the a-SiO_2 matrix appears to restrict the thermal expansion of embedded Pt NCs consistent with the negative thermal expansion coefficient of a-SiO_2 below 180 K and a very low yet positive coefficient above this temperature.[69, 70] Similar results have been reported for Ge NCs.[71] Other reports include nil thermal expansion for functionalized Pt NCs[65] and an unusual negative thermal expansion for Pt NCs supported on Al_2O_3,[62] the latter attributed to Pt-Al_2O_3 interaction.

Such results illustrate that finite-size effects, surface functionalisation and the surrounding environment can also influence the thermal properties of Pt NCs.

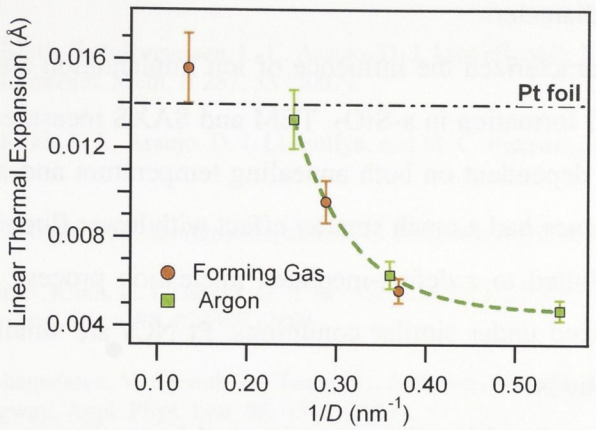

Fig. 5.21 – Linear thermal expansion as a function of inverse NC diameter. The dashed line is a guide to the eye.

For all samples, Fig. 5.20 also demonstrates the asymmetry of the interatomic distance distribution increases with an increase in measurement temperature as expected from the anharmonicity of the effective potential. The spectra are offset vertically as a result of differences in the structural contribution to C_3 and generally this component increases with a decrease in NC size in good agreement with results for supported Pt NCs.[63]

5.6 – Conclusions

In summary, we have investigated the formation, structural and thermal properties of Pt NCs formed in a-SiO_2 by ion implantation and thermal annealing. The nucleation behavior was studied by irradiating a-SiO_2 with Ge ions prior to Pt implantation. Without ion irradiation, the largest Pt NCs (~5.5 nm) were formed at depths where the irradiation-induced vacancy production was minimal, in contrast to other metals. With ion irradiation prior to NC formation, the mean Pt NC diameter decreased as the irradiation fluence increased. Saturation of the NC diameter at ~3 nm was observed when the energy deposited in vacancy production reached ~2×10^{23} keV/cm^3. We suggest Pt NCs readily nucleated on irradiation-induced disorder, the nature of which was not identified but was unlikely to be a single defect configuration.

High-energy ion irradiation of SiO_2 prior to Pt NC formation, producing a near-constant concentration of irradiation-induced vacancies over the extent of the SiO_2 layer, yielded a more uniform Pt NC size distribution and thus represents an effective means of tailoring the Pt NC diameter.

We have characterized the influence of ion implantation and thermal annealing conditions on Pt NC formation in a-SiO_2. TEM and SAXS measurements demonstrated NC size is strongly dependent on both annealing temperature and ambient. In contrast, the implantation fluence had a much smaller effect with lower fluences actually yielding larger sizes as attributed to a defect-mediated nucleation process. Compared to other metallic NCs produced under similar conditions, Pt NCs are smaller and exhibit very narrow size distributions.

Size dependent bond-length contraction and increasing structural disorder were observed, attributed to finite size effects and increasing capillary pressure with decreasing NC size.

XANES measurements demonstrated the presence of Pt-H bonding in NCs annealed in FG at high temperatures. In large NCs (> 3.0 nm), H chemisorption induced a bond-length expansion, a decrease in Pt coordination number and an increase in structural disorder as apparent from EXAFS measurements. The surface tension for such hydrogenated Pt NCs was strikingly different from that of bulk material and NCs annealed in Ar or O_2. Clearly H chemisorption yields significant structural perturbations in Pt NCs.

The vibrational and thermal properties of Pt NCs embedded in a-SiO_2 have been characterized using temperature-dependent EXAFS analysis. The interatomic distance, structural and thermal disorder and asymmetry have been determined as a function of measurement temperature and NC size. Relative to bulk values, the structural disorder and mean vibrational frequency increased as the NC diameter decreased. Pt NCs thus exhibit stiffer bonding compared to their bulk counterparts. The vibrational properties of embedded Pt NCs are not significantly influenced by the a-SiO_2 matrix or H chemisorption. The constraint imposed by the matrix can, however, reduce the thermal expansion of embedded Pt NCs.

References

[1] R. Giulian, P. Kluth, B. Johannessen, L. L. Araujo, D. J. Llewellyn, D. J. Cookson, and M. C. Ridgway, Nucl. Instrum. Meth. B **257**, 33 (2007).

[2] R. Giulian, P. Kluth, L. L. Araujo, D. J. Llewellyn, and M. C. Ridgway, Appl. Phys. Lett. **91**, 093115 (2007).

[3] L. L. Araujo, P. Kluth, G. d. M. Azevedo, and M. C. Ridgway, Phys. Rev. B **74**, 184102 (2006).

[4] B. Johannessen, P. Kluth, C. J. Glover, G. d. M. Azevedo, D. J. Llewellyn, G. J. Foran, and M. C. Ridgway, J. Appl. Phys. **98**, 024307 (2005).

[5] P. Kluth, B. Johannessen, V. Giraud, A. Cheung, C. J. Glover, G. d. M. Azevedo, G. J. Foran, and M. C. Ridgway, Appl. Phys. Lett. **85**, 3561 (2004).

[6] A. Meldrum, L. A. Boatner, and C. W. White, Nucl. Instr. and Meth. B **178**, 7 (2001).

[7] K. H. Heinig, T. Muller, B. Schmidt, M. Strobel, and W. Moller, Appl. Phys. A **77**, 17 (2003).

[8] P. Kluth, B. Johannessen, G. J. Foran, D. J. Cookson, S. M. Kluth, and M. C. Ridgway, Phys. Rev. B **74**, 014202 (2006).

[9] G. Rizza, H. Cheverry, T. Gacoin, A. Lamasson, and S. Henry, J. Appl. Phys. **101**, 014321 (2007).

[10] M. A. El-Sayed, Accounts Chem. Res. **34**, 257 (2001).

[11] A. T. Bell, Science **299**, 1688 (2003).

[12] M. E. Akerman, W. C. W. Chan, P. Laakkonen, S. N. Bhatia, and E. Ruoslahti, P. Natl. Acad. Sci. USA **99**, 12617 (2002).

[13] A. I. Frenkel, C. W. Hills, and R. G. Nuzzo, J. Phys. Chem. B **105**, 12689 (2001).

[14] X. Zhong, Y. Feng, I. Lieberwirth, and W. Knoll, Chem. Mater. **18**, 2468 (2006).

[15] J. F. Ziegler, J. P. Biersack, and U. Littmark, *The Stopping and Range of Ions in Solids* (Pergamon Press, New York, 1985).

[16] www.srim.org.

[17] S. Klaumunzer, Nucl. Instr. and Meth. B **225**, 136 (2004).

[18] E. Valentin, H. Bernas, C. Ricolleau, and F. Creuzet, Phys. Rev. Lett. **86**, 99 (2001).

[19] P. Kluth, B. Johannessen, D. J. Cookson, G. J. Foran, and M. C. Ridgway, Nucl. Instrum. Meth. B **246**, 30 (2006).

[20] C. M. Johnson, M. C. Ridgway, and P. W. Leech, Appl. Phys. Lett. **69**, 984 (1996).

[21] R. A. B. Devine, Nucl. Instr. and Meth. B **91**, 378 (1994).

[22] S. L. Ellingboe and M. C. Ridgway, Nucl. Instr. and Meth. B **127**, 90 (1997).

[23] H. Borchert, V. Shevchenko, A. Robert, I. Mekis, A. Kornowski, G. Grubel, and H. Weller, Langmuir **21**, 1931 (2005).

[24] L. G. Jacobsohn, J. D. Thompson, A. Misra, R. K. Schulze, M. F. Hundley, and M. Nastasi, J. Appl. Phys. **99**, 104307 (2006).

[25] A. Miotello, G. De Marchi, G. Mattei, P. Mazzoldi, and C. Sada, Phys. Rev. B **63**, 075409 (2001).

[26] H. Dallaporta, M. Liehr, and J. E. Lewis, Phys. Rev. B **41**, 5075 (1990).

[27] J. D. McBrayer, R. M. Swanson, and T. W. Sigmon, J. Electrochem. Soc. **133**, 1242 (1986).

[28] A. Meldrum, R. F. Haglund, L. A. Boatner, and C. W. White, Adv. Mater. **13**, 1431 (2001).

[29] A. K. Shukla, R. K. Raman, N. A. Choudhury, K. R. Priolkar, P. R. Sarode, S. Emura, and R. Kumashiro, J. Electroanal. Chem. **563**, 181 (2004).

[30] M. Fernandez-Garcia, Catal. Rev. **44**, 59 (2002).

[31] B. Hammer and J. K. Norskov, Nature **376**, 238 (1995).

[32] M. K. Oudenhuijzen, J. A. van Bokhoven, J. T. Miller, D. E. Ramaker, and D. C. Koningsberger, J. Am Chem. Soc. **127**, 1530 (2005).

[33] E. Bus and J. A. vanBokhoven, J. Phys. Chem. C **111**, 9761 (2007).

[34] A. Y. Stakheev, Y. Zhang, A. V. Ivanov, G. N. Baeva, D. E. Ramaker, and D. C. Koningsberger, J. Phys. Chem. C **111**, 3938 (2007).

[35] K. L. Brower, Phys. Rev. B **38**, 9657 (1988).

[36] I. A. Shkrob, B. M. Tadjikov, S. D. Chemerisov, and A. D. Trifunac, J. Chem. Phys. **111**, 5124 (1999).

[37] T. Kubota, K. Asakura, N. Ichikuni, and Y. Iwasawa, Chem. Phys. Lett. **256**, 445 (1996).

[38] K. Asakura, T. Kubota, W.-J. Chun, Y. Iwasawa, K. Ohtani, and T. Fujikawa, J. Synchrotron Rad. **6**, 439 (1999).

[39] C. Q. Sun, Prog. Solid State Chem. **35**, 1 (2007).

[40] S. Depanfilis, F. Dacapito, V. Haas, H. Konrad, J. Weissmuller, and F. Boscherini, Phys. Lett. A **207**, 397 (1995).

[41] J. S. Vermaak, C. W. Mays, and D. Kuhlmann, Surf. Sci. **12**, 128 (1968).

[42] C. W. Mays, J. S. Vermaak, and D. Kuhlmann, Surf. Sci. **12**, 134 (1968).

[43] B. Johannessen, P. Kluth, D. J. Cookson, G. J. Foran, and M. C. Ridgway, Nucl. Instrum. Meth. B **246**, 45 (2006).

[44] C. Solliard and M. Flueli, Surf. Sci. **156**, 487 (1985).

[45] www.webelements.com.

[46] E. Bus and J. A. van Bokhoven, Phys. Chem. Chem. Phys. **9**, 2894 (2007).

[47] M. K. Oudenhuijzen, J. H. Bitter, and D. C. Koningsberger, J. Phys. Chem. B **105**, 4616 (2001).

[48] R. Meyer, L. J. Lewis, S. Prakash, and P. Entel, Phys. Rev. B **68** (2003).

[49] P. Fornasini, S. A. Beccara, G. Dalba, R. Grisenti, A. Sanson, M. Vaccari, and F. Rocca, Phys. Rev. B **70** (2004).

[50] P. Fornasini, AIP Conf. Proc. **882**, 94 (2007).

[51] L. Troger, T. Yokoyama, D. Arvanitis, T. Lederer, M. Tischer, and K. Baberschke, Phys. Rev. B **49**, 888 (1994).

[52] A. I. Frenkel and J. J. Rehr, Phys. Rev. B **48**, 585 (1993).

[53] G. Dalba, P. Fornasini, R. Grisenti, and J. Purans, Phys. Rev. Lett. **82**, 4240 (1999).

[54] G. S. Knapp, H. K. Pan, and J. M. Tranquada, Phys. Rev. B **32**, 2006 (1985).

[55] B. Gilbert, F. Huang, H. Z. Zhang, G. A. Waychunas, and J. F. Banfield, Science **305**, 651 (2004).

[56] N. Van Hung, N. B. Duc, and R. R. Frahm, J. Phys. Soc. Jpn. **72**, 1254 (2003).

[57] M. Vaccari and P. Fornasini, J. Synchrot. Radiat. **13**, 321 (2006).

[58] J. J. Rehr and R. C. Albers, Rev. Mod. Phys. **72**, 621 (2000).

[59] E. Sevillano, H. Meuth, and J. J. Rehr, Phys. Rev. B **20**, 4908 (1979).

[60] E. A. Stern, B. A. Bunker, and S. M. Heald, Phys. Rev. B **21**, 5521 (1980).

[61] P. Kluth, B. Johannessen, L. L. Araujo, and M. C. Ridgway, AIP Conf. Proc. **882**, 731 (2007).

[62] J. H. Kang, L. D. Menard, R. G. Nuzzo, and A. I. Frenkel, J. Am Chem. Soc. **128**, 12068 (2006).

[63] A. Witkowska, A. Di Cicco, and E. Principi, Phys. Rev. B **76**, 104110 (2007).

[64] R. Giulian, L. L. Araujo, P. Kluth, D. J. Sprouster, C. S. Schnohr, B. Johannessen, G. J. Foran, and M. C. Ridgway, J. Appl. Phys. **105**, 044303 (2009).

[65] L. J. Giovanetti, J. M. Ramallo-Lopez, F. G. Requejo, D. I. Garcia-Gutierrez, M. Jose-Yacaman, and A. F. Craievich, J. Phys. Chem. C **111**, 7599 (2007).

[66] B. Johannessen, P. Kluth, R. Giulian, L. L. Araujo, D. J. Llewellyn, G. J. Foran, D. J. Cookson, and M. C. Ridgway, Nucl. Instrum. Meth. B **257**, 37 (2007).

[67] R. Meyer, S. Prakash, and P. Entel, Phase Transitions **75**, 51 (2002).

[68] G. E. J. Koops, H. Pattyn, A. Vantomme, S. Nauwelaerts, and R. Venegas, Phys. Rev. B **70**, 235410 (2004).

[69] G. K. White, J. Phys. D-Appl. Phys. **6**, 2070 (1973).

[70] P. H. Gaskell, Trans. Faraday Soc. **62**, 1505 (1966).

[71] L. L. Araujo, R. Giulian, D. J. Sprouster, C. S. Schnohr, D. J. Llewellyn, P. Kluth, D. J. Cookson, G. J. Foran, and M. C. Ridgway, Phys. Rev. B **78**, 094112 (2008).

CHAPTER VI

SWIFT HEAVY ION IRRADIATION OF PLATINUM NANOCRYSTALS

This chapter reports on the swift heavy ion irradiation of Pt NCs. Transmission electron microscopy, small-angle x-ray scattering and x-ray absorption fine structure (near-edge and extended regions) were used to investigate the changes in NC shape, size and structure, as well as the changes in H content induced by swift heavy ion irradiation.

6.1 – Introduction

The understanding of NC properties as well as the ability to control parameters like size, shape and structure are essential for the development of novel functional materials and devices.[1] As demonstrated in the previous chapter, parameters like bond-length, coordination number (CN) and atomic disorder are size dependent and can differ significantly from bulk values. Furthermore, NC properties are also influenced by their shape. Examples include linearly polarized emission of semiconductor quantum rods,[2, 3] anisotropic magnetic properties of elongated Co NCs[4] and enhanced catalytic activities of non-spherical Pt NCs.[5] We are able to tailor the size distribution of spherical NCs using ion irradiation prior[6] or subsequent[7, 8] to NC formation along with varying the implanted atom concentration and annealing conditions.[9]

Swift heavy ion irradiation (SHII) is an important tool in the modification of materials.[10-13] In the energy regime above tens of MeV, the ion-matter interaction is dominated by electronic energy loss with the energy locally deposited along the ion path.[14] Effects that arise from this form of interaction include the deformation of metallic and semiconductor NCs. Interestingly, the deformation of semiconductor NCs yields elongation perpendicular to the incident ion beam direction,[15-18] while metallic NCs elongate parallel to the beam direction.[4, 19-23] This intriguing behavior of metallic NCs under SHII may yield applications in advanced devices given NC magnetic[4] and optical[2] properties strongly depend on orientation. D'Orleans *et al.*[4] suggested NC melting combined with creep deformation drives the elongation process though Klaumunzer[13] pointed out the limitations of such a model. A thorough understanding of the deformation process is still lacking and only scant and sometimes contradicting results (like the deformation of Ag NCs under SHII, which was reported by Oliver *et al.*[21] but not observed by Penninkhof *et al.*[20]) have been presented thus far.

This chapter reports on the effects of SHII of Pt NCs formed by ion implantation in amorphous SiO_2 (a-SiO_2). The deformation process was studied as a function of NC size, irradiation fluence and energy to give a broad perspective of the shape transformation. It also includes the effects of SHII on the H desorption and structural properties of embedded Pt NCs. X-ray absorption fine structure (near edge (XANES) and extended (EXAFS) regions), as well as small-angle x-ray scattering (SAXS) and

transmission electron microscopy (TEM) analyses were used to investigate parameters like NC size, shape, CN, bond-length, mean-square relative displacement (MSRD), as well as NC dissolution and H desorption. The Pt-H bonding, previously identified in samples annealed in forming gas (FG) at temperatures above 1000 °C,[24] diminished upon SHII, resulting in dramatic changes in the NC structural parameters.

6.2 – Experimental

Pt NC-containing samples were prepared by ion implantation and thermal annealing as described in Chapter V. Unless otherwise stated, the samples were annealed in FG. Subsequently, the samples were irradiated with 27, 55, 89 or 185 MeV Au ions at room temperature with fluences varying from $1x10^{12}$-$1x10^{15}$ cm^{-2}. The electronic energy loss was near constant over the depth of the SiO_2 layer and of approximate value 4, 8, 12 and 17 keV/nm, respectively. The nuclear energy loss was significantly lower than the electronic,[25] as shown in Fig.2.1, and was thus considered negligible.

TEM, SAXS and XAFS measurements were used to evaluate the shape, size and structure (including H desorption) evolution of the Pt NCs as a function of irradiation fluence. The sample preparation and data analysis methods are those described in Chapter IV.

6.3 – NC shape transformation

Figure 6.1 shows TEM micrographs of Pt NCs irradiated with 185 MeV Au ions. The left panels show the evolution of the NC shape and size as a function of irradiation fluence. Prior to irradiation, the NCs are of diameter 14.5 nm (with standard deviation of 1.8 nm (Table 6.1)) and, as shown in the inset on the right panel of Fig. 6.1, are spherical and single crystalline. Upon irradiation, the NCs elongate in the direction parallel to the incident ion beam with increasing aspect ratio for fluences $\leq 2x10^{14}$ cm^{-2}. They exhibit polycrystalline morphology, as apparent from the high resolution TEM image shown on the right panel of Fig. 6.1. For SHII fluences above $2x10^{14}$ cm^{-2}, the aspect ratio decreases due to dissolution and fragmentation via Rayleigh instability,[26] the latter similar to that observed for annealed nanowires.[27] Fragmentation can be

observed in the bottom panel of Fig. 6.1, which shows elongated Pt NCs irradiated with $4x10^{14}$ cm^{-2}. Surrounding the elongated NCs are very small Pt clusters < 1 nm in diameter resulting from NC dissolution. Their small size was below the minimum required for quantitative TEM and SAXS analysis.

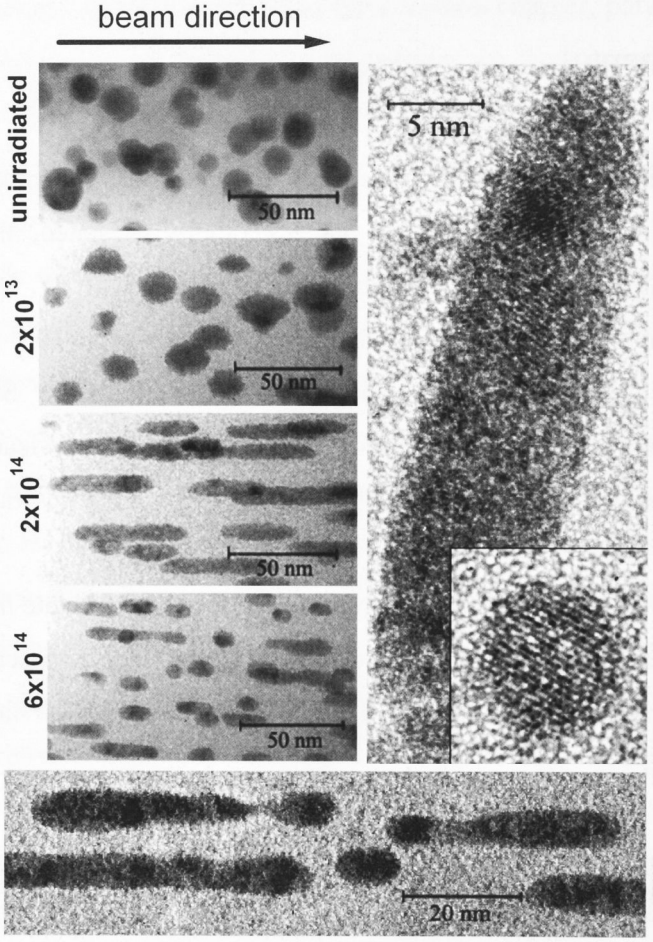

Fig. 6.1 – (left) TEM micrographs of Pt NCs (mean diameter 14.5 nm prior to SHII) irradiated with 185 MeV Au ions at fluences indicated on the panels. (right) High resolution images of elongated and spherical Pt NCs. (bottom) Magnified view of Pt NCs irradiated with $4x10^{14}$ cm^{-2}.

The evolution of the NC dimensions under SHII is demonstrated in Fig. 6.2 which shows the minor dimension (D_{minor}) as a function of the major dimension (D_{major}) measured from TEM micrographs (each point represents the mean value of D_{minor} for a given D_{major} ± 1 nm). Elongation is only observed for NCs exceeding a threshold diameter of ~6.5 nm for irradiation at 185 MeV. NCs larger than the threshold diameter elongate until D_{minor} saturates at this same threshold value, yielding a very narrow

distribution for D_{minor}. Simultaneously, D_{major} increases significantly for SHII fluences $\leq 2x10^{14}$ cm^{-2} yielding aspect ratios as great as 10 (not apparent from Fig. 6.2). For higher fluences, despite dissolution and fragmentation, D_{minor} remains unchanged.

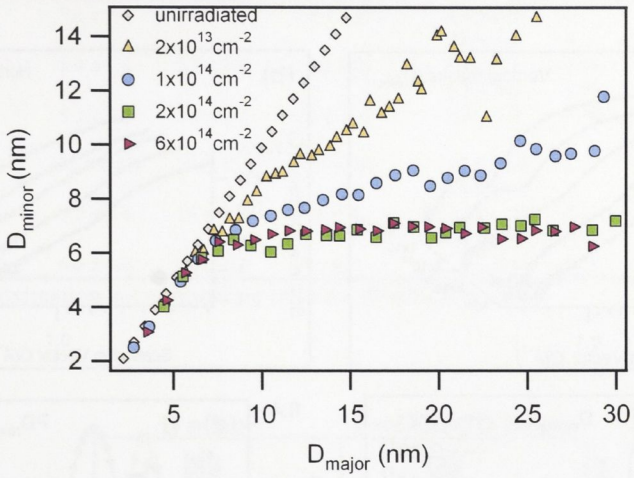

Fig. 6.2 – NC D_{major} versus D_{minor} according to SHII fluence (185 MeV irradiations), as determined from TEM.

Figure 6.3 shows SAXS scattering intensities as a function of Q following 185 MeV Au ion irradiation. Scattering from the area within the vertical mask is plotted in Fig. 6.3(a), which originates from D_{minor} while scattering from the region encompassed by the horizontal mask is plotted in Fig. 6.3(b), corresponding to PD_{major} at 45°. The associated dimension distributions are plotted in Fig. 6.3(c) and (d), which show the evolution of D_{minor} and PD_{major} as a function of SHII fluence. The elongation of the NCs upon irradiation broadens the PD_{major} distribution (Fig. 6.3(d)). At the same time, the reduction of D_{minor} is accompanied by a narrowing of the D_{minor} distribution (Fig. 6.3(c)). The mean dimensions obtained from TEM and SAXS analysis of NCs irradiated with 185 MeV Au ions at different fluences, as well as the standard deviation of the distributions (when applicable) and the intensity correction calculated using Eq. (4.2) are presented in Table 6.1 for two NC sizes (8.4 and 14.5 nm prior to SHII). The values listed for the mean dimensions stem from the statistical average of the experimental data, not necessarily coinciding with the peak of the distributions. When the distributions could be approximated by a Gaussian, the standard deviations are also included. Note that for both size distributions, the mean NC diameter prior to SHII exceeded the threshold for elongation and, within experimental error, a common

saturation value for D_{minor} was observed upon SHII. These results agree well with TEM analysis as shown in Fig. 6.4, validating our approach used in the SAXS analysis of the rod-like NCs. The TEM distributions (D_{minor} and D_{major}) were corrected using Eq. (4.1) to enable comparison with the SAXS results.

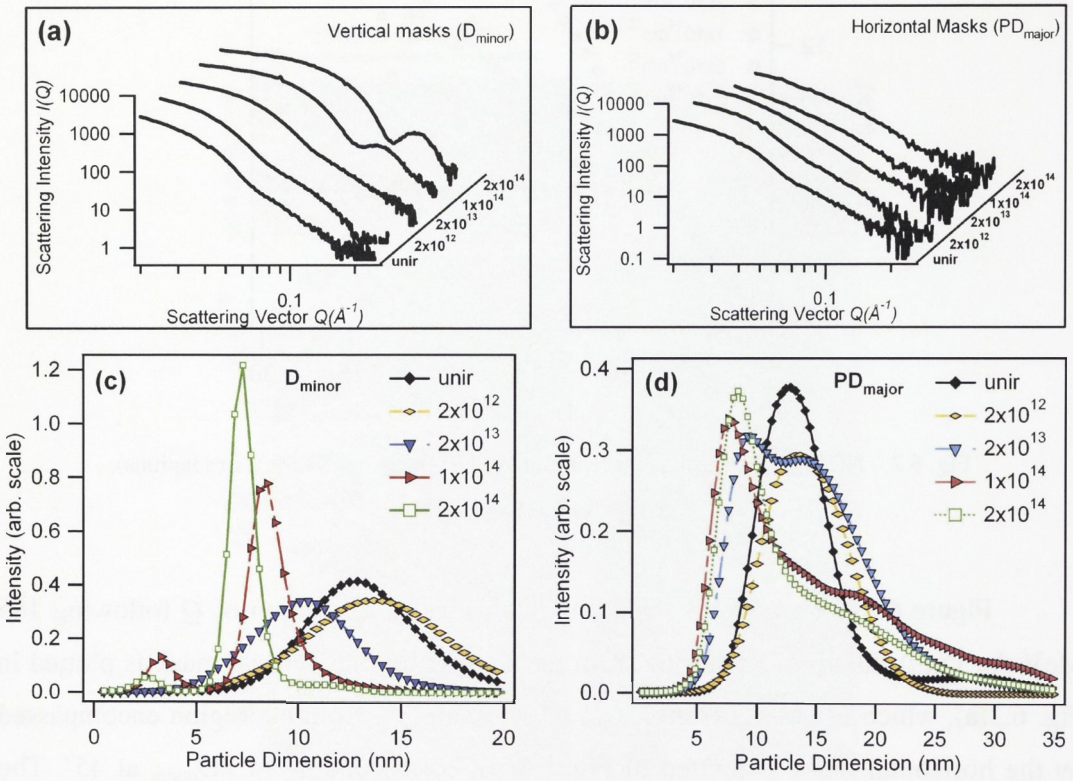

Fig. 6.3 - Scattering intensity $I(Q)$ as a function of the scattering vector Q for Pt NCs with mean diameter 14.5 nm (prior to SHII) irradiated with 185 MeV Au ions at different fluences. Panel (a) shows the scattering integrated from the vertical masks and panel (b) from the horizontal masks, with the respective distributions shown in panel (c) and (d), which correspond to the NCs D_{minor} and PD_{major} at 45° sample tilt, respectively.

Table 6.1 – D_{minor} , D_{major} and PD_{major} (45°) estimated from TEM. D_{minor}, PD_{major} and respective intensity corrections as a function of SHII fluence estimated from SAXS. σ is the standard deviation of the distributions.

	SHII fluence	TEM (nm)			SAXS (nm)			
	(cm^{-2}) 185 MeV	$D_{minor} \pm \sigma$	$D_{major} \pm \sigma$	$PD_{major} \pm \sigma$	$D_{minor} \pm \sigma$	IC_{minor}	$PD_{major} \pm \sigma$	IC_{major}
3 at. % 1200 °C	unirradiated	7.8 ± 1.4	7.8 ± 1.4	7.8 ± 1.4	8.4 ± 0.9	1	8.5 ± 0.8	1
	$2x10^{12}$	-	-	-	7.6 ± 1.3	1	7.7 ± 1.1	1
	$2x10^{13}$	5.4 ± 1.8	6.2 ± 1.6	5.8 ± 1.2	6.8 ± 1.4	0.93	7.0 ± 0.9	1.04
	$1x10^{14}$	-	-	-	6.5 ± 1.0	0.81	6.9 ± 0.8	1.13
	$2x10^{14}$	5.2 ± 1.8	7.4 ± 1.8	6.5 ± 1.3	6.4 ± 1.0	0.79	6.8 ± 1.0	1.15
3 at.% 1300 °C	unirradiated	13.0 ± 3.4	13.0 ± 3.4	13.0 ± 3.4	14.5 ± 1.8	1	14.4 ± 1.9	1
	$2x10^{12}$	-	-	-	14.4 ± 2.3	1	14.3 ± 2.4	1
	$2x10^{13}$	9.7 ± 2.4	13.1 ± *	11.6 ± *	10.9 ± 1.8	0.41	14.4 ± *	2.14
	$1x10^{14}$	-	-	-	8.8 ± 0.6	0.22	14.7 ± *	4.66
	$2x10^{14}$	6.6 ± 1.0	21.1 ± *	15.7 ± *	7.3 ± 0.4	0.18	13.1 ± *	6.35

* Gaussian approximation not appropriate to fit the distributions.

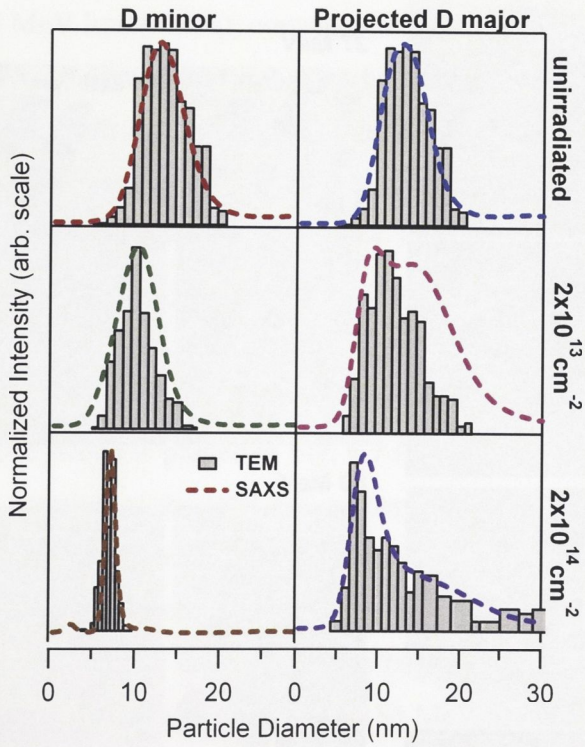

Fig. 6.4 - SAXS (lines) and TEM (bars) particle dimension distributions for samples containing NCs with mean diameter 14.5 nm (prior to SHII) irradiated with 185 MeV Au ions at different fluences. The evolution of D_{minor} is displayed on the left while the PD_{major} (at 45° sample tilt) is presented on the right. The TEM distributions for the PD_{major} were geometrically corrected using Eq. (4.1) to allow the comparison with SAXS results.

Figure 6.5 shows TEM micrographs of 14.5 nm Pt NCs irradiated with 27, 55, 89 and 185 MeV Au ions to a total fluence of $2x10^{14}$ cm^{-2} (left), as well as NCs

irradiated with different fluences of 27 and 89 MeV Au ions until saturation of D_{minor} was reached (right). For a fluence of $2x10^{14}$ cm^{-2}, 89 and 185 MeV irradiations yield a saturation of D_{minor} (as previously demonstrated in Fig. 6.2 for the latter). However, at lower energies this fluence is insufficient to achieve saturation. 27 MeV/$2x10^{14}cm^{-2}$ irradiation yields images similar to that observed for 185 MeV with a fluence five times lower, where the NCs change from spheres to prolate spheroids. The electronic energy loss is approximately four times greater at 185 MeV compared to 27 MeV. Furthermore, the threshold diameter for elongation decreases with a reduction in ion energy as apparent from Fig. 6.6, which shows the evolution of D_{major} and D_{minor} following irradiations at different energies. D_{minor} saturation values are approximately 4.3, 5.2, 5.4 and 6.7±0.1 nm (as obtained from a linear fit to the data) for 27, 55, 89 and 185 MeV.

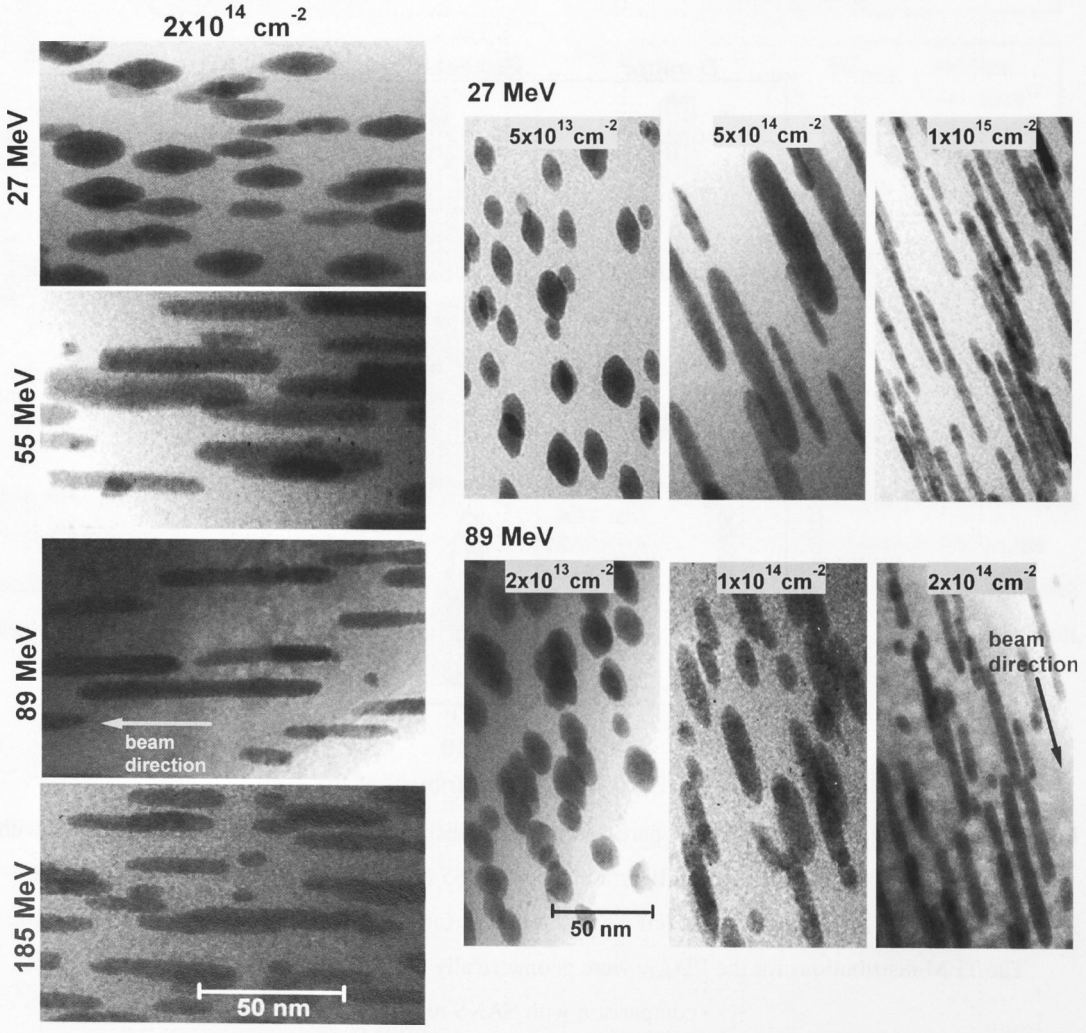

Fig. 6.5 – TEM micrographs of 14.5 nm Pt NCs (prior to SHII). (left) samples irradiated with $2x10^{14}$ cm^{-2} at different energies (as shown in each panel), (right) samples irradiated with 27 and 89 MeV at different fluences (as shown in each panel).

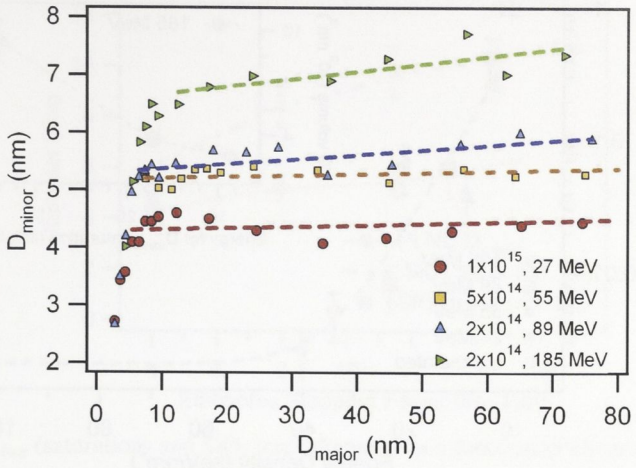

Fig. 6.6 - D_{minor} saturation for different energies and fluences (as determined by TEM).

The minimum irradiation fluence for which changes in shape were observed was ~10^{13} cm^{-2} (for 185 MeV irradiations), corresponding to ~15 ion impacts over the cross sectional area of a NC of diameter 14 nm. Clearly elongation is not a single ion impact event but it is the result of successive ion/NC/matrix interactions. The shape transformation was observed for all irradiation energies (27-185 MeV) or equivalently over the range of electronic stopping powers (4-17 keV/nm). In all cases the latter exceed the threshold (~2 keV/nm) for molten track formation in a-SiO_2.[28]

As demonstrated in Figs. 6.2 and 6.6, there is a threshold diameter for NC elongation at each irradiation energy. From a linear fit to the data above this threshold, we extracted the slope which is plotted in Fig. 6.7 (for NCs of mean diameter 14.5 nm prior to SHII) as a function of the total energy deposited by Au ions in SiO_2 (energy density). A slope of zero corresponds to the saturation of D_{minor}. Any ion energy dependence is within experimental error. The energy density required to reach saturation is necessarily NC size dependent, with larger NCs requiring more energy to saturate D_{minor} as shown in the Fig. 6.7 inset for 185 MeV irradiations. The NC volume plotted in the inset is that of the particles before irradiation as estimated from the elongated particle volume corrected to account for dissolution (details on NC dissolution are shown in the next section of this chapter).

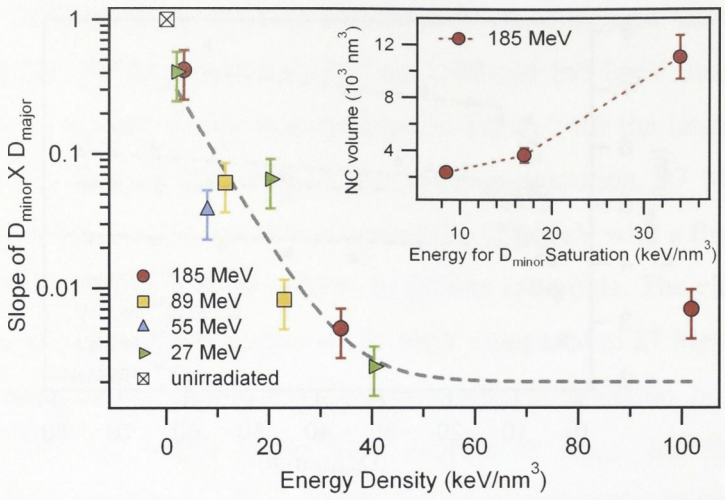

Fig. 6.7 – Slope extracted from linear fit to the data above the threshold diameter for elongation presented in Figs. 6.2 and 6.6 plotted as a function of energy density in SiO_2 for samples containing NCs as large as 19 nm diameter (prior to SHII). The inset shows the maximum NC volume for which D_{minor} saturation was observed as a function of energy deposited in the SiO_2 (for 185 MeV irradiations).

As reported by Toulemonde *et al.*,[14, 28] SHII of a-SiO_2 can result in the formation of a latent track with a diameter dependent on the ion energy. Tracks result from the rapid quenching of a cylinder of matter in which the energy transferred into the lattice exceeds that necessary for melting. Track diameters range from 6-10 nm for electronic stopping powers of 4-17 keV/nm.[29] Note the similarity between such values and those for the threshold diameters for elongation and D_{minor} saturations for Pt NCs following SHII. Figure 6.8 shows theoretical[29] and experimental[30] estimates of the track diameter in SiO_2 and the D_{minor} saturation for Pt NCs as a function of electronic energy loss. The track diameter in SiO_2 is larger than D_{minor} saturation for Pt NCs though both parameters scale with the electronic stopping power. We suggest the elongated metal NCs are confined by the molten track in amorphous SiO_2 and thus the shape transformation will not proceed in the absence of an embedding matrix as consistent with previous observations.[19]

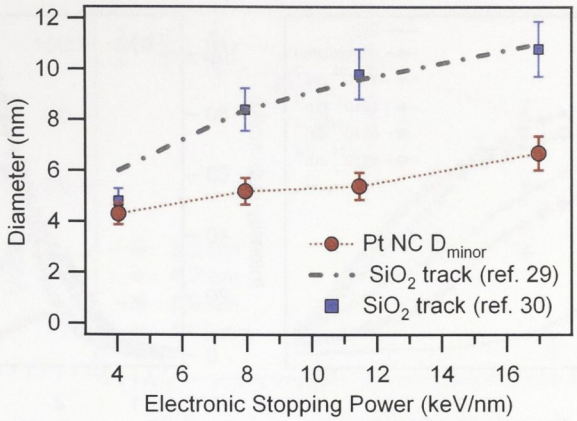

Fig. 6.8 – Pt NC D_{minor} (saturation) and SiO_2 track diameter as a function of electronic stopping power. The latter was extracted from ref.[29] and ref.[30]

6.4 – NC dissolution

Figure 6.9 shows TEM images of Pt NCs with a mean diameter (3.2 nm) less than the minimum required for elongation. The well defined NC/matrix interfaces apparent in unirradiated particles (Fig. 6.9(a)) are lacking following irradiation with 185 MeV Au ions to a total fluence of $3x10^{14}$ cm^{-2} (Fig. 6.9(b)). There is no evidence of a shape change for particles of this size. SHII causes dissolution of the particles, which decrease in size upon irradiation as demonstrated by the SAXS analysis presented in Fig. 6.10. For NCs of diameter of 3.2 nm irradiated with 185 MeV Au ions, a progressive reduction in NC diameter as a function of increasing irradiation fluence is apparent. The mean NC diameter and the standard deviation of the distributions are presented in Table 6.2 as a function of SHII fluence.

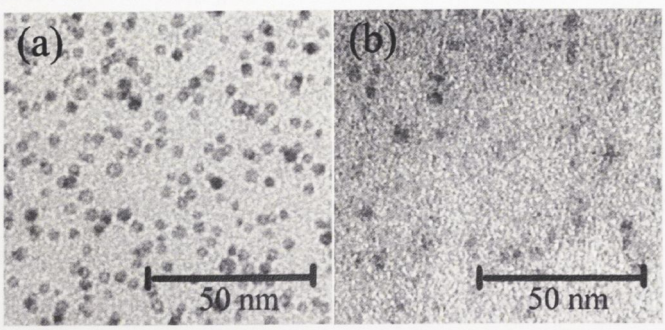

Fig. 6.9 - TEM micrographs of (a) unirradiated Pt NCs with 3.2 nm mean diameter and (b) the same NCs after SHII at 185 MeV Au ions to a total fluence of $3x10^{14}$ cm^{-2}.

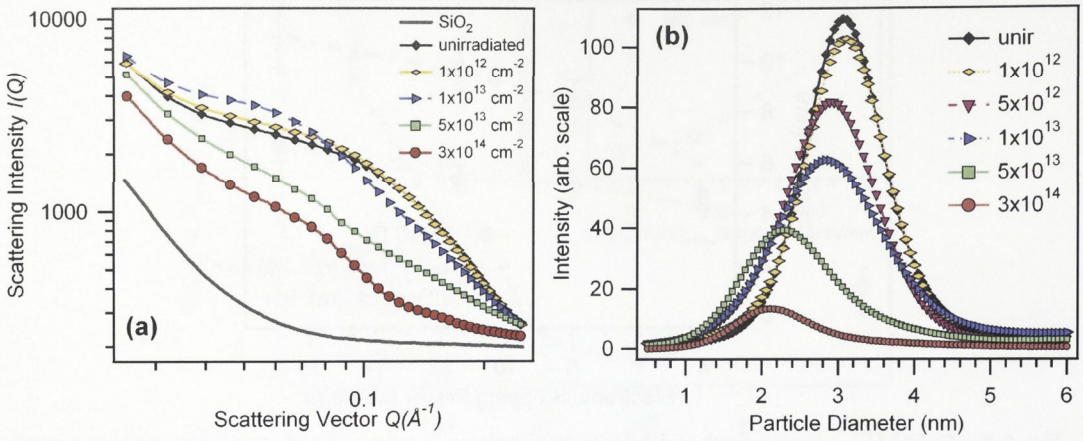

Fig. 6.10 - (a) Scattering intensity $I(Q)$ as a function of the scattering vector Q for Pt NCs with mean diameter 3.2 nm (prior to SHII) irradiated with 185 MeV Au ions at different fluences and the scattering contribution of a blank SiO_2; (b) particle diameter distributions for the same samples.

Table 6.2 – Mean particle diameter ($\mathbf{D_{mean}}$) and standard deviation of the distributions ($\boldsymbol{\sigma}$) for samples irradiated with 185 MeV Au ions.

Sample	SHII fluence (cm^{-2})	$\mathbf{D_{mean}}$ (nm)	$\boldsymbol{\sigma}$ (nm)
0.9 at. % 1100 °C	unirradiated	3.2	0.4
	$1x10^{12}$	3.1	0.4
	$5x10^{12}$	2.9	0.4
	$1x10^{13}$	3.0	0.5
	$5x10^{13}$	2.7	0.4
	$3x10^{14}$	2.6	0.3

From dimension distributions derived from SAXS, we extracted the total volume of scattering particles as a function of SHII fluence and particle size as shown in Fig. 6.11 (for 185 MeV irradiations). (For the SAXS experimental arrangement described herein, we are sensitive to NCs of diameter $\geq$ 1 nm). Clearly, for the same irradiation energy and fluence, smaller NCs are more readily dissolved in the matrix under irradiation, consistent with a larger surface-area-to-volume-ratio. These results are in agreement with those reported by Awazu *et al.*[31] for the lattice temperature of Au NCs under SHII - the smaller the NC, the higher the lattice temperature.

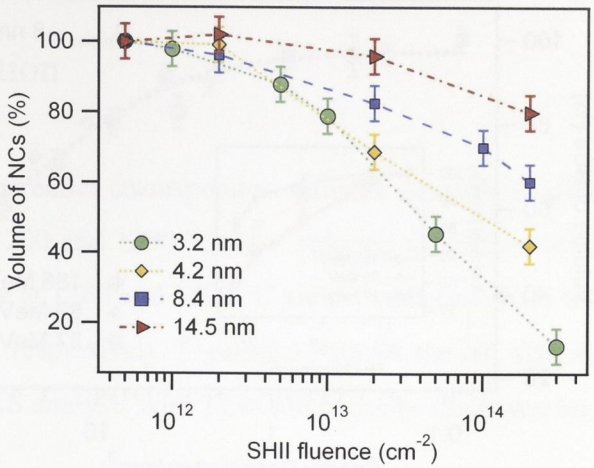

Fig. 6.11 - Volume percentage of remaining NCs as a function of SHII fluence. The values are relative to the unirradiated samples and the calculations are based on the total volume occupied by the particles according to SAXS analysis.

Fig. 6.12 shows the volume percentage of remaining NCs (with the same initial mean diameter (~8 nm)) irradiated with different energies and fluences. The main graph shows the total volume of NCs larger than ~1 nm as a function of energy density (i.e. the product of the electronic stopping power and the irradiation fluence) for samples irradiated with increasing fluences of 27, 89 and 185 MeV Au ions. The inset shows the same data as a function of SHII fluence, hence, data from different energies appear in separate curves. For a given energy (same particle size), dissolution is more pronounced the higher the irradiation fluence. However, the universal plot as a function of energy density demonstrates comparable dissolution can be achieved by different combinations of SHII energy and fluence. A similar effect was apparent in the elongation process (Fig. 6.5). When the energy density is comparable (for example, for samples irradiated with 89 MeV/2x10^{13} cm^{-2} and 27 MeV/5x10^{13} cm^{-2}, corresponding to an energy density of ~ 2 keV/nm^3), the NC shape and size are very similar. Note that dissolution due to SHII is a size dependent process, as shown in Fig. 6.11: the smaller the NC, the faster it dissolves, and it happens for all NC sizes regardless of elongation.[32] The results shown in Fig.6.12 correspond to samples with the same initial D_{mean}, hence the effects of SHII energy and fluence are highlighted with no influence of NC size.

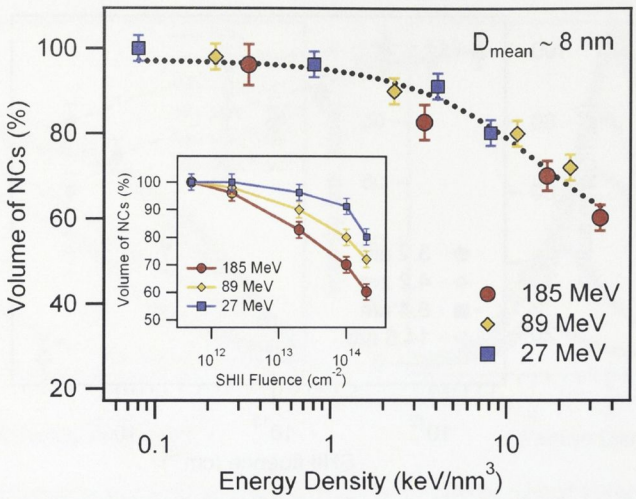

Fig. 6.12 – Volume percentage of remaining NCs as a function of energy density (energy deposited into the SiO_2). The inset shows the same data as a function of SHII fluence. The values are relative to the unirradiated samples and the calculations are based on the total volume occupied by the particles according to SAXS analysis.

TEM and SAXS results presented here clearly demonstrate that NC volume is not conserved upon irradiation, in contrast to previous reports.[4, 17, 19, 20] Figures 6.10 and 11 show, respectively, the mean diameter and the total volume of NCs contributing to the scattering process decrease as a function of increasing irradiation fluence. For example, using the mean dimensions derived from SAXS and listed in Table 6.1, the volume of a spherical NC of diameter 14.5 nm is twice that of the rod with D_{minor} and PD_{major} of 8.8 and 14.7 nm, respectively, observed after 185 MeV Au ion irradiation to a fluence of $1x10^{14}$ cm^{-2}. Furthermore, saturation of D_{minor} has yet to be achieved at such a fluence.

As apparent from Fig. 6.10(b), Pt NCs below the threshold diameter for elongation dissolve into the matrix upon irradiation. Similar observations were reported by D'Orleans *et al.*[4] for small Co NCs irradiated with 200 MeV I ions though the dissolution of small particles was accompanied by the growth of large particles, consistent with Ostwald ripening. The latter was not evident for Pt NCs. Figures 6.10(b) and Fig. 11 demonstrated, respectively, that the average particle diameter and the total volume of particles contributing to the scattering process both decreased with irradiation fluence. The dissolved Pt could be in the form of monomers in an oxidized environment within the matrix and/or metallic clusters too small (< 1 nm) for detection by either TEM or SAXS.

6.5 – H desorption

The results hereafter correspond to samples annealed in either O_2 or FG for 1 hr at temperatures of 1200 and 1300 °C (now referred to with nomenclature FG/1300, for example). Annealing at 1200 and 1300 °C yielded spherical NCs with mean diameter of ~8 nm and ~14 nm, respectively. Figure 6.13 shows the NC size distributions obtained from TEM and SAXS analysis with TEM micrographs displayed on the background.

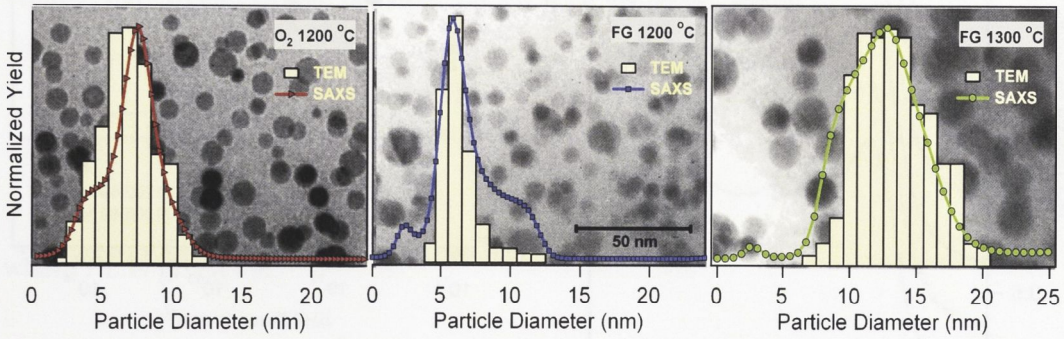

Fig. 6.13 – TEM (bars) and SAXS (line and symbols) diameter distributions measured for samples O_2/1200, FG/1200 and FG/1300. Representative TEM micrographs are shown on the background.

As demonstrated in the Chapter V, Pt NCs annealed in FG at temperatures above 1000 °C chemisorb H. The H content varies as a function of annealing temperature and/or NC size, as determined from XANES analysis.[24] Following the procedure described in Chapter IV, the H content was evaluated in FG/1200 and FG/1300 samples before and after irradiation with 89 and 185 MeV Au ions. The left panel in Fig. 6.14 shows the XANES spectra of FG/1200 samples before and after irradiation with 89 MeV Au ions, as well as the Pt foil. The area of the Lorentzian peak is plotted as a function of SHII fluence on the right panel. The decrease in NC size can affect the white line intensity and position, but this effect is only pronounced for NCs smaller than 3 nm in diameter (Fig. 5.11).[24, 33] Furthermore, no differences were found in the O_2 annealed samples, which are H-free and upon irradiation dissolve in a very similar manner to samples annealed in FG. The decrease in the area of the Lorentzian peaks for samples annealed in FG can thus be assigned to H desorption induced by SHII. Samples annealed at the highest temperature (1300 °C) had a greater H content, as previously

shown (Fig. 5.11). Upon irradiation, the H content progressively decreases as a function of fluence in samples annealed at both 1200 and 1300 °C. For a given annealing temperature (or equivalently a given NC size) and irradiation fluence, no significant differences are apparent when comparing irradiations at 89 and 185 MeV, as evident from the right panel in Fig. 6.14.

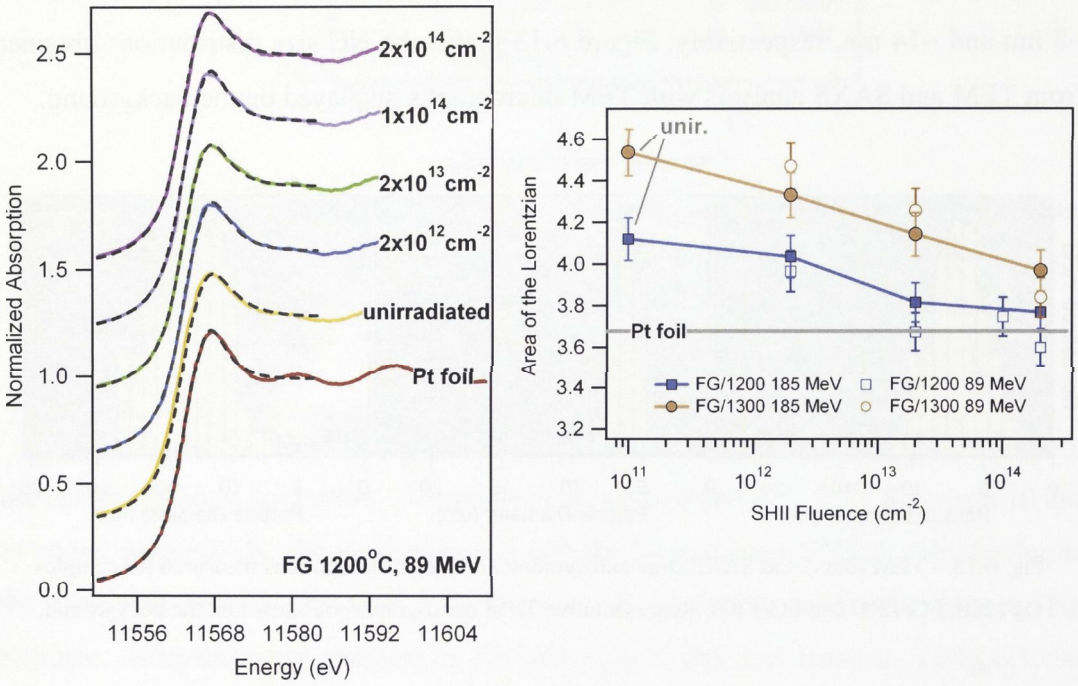

Fig. 6.14 – (left) Normalized Pt L_3 edge XANES spectra of FG/1200 samples irradiated with 89 MeV Au ions at the fluences shown in the graph. The dashed lines represent the fitting to the data. Spectra offset vertically for clarity. (right) Area of the Lorentzian fitted to the XANES data (white line peak) as a function of SHII fluence. Both graphs also show the results for a Pt foil and unirradiated samples.

SHII can induce latent track formation in a-SiO_2, resulting from the rapid quenching of a cylinder of matter in which the energy deposited into the matrix exceeds that necessary for melting.[14, 30, 34] The quench rate of the molten cylinder is governed by the thermal properties of the material.[35] In the framework of the thermal spike model, the energy deposited into the electronic system is rapidly transferred to the lattice via electron-phonon coupling and the energy is confined to a narrow region where the atoms thermalize and a molten track is formed (for a-SiO_2). In metals, the energetic electrons spread over a wider region before transferring energy to the lattice, and the thermal conductivity of both the electronic and lattice subsystems are much larger than

that of a-SiO_2.[31] Energetic ions do not form latent tracks in crystalline metals, although defect annihilation and other effects have been observed.[14]

Given the metallic character of the NCs, with higher thermal conductivity than the a-SiO_2 matrix, we assume that when an energetic ion passes through a NC the energy deposited along the NC length is rapidly and uniformly spread within the NC volume, but is restrained by the NC boundaries.[17] For example, 185 MeV (89 MeV) Au ions deposit energy in Pt at a rate of ~50 keV/nm (~30 keV/nm) compared to ~17 keV/nm (~12 keV/nm) in a-SiO_2. The electronic energy (E_d) deposited per atom in a NC varies according to the path length (PL) of the ion inside the NC as well as the NC volume (NC_{vol}) and atomic density (ρ), and can be estimated by:

$$E_d = \frac{S_e \cdot PL}{NC_{vol} \cdot \rho} \tag{6.1}$$

where PL is given by:

$$PL = 2\frac{D_{major}}{D_{minor}}\sqrt{\left(\frac{D_{minor}}{2}\right)^2 - B^2} \tag{6.2}$$

In addition to spheres (where $D_{major} = D_{minor}$), equation (6.2) enables the energy calculation to be extended to prolate ellipsoids with dimensions D_{major}, D_{minor} and ions impinging in a direction perpendicular to D_{minor} at a distance B from the NC axis. E_d varies as a function of inverse NC volume, but due to the alignment of D_{major} with the incident beam direction, the D_{major} terms from NC_{vol} and PL cancel out. Hence, the energy deposited per atom depends only on D_{minor}, or equivalently on the NC cross-sectional area (i.e., spherical and elongated NCs with the same cross-sectional area receive the same amount of energy per atom).

Figure 6.15 shows graphical representations of FG/1200 and FG/1300 samples before and after SHII. Ion trajectories for a fluence of $1x10^{12}$ cm^{-2} are shown, which were randomly generated using a Monte Carlo simulation[36] (for details see Appendix A). The NC size distributions are those determined by TEM and SAXS (Fig. 6.13). The number of particles was also preserved (from TEM), although concentrated in a cube 80 nm per side.

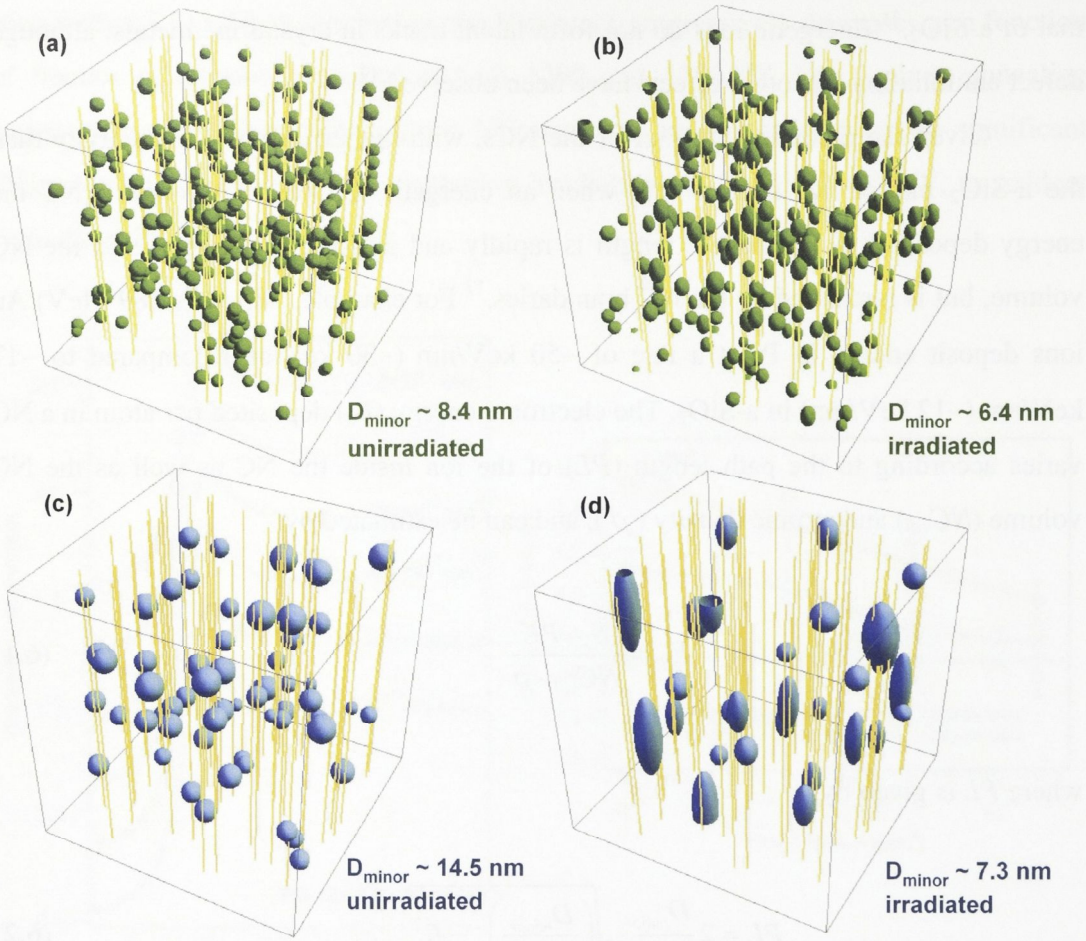

Fig. 6.15 – Graphical representation of (a),(b) FG/1200 and (c),(d) FG/1300 samples prior and subsequent to SHII, respectively. The lines represent the ion paths for an irradiation fluence of $1x10^{12}$ cm^{-2}.

The graphics shown in Fig. 6.15 were used to estimate the maximum energy deposited in each particle (subsequently converted to energy per atom using Eq.(6.1)) by 185 MeV Au ions (Appendix A). The above model, which considers randomly distributed particles and ion paths, shows that for low fluences (~10^{12} cm^{-2}) not all the particles were impacted by an ion, while others received multiple hits. Given the low irradiation flux used therein and the short time frames of energy transfer predicted by the thermal spike model[14, 31] the energy deposited in each event is dissipated before the next ion impact, hence, only the highest energy deposition events for each NC were considered in the results presented in Table 6.3 and Fig. 6.16. The fraction of atoms that received energy from an impinging ion relative to the total number of atoms, as well as the mean energy per atom for the impacted atom fraction and for the total number of atoms are listed in Table 6.3 for FG/1200 and FG/1300 samples irradiated with 185 MeV Au ions.

Table 6.3 – Fraction of impacted atoms ($\mathbf{F_{imp}}$) as well as the mean energy per atom (averaged from the maximum energy deposited in a single event) for the given F_{imp} fraction ($\mathbf{E_{imp}}$) and for the total number of atoms ($\mathbf{E_{total}}$) for samples FG/1200 and FG/1300 irradiated with 185 MeV Au ions.

	SHII fluence (cm^{-2}) 185 MeV	$\mathbf{F_{imp}}$	$\mathbf{E_{imp}}$ (eV/atom)	$\mathbf{E_{total}}$ (eV/atom)
FG/1200	$2x10^{12}$	25 ± 1 %	12.8 ± 0.1	3.2 ± 0.1
	$2x10^{13}$	89 ± 1 %	18.9 ± 0.1	16.8 ± 0.1
	$2x10^{14}$	100 %	27.5 ± 0.1	27.5 ± 0.1
FG/1300	$2x10^{12}$	61 ± 1 %	4.1 ± 0.1	2.5 ± 0.1
	$2x10^{13}$	99 ± 1 %	7.7 ± 0.1	7.6 ± 0.1
	$2x10^{14}$	100 %	16.4 ± 0.1	16.4 ± 0.1

Figure 6.16 shows the fraction of atoms and the corresponding maximum energy received for FG/1200 and FG/1300 samples after SHII with 185 MeV Au at different fluences. The sum of the column heights of each histogram corresponds to the fraction of impacted atoms $\mathbf{F_{imp}}$ given in Table 6.3.

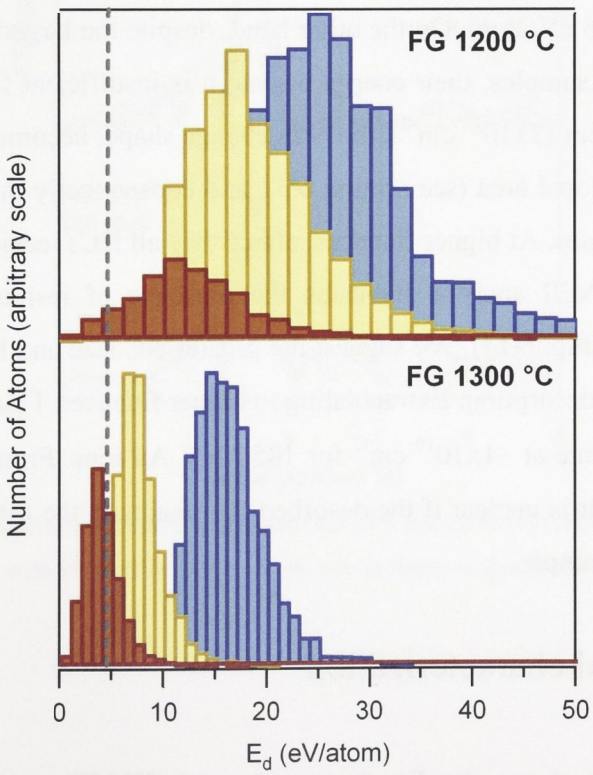

Fig. 6.16 – Number of impacted atoms as a function of energy per atom (from Eq. (6.1)).

As shown in Table 6.3, the fraction of impacted atoms necessarily increases with irradiation fluence for both FG/1200 and FG/1300 samples. For the former, $\mathbf{F_{imp}}$ is

lower at low fluences due to the smaller NC cross-sectional area. On the other hand, the smaller NC volume results in a higher energy per impacted atom. The increase in the mean energy per atom with increasing irradiation fluence for both samples is the combined result of the increase in the fraction of energetic atoms and the reduction in the NC cross-sectional area (reduction in D_{minor} as shown in section 6.3). Note that the NC size distributions used for the calculations were those from TEM for the given irradiation fluence, as shown in Table 6.1.

The influence of B on E_d (Eq.(6.1)) coupled with the given NC size distributions (Fig. 6.15), results in a broad energy distribution for the impacted atoms, as shown in Fig. 6.16. The energy required for H desorption is 2.6 eV for bulk Pt [37] and 2.4-4.6 eV for Pt clusters.[38, 39] These values correspond to H adsorbed on the surface and vary as a function of cluster size, adsorption site and H coverage. In our case the chemisorbed H is potentially distributed over the NC volume.[24] Assuming H desorption when the energy per atom (E_d) exceeds 4.6 eV (see dashed line in Fig. 6.16), the process is operative at lower fluences for FG/1200 samples since a considerable fraction of the atoms receive > 4.6 eV/atom. On the other hand, despite the larger fraction of impacted atoms in FG/1300 samples, their energy per atom is insufficient for H desorption. For intermediate fluences ($2x10^{13}$ cm^{-2}), the NCs change shape, becoming more prolate with reduced cross-sectional area (see section 6.3), and consequently the probability of E_d > 4.6 eV/atom increases. At higher fluences, effectively all NCs receive E_d > 4.6 eV/atom. Nevertheless, XANES analysis indicates the presence of residual Pt-H bonding in FG/1300 samples (Fig. 6.14). We suggest the greater NC size and H content may lessen the relative rate of desorption. Extrapolating to higher fluences, FG/1300 samples would achieve a H-free state at ~$1x10^{16}$ cm^{-2} for 185 MeV Au ions. From the analysis shown here, we note that it is unclear if the desorbed H remains in the matrix or is completely released from the sample.

6.6 – Structural characterization

Figure 6.17 shows the Fourier-transformed EXAFS spectra of O_2/1200 and FG/1300 samples irradiated with 89 MeV and 185 MeV Au ions. For the H-free samples annealed in O_2, the amplitude decreases as the irradiation fluence increases, consistent with a reduction in CN and increase in MSRD driven by the dissolution of

the particles. For samples annealed in FG, however, the amplitude first decreases ($\leq 2x10^{13}$ cm^{-2}), followed by a sudden increase ($2x10^{14}$ cm^{-2}). This unusual behavior, as we show below, is consistent with a combination of NC dissolution and H desorption, both driven by SHII. Refined fitting parameters for the first NN shell are listed in Table 6.4, which also shows the asymmetry (C_3) of the first NN shell of atoms surrounding a Pt absorbing atom.

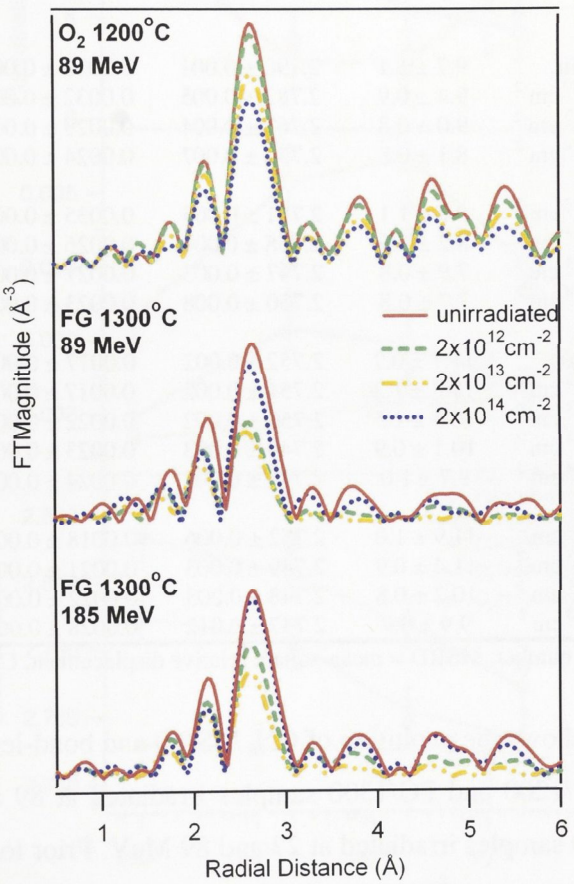

Fig. 6.17 – Fourier-transformed (non-phase corrected) EXAFS spectra of O_2/1200 and FG/1300 samples, irradiated with 89 MeV or 185 MeV Au ions at fluences shown in the graph.

Table 6.4 – Structural parameters obtained from first NN shell EXAFS analysis

Sample			CN (atoms)	Bond-length (Å)	MSRD ($Å^2$)	C_3 (10^{-5} $Å^3$)
Pt foil			12	2.752 ± 0.001	0.0017 ± 0.0001	-5 ± 1
FG 1300°C	185 MeV	unir.	9.5 ± 1.0	2.814 ± 0.008	0.0033 ± 0.0002	23 ± 11
		$2x10^{12}$ cm^{-2}	7.5 ± 0.7	2.802 ± 0.007	0.0040 ± 0.0002	24 ± 12
		$2x10^{13}$ cm^{-2}	6.9 ± 0.7	2.787 ± 0.005	0.0048 ± 0.0002	31 ± 15
		$2x10^{14}$ cm^{-2}	9.2 ± 0.9	2.768 ± 0.005	0.0037 ± 0.0003	5 ± 5
	89 MeV	$2x10^{12}$ cm^{-2}	7.1 ± 0.8	2.811 ± 0.006	0.0051 ± 0.0003	37 ± 18
		$2x10^{13}$ cm^{-2}	7.2 ± 0.8	2.789 ± 0.007	0.0055 ± 0.0004	32 ± 16
		$2x10^{14}$ cm^{-2}	8.8 ± 0.9	2.774 ± 0.005	0.0040 ± 0.0004	20 ± 9
FG 1200°C	185 MeV	unir.	9.7 ± 1.1	2.790 ± 0.004	0.0020 ± 0.0002	15 ± 6
		$2x10^{12}$ cm^{-2}	9.4 ± 0.9	2.782 ± 0.005	0.0032 ± 0.0003	11 ± 8
		$2x10^{13}$ cm^{-2}	9.0 ± 0.8	2.762 ± 0.004	0.0029 ± 0.0003	2 ± 3
		$2x10^{14}$ cm^{-2}	8.1 ± 0.8	2.753 ± 0.007	0.0024 ± 0.0002	-8 ± 9
	89 MeV	$2x10^{12}$ cm^{-2}	9.3 ± 1.1	2.781 ± 0.005	0.0035 ± 0.0003	15 ± 8
		$2x10^{13}$ cm^{-2}	8.2 ± 0.9	2.758 ± 0.004	0.0026 ± 0.0003	2 ± 3
		$1x10^{14}$ cm^{-2}	7.9 ± 0.8	2.747 ± 0.003	0.0027 ± 0.0002	0 ± 3
		$2x10^{14}$ cm^{-2}	7.7 ± 0.8	2.750 ± 0.008	0.0023 ± 0.0005	-1 ± 2
O_2 1200 °C	89 MeV	unir.	11.7 ± 0.9	2.752 ± 0.002	0.0017 ± 0.0002	0 ± 1
		$2x10^{12}$ cm^{-2}	11.3 ± 1.2	2.751 ± 0.002	0.0017 ± 0.0002	6 ± 1
		$2x10^{13}$ cm^{-2}	10.5 ± 1.5	2.750 ± 0.002	0.0022 ± 0.0002	12 ± 5
		$1x10^{14}$ cm^{-2}	10.1 ± 0.9	2.749 ± 0.003	0.0023 ± 0.0003	12 ± 7
		$2x10^{14}$ cm^{-2}	9.7 ± 1.0	2.747 ± 0.005	0.0024 ± 0.0002	11 ± 8
	27 MeV	$2x10^{12}$ cm^{-2}	11.9 ± 1.0	2.752 ± 0.006	0.0018 ± 0.0003	4 ± 1
		$2x10^{13}$ cm^{-2}	11.4 ± 0.9	2.749 ± 0.003	0.0021 ± 0.0002	6 ± 1
		$2x10^{14}$ cm^{-2}	10.2 ± 0.8	2.748 ± 0.003	0.0022 ± 0.0002	2 ± 2
		$1x10^{15}$ cm^{-2}	9.9 ± 0.9	2.747 ± 0.012	0.0028 ± 0.0012	9 ± 4

CN = coordination number, MSRD = mean-square relative displacement, C_3 = third cumulant.

Figure 6.18 shows the evolution of CN, MSRD and bond-length as a function of SHII fluence for FG/1200 and FG/1300 samples irradiated at 89 and 185 MeV. Also included are O_2/1200 samples irradiated at 27 and 89 MeV. Prior to irradiation, samples annealed in FG exhibit lower CN due to H chemisorption, as discussed previously. Upon irradiation, samples annealed in O_2 show a steady decrease in CN together with an increase in MSRD due to NC dissolution and fragmentation. FG/1200 samples also exhibit a decrease in CN with a maximum MSRD at intermediate fluences. FG/1300 samples (with the greatest amount of chemisorbed H) show a CN minimum at intermediate fluences with the MSRD exhibiting the opposite trend. The desorption of H alone should yield an increase in CN and decrease in MSRD. Dissolution, however, takes place simultaneously and is a competing effect, driving the CN and MSRD in the

opposite directions to those associated with H desorption. The two influences are separable from a comparison with samples that were annealed in O_2 that are H-free.

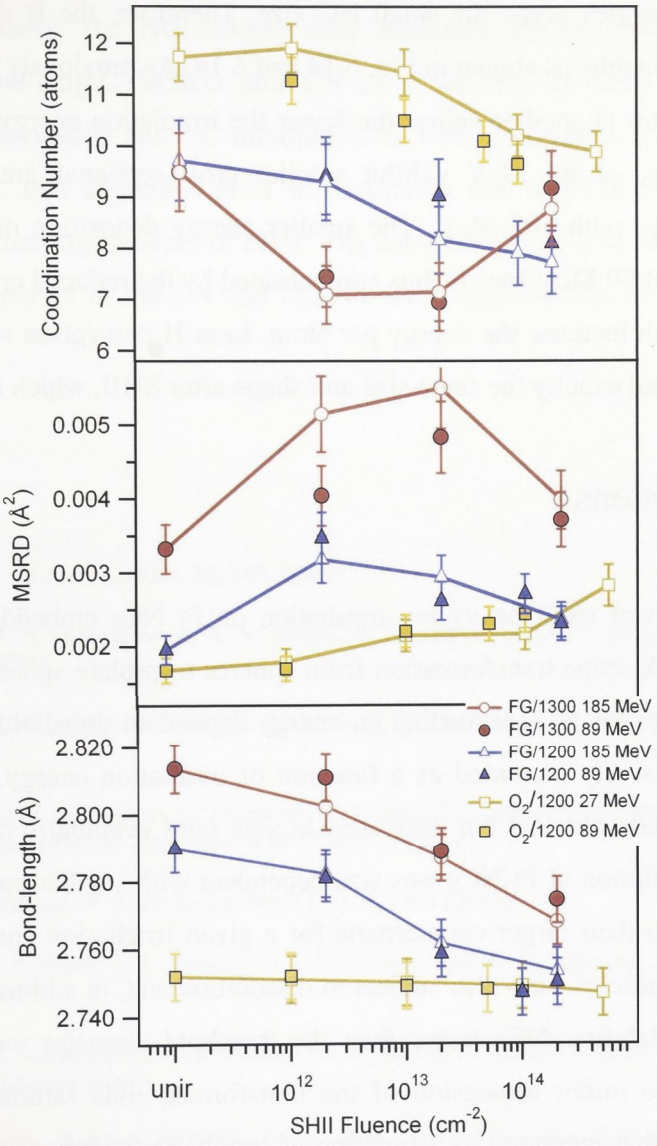

Fig. 6.18 – First NN shell coordination number (top), MSRD (middle) and bond-length (bottom) as a function of SHII fluence. Data obtained from EXAFS analysis of O_2/1200 irradiated at 27 and 89 MeV, FG/1200 and FG/1300 samples irradiated at 185 or 89 MeV.

NC dissolution and H desorption both cause a reduction in bond-length observed in the bottom panel of Fig. 6.18. The former yields smaller NCs, hence greater capillary pressure and thus smaller bond-lengths. The latter yields smaller bond-lengths simply due to the absence of H. The reduction in bond-length in samples annealed in FG is greater given both processes are operative.

In principle, 89 MeV irradiations should cause less H desorption and lesser changes in the structural parameters discussed above when compared to 185 MeV irradiations. However, for FG/1200 samples the probability that E_d > 4.6 eV/atom is high for both energies given the small NC size. Therefore, the H desorption at both energies is comparable, as shown in Fig. 6.14 and 6.18. As previously demonstrated, the NC D_{minor} saturates at smaller values the lower the irradiation energy, hence, FG/1300 samples irradiated at 89 MeV exhibit smaller cross-sectional area than the same particles irradiated with 185 MeV. The smaller energy deposition due to the reduced stopping power of 89 MeV ions is thus compensated by the reduced cross-sectional area of the NCs, which increase the energy per atom. Less H desorption would be apparent only if the NCs had exactly the same size and shape after SHII, which is not the case.

6.7 – Conclusions

The effect of swift heavy ion irradiation on Pt NCs embedded in a-SiO_2 had been examined. A shape transformation from spheres to prolate spheroids to elongated rods was observed for NCs exceeding an energy dependent threshold diameter, where the latter progressively increased as a function of irradiation energy. NCs below this threshold remained spherical but decreased in size until eventually dissolved into the matrix. The dissolution of Pt NCs was size dependent with smaller particles dissolving more rapidly than their larger counterparts for a given irradiation energy and fluence. Elongated nanoparticles were also subject to dissolution and, in addition, fragmentation via Rayleigh instability. NCs larger than the threshold diameter were progressively elongated and the minor dimension of the transformed rods saturated at an energy dependent value that increased as a function of irradiation energy. The total electronic energy deposition necessary to achieve saturation was determined as a function of NC size. As anticipated, larger NCs required greater total energy deposition to reach saturation. We have correlated the saturation of the minor dimension of elongated particles with the diameter of the molten track in amorphous SiO_2 and suggest the latter confines the irradiation-induced shape transformation.

The structural properties and H desorption of embedded Pt NCs irradiated with 27-185 MeV Au ions were also investigated as function of SHII fluence. XANES analyses suggested an irradiation-induced H desorption for NCs annealed in FG. NCs

with D_{mean} ~8 nm showed a significant reduction in H content after complete overlap was achieved. H desorption was also observed for NCs with D_{mean} ~14 nm, though the fluence required to achieve a H-free state would be considerably higher, approximately $1x10^{16}$ cm^{-2}. Clearly, the NC volume may influence the desorption process. The evolution of bond-length, MSRD and CN as a function of SHII fluence and the influence of H desorption and NC dissolution on such parameters was also examined. The bond-length, that expanded prior to irradiation due to Pt-H bonding, gradually decreased for increasing fluences of SHII. The competing effects of NC dissolution and H desorption, apparent in the CN and MSRD, were separated by comparison with H-free samples.

References

1 E. Roduner, Chem. Soc. Rev. **35**, 583 (2006).

2 H. Htoon, J. A. Hollingworth, A. V. Malko, R. Dickerson, and V. I. Klimov, Appl. Phys. Lett. **82**, 4776 (2003).

3 D. Katz, T. Wizansky, O. Millo, E. Rothenberg, T. Mokari, and U. Banin, Phys. Rev. Lett. **89** (2002).

4 C. D'Orleans, J. P. Stoquert, C. Estournes, C. Cerruti, J. J. Grob, J. L. Guille, F. Haas, D. Muller, and M. Richard-Plouet, Phys. Rev. B **67**, 220101 (2003).

5 R. Narayanan and M. A. El-Sayed, Nano Lett. **4**, 1343 (2004).

6 R. Giulian, P. Kluth, L. L. Araujo, D. J. Llewellyn, and M. C. Ridgway, Appl. Phys. Lett. **91**, 093115 (2007).

7 P. Kluth, B. Johannessen, G. J. Foran, D. J. Cookson, S. M. Kluth, and M. C. Ridgway, Phys. Rev. B **74**, 014202 (2006).

8 B. Johannessen, P. Kluth, R. Giulian, L. L. Araujo, D. J. Llewellyn, G. J. Foran, D. J. Cookson, and M. C. Ridgway, Nucl. Instrum. Meth. B **257**, 37 (2007).

9 R. Giulian, P. Kluth, B. Johannessen, L. L. Araujo, D. J. Llewellyn, D. J. Cookson, and M. C. Ridgway, Nucl. Instrum. Meth. B **257**, 33 (2007).

10 S. Klaumunzer and G. Schumacher, Phys. Rev. Lett. **51**, 1987 (1983).

11 A. Hedler, S. L. Klaumunzer, and W. Wesch, Nature Materials **3**, 804 (2004).

12 S. Klaumunzer, Nucl. Instr. and Meth. B **244**, 1 (2006).

13 E. Akcoltekin, T. Peters, R. Meyer, A. Duvenbeck, M. Klusmann, I. Monnet, H. Lebius, and M. Schleberger, Nature Nanotechnology **2**, 290 (2007).

14 M. Toulemonde, C. Dufour, and E. Paumier, Acta Phys. Pol. A **109**, 311 (2006).

[15] T. Van Dillen, E. van der Giessen, P. R. Onck, and A. Polman, Phys. Rev. B **74**, 132103 (2006).

[16] E. Snoeks, A. van Blaaderen, T. van Dillen, C. M. van Kats, K. Velikov, M. L. Brongersma, and A. Polman, Nuclear Instruments & Methods in Physics Research Section B-Beam Interactions with Materials and Atoms **178**, 62 (2001).

[17] B. Schmidt, A. Mucklich, L. Rontzsch, and K. H. Heinig, Nucl. Instrum. Meth. B **257**, 30 (2007).

[18] S. Klaumunzer, Nucl. Instr. and Meth. B **215**, 345 (2004).

[19] S. Roorda, T. van Dillen, A. Polman, C. Graf, A. van Blaaderen, and B. J. Kooi, Adv. Mater. **16**, 235 (2004).

[20] J. J. Penninkhof, T. van Dillen, S. Roorda, C. Graf, A. van Blaaderen, A. M. Vredenberg, and A. Polman, Nucl. Instrum. Meth. B **242**, 523 (2006).

[21] A. Oliver, J. A. Reyes-Esqueda, J. C. Cheang-Wong, C. E. Roman-Velazquez, A. Crespo-Sosa, L. Rodriguez-Fernandez, J. A. Seman, and C. Noguez, Phys. Rev. B **74**, 245425 (2006).

[22] P. Kluth, B. Johannessen, R. Giulian, C. S. Schnohr, G. J. Foran, D. J. Cookson, A. P. Byrne, and M. C. Ridgway, Radiat. Eff. Defects Solids **162**, 501 (2007).

[23] B. Joseph, J. Ghatak, H. P. Lenka, P. K. Kuiri, G. Sahu, N. C. Mishra, and D. P. Mahapatra, Nucl. Instrum. Meth. B **256**, 659 (2007).

[24] R. Giulian, L. L. Araujo, P. Kluth, D. J. Sprouster, C. S. Schnohr, B. Johannessen, G. J. Foran, and M. C. Ridgway, J. Appl. Phys. **105**, 044303 (2009).

[25] J. F. Ziegler, J. P. Biersack, and U. Littmark, *The Stopping and Range of Ions in Solids* (Pergamon Press, New York, 1985).

[26] L. Rayleigh, Proc. London Math. Soc. **10**, 4 (1878).

[27] M. E. Toimil-Molares, A. G. Balogh, T. W. Cornelius, R. Neumann, and C. Trautmann, Appl. Phys. Lett. **85**, 5337 (2004).

[28] M. Toulemonde, C. Trautmann, E. Balanzat, K. Hjort, and A. Weidinger, Nucl. Instr. and Meth. B **216**, 1 (2004).

[29] M. Toulemonde, C. Dufour, E. Paumier, and F. Pawlak, Mat. Res. Soc. Symp. Proc. **504**, 99 (1998).

[30] P. Kluth, et al., Phys. Rev. Lett. **101**, 175503 (2008).

[31] K. Awazu, X. M. Wang, M. Fujimaki, J. Tominaga, H. Aiba, Y. Ohki, and T. Komatsubara, Phys. Rev. B **78**, 054102 (2008).

[32] R. Giulian, P. Kluth, L. L. Araujo, D. J. Sprouster, A. P. Byrne, D. J. Cookson, and M. C. Ridgway, Phys. Rev. B **78**, 125413 (2008).

[33] A. I. Frenkel, C. W. Hills, and R. G. Nuzzo, J. Phys. Chem. B **105**, 12689 (2001).

[34] K. Awazu, S. Ishii, K. Shima, S. Roorda, and J. L. Brebner, Phys. Rev. B **62**, 3689 (2000).

[35] M. Toulemonde, C. Dufour, and E. Paumier, Phys. Rev. B **46**, 14362 (1992).

[36] http://www.wolfram.com.

[37] G. Papoian, J. K. Norskov, and R. Hoffmann, J. Am Chem. Soc. **122**, 4129 (2000).

[38] L. Chen, A. C. Cooper, G. P. Pez, and H. S. Cheng, J. Phys. Chem. C **111**, 5514 (2007).

[39] N. Watari and S. Ohnishi, J. Chem. Phys. **106**, 7531 (1997).

CHAPTER VII

CONCLUSIONS

This chapter contains the main conclusions and key findings from the research presented in this thesis, as well as experimental improvements achieved and possible future directions.

7.1 – Pt nanocrystal formation

We successfully formed Pt nanocrystals (NCs) in amorphous SiO_2 (a-SiO_2) using ion implantation and thermal annealing. Pt NCs preferentially nucleated around defects in the a-SiO_2 matrix, with the largest particles being formed at depths where vacancy production was a minimum. As a result, the NCs were smaller and exhibited narrower size distributions compared to other metallic NCs produced under similar conditions. A means of modifying the size distribution of Pt NCs was introduced by ion irradiation of the a-SiO_2 prior to Pt NC formation, first producing a near-uniform concentration of irradiation-induced vacancies over the extent of the SiO_2 layer.

The annealing temperature and ambient strongly influenced the Pt NC size. In contrast, the implantation fluence had a much smaller effect, with lower fluences actually yielding larger sizes as attributed to the defect-mediated nucleation process mentioned above.

A size-dependent bond-length contraction was observed for Pt NCs smaller than ~3 nm in diameter. For temperatures above 1000°C, however, annealing in forming gas yielded Pt-H bonding where the H content increased with increasing annealing temperature. The presence of H induced a bond-length expansion, increased atomic disorder and lower coordination number.

Relative to bulk values, the structural disorder and mean vibrational frequency increased as the NC diameter decreased. Embedded Pt NCs thus exhibit a size-dependent stiffening of bonds compared to bulk Pt. The vibrational properties of embedded Pt NCs are not significantly influenced by the a-SiO_2 matrix or H chemisorption. The constraint imposed by the matrix can, however, reduce the thermal expansion of embedded Pt NCs.

7.2 – Swift heavy ion irradiation of Pt nanocrystals

The shape transformation of embedded Pt NCs after swift heavy ion irradiation (SHII) was thoroughly characterized. NCs larger than an energy-dependent threshold diameter gradually changed from spheres to prolate spheroids to rods aligned in the incident ion beam direction. The minor dimension (D_{minor}) of the NCs decreased until

saturation at a value slightly smaller than the diameter of a molten track formed in a-SiO_2, suggesting NCs are confined by a temperature/energy barrier. Upon saturation of D_{minor}, D_{major} decreased by dissolution and fragmentation via Rayleigh instability. NCs smaller than the threshold diameter for elongation progressively dissolved in the matrix but remained spherical. For a given irradiation energy and fluence, dissolution was more pronounced for smaller NCs. For a given NC size, dissolution was energy density dependent, such that similar results were obtained for different combinations of irradiation energy and fluence.

SHII also induced H desorption from Pt NCs annealed in FG. The H content decreased considerably for ~8 nm NCs after fluences necessary for complete surface coverage. H desorption was slower in larger NCs, suggesting the process was influenced by the particle volume.

The shape transformation caused negligible changes in the structural parameters of the NCs irradiated with swift heavy ions. The H desorption and NC dissolution, on the other hand, caused significant changes in the bond-length, structural disorder and coordination number. The bond-length gradually decreased for increasing fluences of SHII, both due to NC dissolution and H desorption. These two processes had opposite effects on the evolution of coordination number and disorder with SHII fluence.

7.3 – Improvements to experiments and data analysis

A novel SAXS sample preparation method was developed to enable quantitative comparison between samples and avoid scattering contribution from the Si substrate. This technique was efficient and is useful not only for SAXS measurements, but also for optical and other experimental techniques where the samples must be a self-supported thin NC-containing a-SiO_2 film, especially for angle-dependent measurements.

A SAXS data analysis routine was also implemented to suit our needs of determining both NC dimensions. A method based on the analysis of selected areas of the scattered intensity was developed using the well established spherical model and the maximum entropy method. Both NC dimensions were recovered yielding excellent agreement with TEM results. By applying minimal corrections to the scattering intensity, we were also able to compare the volume of scattering centers in each sample.

7.4 – Improvements to the understanding of NC formation and characterization

The results shown in this thesis represent an important contribution to the field. To the best of the author's knowledge, the formation of Pt NCs in a-SiO_2 by ion implantation is reported here for the first time. The study of defect-mediated nucleation of Pt NCs adds to the existing knowledge of NC formation, identifying another means by which the NC size can be tailored. The NC structural characterization contributes to the understanding of finite size effects on parameters like coordination number, bond-length and atomic disorder, as well as thermal/vibrational properties.

This thesis presents the fist evidence of elongation of Pt NCs by swift heavy ions. The thorough characterization of irradiated Pt NCs contributes extensive experimental evidence to the existing knowledge of the shape transformation mechanism, which is still in its early stages. Information about D_{minor} saturation and its relation with the molten track in SiO_2, as well as the correlation between the changes in shape and the energy deposited in the matrix were reported here for the first time.

With the results presented in this thesis we demonstrate a means by which embedded Pt NCs chemisorb H, adding to the widely investigated H adsorption on supported Pt NCs. In spite of the latter being regarded as a surface effect, we demonstrate that for the NCs produced here the H is distributed over the NC volume and the H content decreases upon SHII.

7.5 – Future directions

Future work could include the quantification of the H content in samples annealed in FG for the development of a calibration curve for the XANES analysis. As part of this thesis, several analytical techniques (nuclear reaction analysis and secondary ions mass spectroscopy) were briefly investigated but without success.

The structural properties of free-standing Pt NCs, including the thermal/vibrational properties and the influence of H chemisorption/desorption without the interference of the a-SiO_2 matrix should be examined. A suitable chemical treatment to remove the matrix and possibly further improvements in sample preparation methods

would be required. Although no changes in shape are expected for free-standing NCs, given the necessity of a matrix for the elongation process to be operative, the SHII of such particles could yield insight in to the H desorption process.

The effects of SHII on metallic and semiconductor NCs including the shape transformation mechanism are far from understood. The experimental evidence shown in this thesis needs to be combined with theoretical models and results from other metallic and semiconductor NCs to yield a more comprehensive body of knowledge and enable the effective use of swift heavy ions in the fabrication of nanoscale materials with technological applications.

APPENDIX A

ENERGY DEPOSITED PER ATOM

This appendix contains the computational code used to calculate the energy deposited per atom presented in Chapter VI, section 6.5.

The following Mathematica* code was used to generate the 3D visual graphics shown in Fig. 6.16, from which the energy deposited per atom was calculated (Table 6.3 and Fig. 6.17). Random Gaussian NC size distributions were generated with mean value and standard deviation as determined by TEM. SHII fluences used here were the same as in the experimental results shown in Table 6.4, with the areal position of the ion impact randomized by Monte Carlo method. The particle density was determined from the mean NC size keeping a constant Pt concentration (determined from the implantation fluence).

3D NC model

```
Needs["Histograms`"]
samplesize=80; (*nm*)
Manipulate[Graphics3D[SeedRandom[sr];
 n2=IonFluence*samplesize^2;
 MeanR=4.2;
 sigma=0.5;
  n= 15.1*samplesize^2/(4/3 π*(MeanR)^3);
 ionposition=Table[RandomReal[{-samplesize,samplesize},{2}],{n2}];
 ionx=ionposition[[All,1]];
 iony=ionposition[[All,2]];
 A=Table[{ionx[[a]],iony[[a]],-100},{a,1,n2}];
 B=Table[{ionx[[a]],iony[[a]],100},{a,1,n2}];
 A1=Table[{A[[a]],B[[a]]},{a,1,n2}];Table[NCposition=RandomReal[{-
samplesize,samplesize},3];NCradius=RandomReal[NormalDistribution[MeanR,sigma]];{RGBColor[1,0.
8,0.1],Thick,Line[A1],Green,Sphere[NCposition,NCradius]},{n}],
 PlotRange→90,ImageSize→{300,300}],
Delimiter,{{IonFluence,0.01,"Ion Fluence (ions/nm^2)"},0.01,1,0.01},
{{sr,12342,"new random configuration"},1,100000,1}]
```

* http://www.wolfram.com

(Debug) Out[18]=

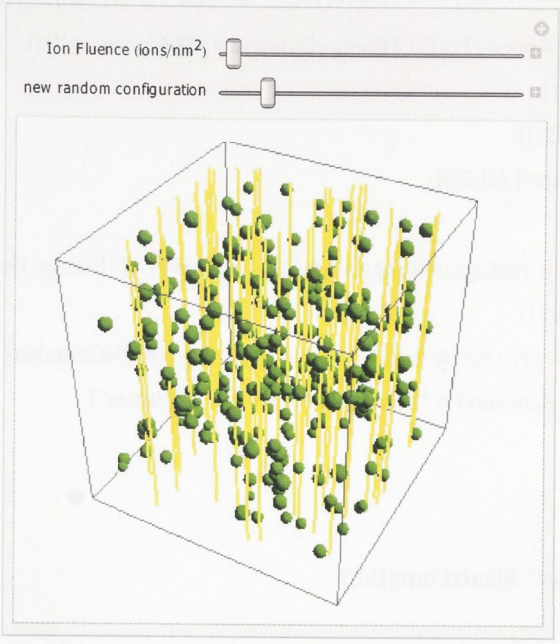

Energy deposited per atom

Input variables

samplesize=200; (* nm *)

IonFluence=0.02; (*10^12cm^-2→ 0.01 nm^-2, 10^13→ 0.1, 10^14→ 1*)

meanNCradius= 4.2; (* nm *)

sigma=1;

(*All the NCs in one nm^2 of sample ocupy a total volume of 15.1 nm^3*)

Ionnumber=IonFluence*samplesize^2;

NCnumber=(15.1*samplesize^2)/(4/3 π*meanNCradius^3);

NCradius=Table[RandomReal[NormalDistribution[meanNCradius,sigma]],{NCnumber}];

NCposition=Table[RandomReal[{-samplesize,samplesize},2],{NCnumber}];

Ionposition=Table[RandomReal[{-samplesize,samplesize},2],{Ionnumber}];

Needs["Histograms`"]

NCpx=NCposition[[All,1]];

NCpy=NCposition[[All,2]];

Ionpx=Ionposition[[All,1]];

Ionpy=Ionposition[[All,2]];

Ed={};

maximumEd={};

Do[B=$\sqrt{(\text{NCpx[[i]]} - \text{Ionpx[[j]]})^2 + (\text{NCpy[[i]]} - \text{Ionpy[[j]]})^2}$;

```
EnergyDeposited=(2*50*1000 √(NCradius[[i]]^2 - B^2) )/(4/3 π*NCradius[[i]]^3*66.23);
If[B≤NCradius[[i]],{AppendTo[Ed,{EnergyDeposited,(*NCposition[[i]],*)NCradius[[i]]}]}],{i,1,NCnum
ber},{j,1,Ionnumber}];
same=Tally[Ed[[All,2]]];
r=FoldList[Plus,1,same[[All,2]]];

Histogram[Ed[[All,1]],HistogramRange→ {0,15},AxesLabel→{"Energy Deposited
(eV/atom)",Frequency}]
Print["% of NCs that were hit by ions = ",(Length[same]*100)/NCnumber]
Print["Mean Energy deposited = ",Mean[Ed[[All,1]]], " eV/atom"]
Length[same]
MatrixForm[Ed]

Export["B12_2e12.dat",MatrixForm[Ed]]
```